KERNFORSCHUNGSANLAGE JÜLICH GmbH
Institut für Kernphysik

A Model for Nucleon Emission Induced by Electron Scattering

by

G. Co

Jül - 1931
June 1984
ISSN 0366-0885

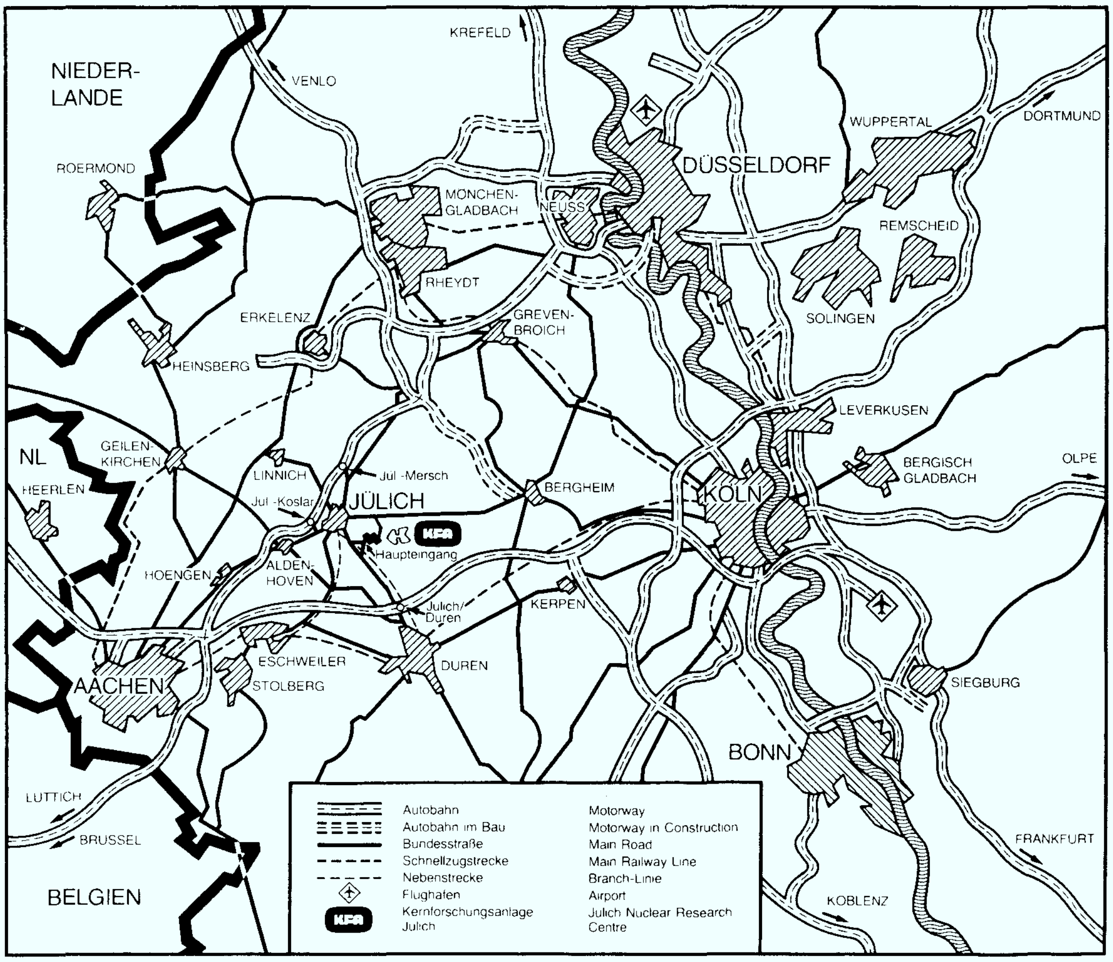

Als Manuskript gedruckt

Berichte der Kernforschungsanlage Jülich – Nr. 1931
Institut für Kernphysik Jül-1931

Zu beziehen durch: ZENTRALBIBLIOTHEK der Kernforschungsanlage Jülich GmbH
Postfach 1913 · D-5170 Jülich (Bundesrepublik Deutschland)
Telefon: 02461/610 · Telex: 833556-0 kf d

A Model for Nucleon Emission Induced by Electron Scattering

by

G. Co

D 5 (Diss. Uni. Bonn)

ABSTRACT

A model for the description of particle emission after electro-excitation of a nucleus is developed. The coupling between the individual decay channels is treated within the framework of the continuum random-phase approximation. The interference terms between charge and current operators as well as the interference term between the two different transverse components of the current operator are included in the calculation. The model is applied to the proton decay of ^{16}O and of ^{12}C. The sensitivity of the angular distribution of the emitted particle to the presence of weak multipole strengths is analysed. Coincidence experiments are shown to be a selective tool to excite bound states embedded in the continuum. Quasi-free knock-out is found to start immediately above the giant dipole resonance region. The analysis of the $^{12}C(e,e'p)^{11}B$ data of Stanford exhibits clear effects due to the presence of monopole strength, even though no concentrated monopole resonance is present in the theory.

TABLE OF CONTENTS

INTRODUCTION

Giant resonances are excitation modes of the nucleus in which a large number of nucleons participates. These collective excitations of the nucleus are characterized by the following properties:

i) They are a general feature of all nuclei, except the lightest ones, changing their form and width smoothly with the nucleon number A.

ii) Their width is small compared with their excitation energy which is typically of the order of a few tens of MeV.

iii) They exhaust a large fraction of the energy-weighted sum rule of the corresponding multipolarity.

This last property is particularly important since the sum rules relate the strength distribution of the excited states integrated over all the excitation energies to some simple, experimentally detectable, ground state properties such as the proton and neutron number, the rms radius, etc.

From the microscopic point of view giant resonances can be described as a superposition of mainly one-particle one-hole (1p-1h) configurations (see Ref. 1 for a review). Due to this relatively simple structure, the investigation of giant resonances is very attractive since it can provide information about the excitation mechanism of the nucleus and in particular about the structure of the nucleon-nucleon interaction in the medium.

In this context one has to point out that the only reliable values of the compression modulus K of the finite nucleus, which is a fundamental property of the effective nucleon-nucleon interaction[2)], are extracted from the giant monopole resonances[3]. In addition to that one has to remark the big interest provoked by the recently discovered spin-isospin collective modes in (p,n) and (^{3}He,t) charge-exchange experiments[4]. These states are extremely sensitive to the details of the spin-isospin interaction and offer the possibility to investigate in detail the effects of one-boson exchange potential inside the nucleus.

Most of our knowledge about giant resonances is coming from one-arm experiments, such as (p,p'), (α',α') and (e,e') (see Ref. 5). Obviously, these are the simplest experiments to perform, on the other hand, in this kind of experiments, the presence of the physical background creates ambiguities which make it very hard to identify weak multipole modes. As a consequence, even in the case of strong resonances, the comparison with the energy-weighted sum rule strengths remains problematic. One may hope that using coincidence experiments, in which the scattered particle is detected in coincidence with particles emitted from the nucleus, these problems will be reduced.

In the giant resonance region, the first coincidence experiments[6,7,8] have been performed to eliminate seeming discrepancies between strength distributions obtained from inelastic scattering and capture experiments respectively. This goal was largely achieved and, as additional results of these investigations, one obtained a convincing evidence for the existence of a compact giant quadrupole resonance in ^{16}O [8] and of a weak quadrupole resonance in ^{12}C [9].

Certainly the investigation of nuclear excitation modes which are not clearly identifiable in one-arm experiments, such as the isovector monopole and quadrupole resonances, constitutes only one part of the motivations to perform coincidence experiments. More recently the interest has shifted to the study of the decay of the collective state itself, i.e. to understand how the nucleus dissipates the energy stored in this collective mode of excitation[10]. For example, one would like to know up to which extent the nucleus decays via proton or neutron emission and under which circumstances more complicated configurations possibly admixed to the giant resonances, such as $(\alpha \otimes {}^{12}C)_{2^+}$ in the case of giant quadrupole resonances in ^{16}O [11], contribute to the decay products.

In this work we develop a model to describe the decay of the giant resonances via nucleon emission.

Up to now, coincidence experiments in the giant resonance region have been performed mostly with hadrons which have the advantage, with respect to electro-magnetic probes, of a higher count rate. In effect, one of the main difficulties in performing double coincidence experiments is due to the low count rate which can be estimated, assuming an isotropic emission of the decay product, to be reduced by a factor of 100 to 1000 with respect to the count rate of the corresponding inclusive experiment.

On the other hand, strongly interacting particles have a high multiple collision probability, and consequently the analysis of the experimental data has to deal with multi-step processes. In this context, however, one has to remark that in the intermediate energy region from 160 MeV to 400 MeV the nucleon-nucleon interaction becomes relatively weak[12] and the reaction mechanism reduces mainly to one-step processes.

The advantages offered by electro-scattering as compared with hadron scattering are well established: the interaction is precisely known and is weak enough, at least in comparison with low energy hadrons, to probe the nucleus without greatly disturbing its structure.

These remarks are also valid for photon scattering, but with electron scattering one has the possibility to change the momentum transfer for a fixed value of the excitation energy.

The new generation of electron accelerators, such as the MAinzer MIkroton[13] operating since July 1983, and the new machines planned or being already under construction in Darmstadt, Frascati, Lund, Saclay, Amsterdam, Stanford, BATES, Charlottesville, Sendai[14], allows to overcome the problems implicit in the low count rates and in the small values of the electron scattering coincidence cross sections (of the order of 10^{-32} cm^2 in the giant resonance region). The transition from the pulsed electron beam to high duty factor (reaching values around 100 %) allows, using average beam intensity of few hundred of μA, 63 μA at MAMI, to work with reasonable count rates. Nowadays, with the improvement of the beam quality and of the detection equipment one can measure cross sections down to 10^{-38} cm^2 [15].

From the theoretical point of view the description of the electron-scattering coincidence experiments results to be easier to handle than the description of hadron induced decay since with strongly interacting projectiles one has to deal with important effects due to the absorption of the probe. Therefore we chose to apply our model to the description of (e,e'N) coincidence experiments. One should remark, however, that our approach is general enough to be extended straightforwardly to describe hadron coincidence experiments.

There are two extreme pictures describing particle emission induced by inelastic scattering processes:

(i) quasi-free knock-out, where the projectile interacts only with the emitted particle, leaving the residual nucleus practically undisturbed,

(ii) resonant decay, where the nucleus is excited as a whole, vibrates and finally decays by emitting a particle.

The validity of each of these two pictures is connected with the nuclear excitation energy and the momentum transfer region under investigation.

So far coincidence experiments with electrons were performed mainly in order to investigate the hole structure of the nucleus[16,17,18]. In order to minimize the effects of the collective degrees of freedom, these experiments have been performed for high values of the nuclear excitation energy (~ 150 MeV) and of the momentum transfer (~ 2 fm^{-1}). From the theoretical point of view models based on the quasi-free knock-out picture[19,20,21,22,23] provide a successful analysis of these experiments.

A proper description of the decay of the giant multipole resonances can be done only within the framework of the resonant decay picture, since giant multipole resonances are collective nuclear excitation modes. In all nuclei the giant multipole resonances are located above the particle emission threshold, therefore one of the essential decay mechanisms of these collective excitations is particle emission.

As an alternative to particle emission, the resonance can proceed towards the creation of a complicated compound system through a sequence of 2p-2h, 3p-3h, ..., np-nh states. The compound nucleus does not conserve memory about the excitation mechanism and decays emitting particles in a statistical way.

In heavy nuclei (A > 40) this process predominates the direct emission from an early stage of the precompound hierarchy[10]. This is due to the fact that charged particle emission is disfavoured by the increased Coulomb barrier and, in addition, the energy gap between the occupied and unoccupied single-particle states scales with $A^{1/3}$, favouring the coupling to n-p n-h configurations.

Since the statistically emitted hadrons contaminate the information about the decay properties of the giant resonances, it is reasonable to start investigations of hadron emission in light nuclei, where direct emission is more relevant.

One should remark, however, that the study of giant resonances in heavy nuclei with coincidence techniques is not completely hopeless since the direct decay can be relevant enough to be investigated. For example, in a recent $(\alpha,\alpha'n)$ experiment on a ^{208}Pb target[24)], a direct decay component of ~ 15 % was estimated for the resonant strength in the monopole/quadrupole region. Furthermore, in the case of high-lying modes, such as the isovector multipole modes, the decay width certainly is an essential contribution of the full width.

The observation of an emitted hadron in coincidence with the scattered particle breaks the rotational symmetry of the nuclear final state with respect to rotations around the direction of the momentum transfer. This fact involves two important differences in comparison with the one-arm experiments where only the scattered particle is detected:

i) all the multipole modes present at a specific excitation energy will interfere,

ii) if the nuclear excitation is induced by a vector operator, even the individual components of the vector operator will interfere.

The well-known reaction mechanism of electron scattering allows to take full advantage of the interference between the different vector components of the transition operator. Only three components of the current are linearly independent because of current conservation. Usually these are chosen to be the charge and the two transverse components of the current. The contribution of each of these components can be isolated in coincidence experiments by changing the detection angles. This fact leads to the possibility of a careful investigation of the structure of the current operator; in this context one should note that the spin currents are particularly sensitive to admixtures of subnuclear degrees of freedom, such as meson exchange currents or the $\Delta_{33}(1232)$ isobaric resonance.

The interference between modes with different multipolarity may be used to identify weak multipole strengths. In coincidence experiments the contribution to the cross section of these weak excitation modes is enhanced by the interference with stronger multipoles and may lead to measurable effects in the angular distribution of the decay products.

The requirements for our model aiming to describe the electron-scattering coincidence processes in the giant resonance region can be summarized as follows. First, since giant resonances are collective modes, the model should include the coupling between the different decay channels. Second, the model should describe properly the nuclear excitation in the continuum. At a given excitation energy, the angular distribution of the emitted particle is very sensitive to the strength of a multipole mode. Since modes of different multipolarities overlap in the continuum, a correct description of the width of the giant resonances is called for. A third requirement is the inclusion of all the interference terms between the different components of the electro-magnetic transition operators. Even though for forward scattering angles of the electron the dominant contribution to the cross section is due to the charge term, one needs the current transition densities in order to understand the asymmetries in the angular distribution of the emitted hadron. Clearly, without current operators, one would forgo the possibility of investigating the effects of magnetic modes.

The nuclear excitation model used in the present work considers the superposition of all those 1p-1h configurations which can contribute at a given momentum transfer and includes the channel-to-channel coupling by solving the continuum random-phase-approximation for each multipole mode.

This model takes into account only one part of the width of a multipole resonance, the so-called escape width $\Gamma^{\uparrow}$ generated by the width of the continuum single particle waves. The so-called spreading width $\Gamma^{\downarrow}$, originated by the splitting of the single particle states due to the coupling to collective nuclear vibrations, is not considered in our model.

This model is expected to work reasonably well in light nuclei, where the escape width is larger than the spreading width. For more detailed questions, of course, the inclusion of at least all 2p-2h degrees of freedom is indispensable. One should remark, however, that at present a combined treatment of both 2p-2h effects and single particle continuum is not even available for a single resonance with definite multipolarity.

Since this is the first work where the four terms of the coincidence cross section are evaluated starting from a microscopic description of the nuclear excitation, a first question we studied qualitatively concerns the relative magnitude of the different terms, especially the charge/current interference term as compared to the current/current interference term.

Second, we explored the sensitivity of the angular distribution of the emitted particle to the presence of weak multipole strength.

As a third point we investigated the selectivity of the tool in exciting the different nuclear modes for a fixed value of the nuclear excitation energy. This has been done both by changing the value of the momentum transfer and selecting the energy of the emitted particle.

A further important problem we studied is how rapidly the effects of the channel-to-channel coupling vanish with increasing excitation energy.

In the last part of this work we applied our model to analyse the experimental data of Calarco et al.[25] for the reaction $^{12}C(e,e'p_0)^{11}B$. Up to now these are the only data available of an electron-scattering coincidence experiment performed to analyse the decay of giant resonances. The results are promising and new experiments performed on ^{208}Pb [26] and ^{28}Si [27] targets have to be analysed; other experiments are already planned in Mainz[28].

CHAPTER 1

The Coincidence Cross Section

In this chapter we derive the coincidence cross section formula expressing the nuclear final state in terms of multipole excitations of the nucleus. First we define the notations employed in this work. We work in natural units ($\hbar$=c=1) and we adopt the conventions of Ref. 29.

The initial and final electron four-momenta are $k_i \equiv (\varepsilon_i,\vec{k}_i)$ and $k_f \equiv (\varepsilon_f,\vec{k}_f)$, respectively, and we assume the ultra-relativistic approximation m_e=0.

The four-momentum transfer is defined as

$$q \equiv (\omega,\vec{q}) \equiv (\varepsilon_f-\varepsilon_i,\vec{k}_f-\vec{k}_i) \qquad (1)$$

The scattering angle of the electron is denoted by ϑ_e (see Fig. 2). We work in the laboratory frame. The z-axis is chosen along the direction of the momentum transfer and the y-axis coincides with $\vec{k} = \vec{k}_f \times \vec{k}_i$. With this choice, the scattering plane, defined by $\vec{k}_f$ and $\vec{k}_i$, is the x,z plane.

The direction of the emitted particle momentum $\vec{p}$ is determined by two angles: the angle ϑ_p between the z-axis and $\vec{p}$, which runs from 0 to π, and the angle φ_p between $\vec{p}$ and its projection on the xz plane, which varies between 0 and 2π.

The interaction between the electron and the electromagnetic field of the nucleus is described by the exchange of one virtual photon. Following Refs. 30 and 31, we consider the electron wave functions to be plane waves. Then the cross section is given by:

$$d\sigma = \frac{2e^4}{(2\pi)^3} \frac{1}{\varepsilon_i \varepsilon_f} \frac{1}{q_\mu^4} [2J_\mu Q^\mu J_\nu^+ Q^\nu + \frac{1}{2} J_\mu^+ J^\mu q_\nu q^\nu] d\vec{k}_f d\vec{p} \qquad (2)$$

where an average over the initial states and a sum over the final ones is understood. In eq. (2) we used the notation:

$$Q = \tfrac{1}{2}(k_f + k_i) \qquad (3)$$

In the expression of the coincidence cross section, given by eq. (2), all the information about the nucleus is contained in the nuclear currents $J_\mu(\vec{q})$ which are defined as:

$$J_\mu(\vec{q}) = \int d\vec{r}\, e^{-i\vec{q}\cdot\vec{r}} \langle \Psi_f | \hat{J}_\mu(\vec{r}) | \Psi_i \rangle \qquad (4)$$

Here $|\psi_i\rangle$ and $|\Psi_k\rangle$ are the initial and final states of the nuclear system and $\hat{J}_\mu(\vec{r})$ is the one-body electro-magnetic operator. The scalar component of this operator corresponds to the nuclear charge density $\hat{\rho}(\vec{r})$, while the vector component is the nuclear current density $\hat{J}(\vec{r})$. Meson-exchange currents are neglected throughout this work.

Current conservation

$$q_\mu J^\mu = 0 \qquad (5)$$

implies that, in spherical coordinates, for the particular choice of the quantization axis ($Z//\vec{q}$), the electromagnetic field of the nucleus can be described by three components: two transverse ones, $J_\pm$ generated by the current operator, and one longitudinal, J_0 generated by the charge operator[30]. For nuclei with ground state angular momentum zero, the cross section, eq. (2), simplifies to:

$$d\sigma = \frac{2e^4}{(2\pi)^3}\frac{1}{\varepsilon_i\varepsilon_f}\frac{1}{q_\mu^4}\,[V_c J_o J_o^+ + V_t(J_- J_-^+ + J_+ J_+^+)$$
$$+ V_I(J_- J_o^+ + J_o J_-^+ - J_+ J_o^+ - J_o J_+^+) + V_S(J_+ J_-^+ + J_- J_+^+)]d\vec{k}_f d\vec{p} \qquad (6)$$

The V coefficients of eq. (6) do not contain any information about the nucleus. They are defined as

$$V_c = \frac{1}{2}\frac{q_\mu^4}{|\vec{q}|^4}\,[(\varepsilon_f+\varepsilon_i)^2 - |\vec{q}|^2]$$
$$V_t = \vec{Q}^2 - \left(\frac{\vec{Q}\cdot\vec{q}}{\vec{q}}\right)^2 - \frac{1}{2}q_\mu^2$$
$$V_I = \frac{1}{\sqrt{2}}\frac{q_\mu^2}{|\vec{q}|^2}\frac{|\vec{k}_f\times\vec{k}_i|}{|\vec{q}\,|}(\varepsilon_f+\varepsilon_i) \qquad (7)$$
$$V_S = -\frac{|\vec{k}_f\times\vec{k}_i|^2}{|\vec{q}\,|^2}$$

Eq. (6) has been obtained simply from kinematical considerations without making any assumption about the excitation mechanism of the nucleus. For this reason it has the same form as the coincidence cross section formula for radiative decay processes, (e,e'γ)[32], and as the cross section of the deuterium electro-disintegration[33,34,35]. The kinematic governing of all these processes is the same.

At this stage, a model for the nuclear excited states enters. We restrict our work to doubly-magic nuclei. Here, the average nuclear potential has spherical shape and generates a set of bound single-particle states characterized by the total angular momentum j_p and the energy ε_p. Since the excitation energy of the nucleus is known by measuring the scattered electron, $E=\varepsilon_i-\varepsilon_f=-\omega$, and the energy ε_p of the emitted particle is available in a coincidence experiment, the energy of the residual nucleus is known.

Within our model, the angular momentum I and the parity π_I of the rest nucleus correspond to the angular momentum and the parity of the shell model hole state in the target nucleus, and the energy of the residual nucleus is identified with the energy of the hole state $\varepsilon_h=\varepsilon_p-E$. Asymptotically, the nuclear final state, at the excitation energy E is composed of the wave function of the emitted nucleon $\Psi(\vec{p}\cdot\vec{r})\chi_\sigma^{1/2}$, described by the momentum $\vec{p}$, the spin $1/2$ and its projection σ on the z-axis, and of the wave function $\Phi(r_i-r_{A-1};\varepsilon_h;Im_I)$ of the rest nucleus with spin I and projection on the quantization axis m_I:

$$\left| E;\vec{p}\,1/2\,\sigma;Im_I\right\rangle \underset{r\to\infty}{\to} \Psi(\vec{p}\cdot\vec{r})\chi_\sigma^{1/2}\,\Phi(\vec{r}_1-\vec{r}_{A-1};\varepsilon_h;Im_I)\Big|_E \tag{8}$$

The parity π_I of the residual nucleus has not been written down explicitly for convenience. The total energy of the system has been denoted by E. Asymptotically it is the sum of the energies of the emitted particle and of the residual nucleus.

In the absence of the nuclear field, the wave function Ψ of the emitted nucleon would reduce to a plane wave. In the present context, however, the interaction of the emitted particle with the residual nucleus introduces phase shifts which are obtained by solving the Schrödinger equation for a nuclear central potential.

Expanding the asymptotic wave function in multipoles one obtains

$$\left|E;\vec{p}\,{}^1\!/\!{}_2\,\sigma;Im_I\right\rangle \underset{r\to\infty}{\to} 4\pi \sum_{\ell,\mu}^{\infty} i^{\ell} u_{\ell}(pr) Y^{*}_{\ell,\mu}(\hat{p}) Y_{\ell,\mu}(\hat{r}) \chi^{1/2}_{\sigma} \Phi(\vec{r}_1,\ldots,\vec{r}_{A-1};\varepsilon_h;Im_I)\Big|_E \tag{9}$$

where $u_\ell(pr)$ is the solution of the radial Schrödinger equation, $\hat{p}$ and $\hat{r}$ indicate the angles defining the directions of the vectors $\vec{p}$ and $\vec{r}$ and $Y_{\ell,\mu}$ is the spherical harmonic. Coupling first the orbital angular momentum ℓ and the spin of the nucleon to the total angular momentum j, and second, coupling this angular momentum j with the angular momentum I of the residual nucleus to a total angular momentum J of the target nucleus, one obtains:

$$\begin{aligned}\left|E;\vec{p}\,{}^1\!/\!{}_2\,\sigma;Im_I\right\rangle = \frac{4\pi}{p} \sum_{\ell\mu} \sum_{jm} \sum_{JM\pi}^{\infty} i^{\ell} Y^{*}_{\ell,\mu}(p) \langle \ell\mu\, {}^1\!/\!{}_2\, \sigma | jm\rangle \langle jmIm_I | JM\rangle \\ \cdot \left|E,J,M,\pi;(Ij\ell;p)\right\rangle\end{aligned} \tag{10}$$

where we defined

$$\left|E,J,M,\pi;(Ij\ell;p)\right\rangle \underset{r\to\infty}{\to} pr\, u_\ell(pr) \sum_{m'} \langle jm'Im_I|JM\rangle \vec{Y}^{m'}_{j\ell}(\hat{r}) \Phi(\vec{r}_1,\ldots,\vec{r}_{A-1};\varepsilon_h;Im_I)\Big|_E \tag{11}$$

with $\vec{Y}^{m}_{j\ell}(\hat{r})$ indicating the spin spherical harmonics[36]. The wave function $\left|E,J,M,\pi;(Ij\ell;p)\right\rangle$ describes a system of A nucleons with angular momentum J, with projection M on the quantization axis, parity π and energy E having one particle in a continuum wave of orbital angular momentum ℓ and total angular momentum j. The total angular momentum of the corresponding residual nucleus is denoted by I. Note that the parity π is determined by the parity π_I of the residual nucleus and by the orbital angular momentum ℓ of the continuum wave.

At this stage it has to be pointed out that the multipole expansion of the nuclear final state with one emitted and one detected particle given by eq. (10) is completely general. Any nuclear model which describes the emission and detection of a nucleon has to be formulated in such a way that its final state coincides asymptotically with the multipole expansion (10). A model independent expression for the transition densities can be obtained by using the multipole expansion of the asymptotic state eq. (10) in order to evaluate the expectation of the nuclear current operator eq. (4). With our choice of the quantization axis ($z//\vec{q}$), the nuclear current, eq. (4), becomes:

$$J_\eta(\vec{q}) = \frac{(32\pi^3)^{1/2}}{p} \sum_{\substack{\ell j J \\ \mu m}} (-i)^{\ell+J}\, Y_{\ell\mu}(\hat{p}) \langle \ell\mu \tfrac{1}{2}\, \sigma | jm \rangle \langle jm I m_I | J{-\eta} \rangle \cdot \langle E,J,\pi;(Ij\ell;p) \| \hat{W}_\eta(q) \| 0 \rangle \tag{12}$$

where η can have the values ± 1 and 0 and indicates the different components of the electromagnetic transition densities.

The longitudinal component of the $\hat{W}$ operator in eq. (12) is related to the nuclear charge density. Explicitly it reads:

$$\hat{W}_0(q) \equiv 2 \int d\vec{r}\; j_J(qr) Y_J(\hat{r}) \hat{\rho}(\vec{r}) \tag{13}$$

where j_J indicates the spherical Bessel function. The definition of the transverse components, related with the current, is:

$$\hat{W}_\pm(q) \equiv (-i) \frac{\sqrt{J}}{[J]} \hat{S}_{J,J+1}(q) - (-i) \frac{\sqrt{J+1}}{[J]} \hat{S}_{J,J-1}(q) \mp \hat{S}_{J,J}(q) \tag{14}$$

where $[J]$ means $(2J+1)^{1/2}$, and we have defined;

$$\hat{S}_{J,\lambda}(q) \equiv \int d\vec{r}\; j_\lambda(qr)\; \vec{Y}_{J,\lambda,1}(\hat{r})\hat{J}(\vec{r}) \tag{15}$$

with $\vec{Y}_{J,\lambda,1}(\hat{r})$ indicating the vector spherical harmonics[36]. The expression of the charge, $\hat{\rho}(\vec{r})$, and current, $\hat{J}(\vec{r})$, operators is given in Appendix B.

In Born approximation, the cross section (6) involves products of the components of the transition currents which read explicitly:

$$J_\eta J^+_{\eta'} = \frac{32\pi^3}{p^2} \sum_{\ell jJ\pi} \sum_{\ell' j' J'\pi'} \langle E,J,\pi;(\ell jI;p) \| W_\eta \| 0\rangle$$

$$\langle 0 \| W^+_{\eta'} \| E,J',\pi';(\ell' j' I;p)\rangle \tag{16}$$

$$\cdot \sum_{\sigma m_I} A(J,\pi;\ell,j;J',\pi';\ell',j';\sigma,m_I,I;\eta,\eta';p)$$

where A is a product of Clebsh-Gordan coefficients and spherical harmonics:

$$A(J,\pi;\ell,j;J',\pi';\ell',j';\sigma,m_I,I;\eta,\eta';p)$$

$$\equiv \langle \ell(-\sigma-m_I-\eta)\, \tfrac{1}{2}\,\sigma | j(-m_I-\eta)\rangle \langle j(-m_I-\eta)\, I m_I | J-\eta\rangle$$

$$\cdot \langle \ell'(-\sigma-m_I-\eta')\, \tfrac{1}{2}\,\sigma | j'(-m_I-\eta')\rangle \langle j'(-m_I-\eta')\, I m_I | J'-\eta'\rangle \tag{17}$$

$$\cdot\, (-i)^{\ell-\ell'+J-J'}\; Y_{\ell,-\sigma-m_I-\eta}(\hat{p})\; Y^*_{\ell',-\sigma-m_I-\eta'}(\hat{p})$$

The coefficient defined in eq. (17) exhibits manifestly the difference between coincidence and one-arm experiments. In one-arm experiments, as widely discussed by de Forest and Walecka[30], one assumes that the nucleus makes a transition between states of definite angular momenta.

Since the longitudinal and the transverse components of the electromagnetic field carry different angular momenta along the direction of the transferred momentum $\vec{q}$ (0 and ± 1 respectively), they cannot interfere; otherwise they would lead to different final nuclear states. In the case of coincidence experiments, however, since the momentum $\vec{p}$ of the emitted particle is detected, the nuclear final state is not any more an eigenstate of the angular momentum of the target nucleus. Therefore the same final state is reached through different multipole excitations, which consequently are interfering with each other. It is clear that in this situation no constraint concerning the interference between the different components of the electro-magnetic field is present.

When the emitted particle is not detected, an integration over the momentum $\vec{p}$ of the emitted particle has to be performed in eq. (6). Because of the orthogonality properties of the spherical harmonics and of the Clebsh-Gordan coefficients, the coefficient defined in eq. (17) reduces to Kronecker deltas and consequently, only the diagonal terms in eq. (16) survive. In this way, the one-arm electron scattering cross section is retrieved.

The information about the angular distribution of the emitted particles is fully contained in the product of the two spherical harmonics of eq. (17). It appears clear that the dependence from the angle $_{p}$ between the direction of the emitted particle and the scattering plane is present only when $\eta \neq \eta'$, i.e. only in the interference terms I and S of eq. (6). Since

$$J_{-}J_{0}^{+} - J_{0}J_{+}^{+} = J_{0}J_{-}^{+} - J_{+}J_{0}^{+} \qquad (18)$$

and

$$J_-J_+^+ = J_+J_-^+ \tag{19}$$

the charge-current interference term depends on cos ${}_p$ only, whereas the current-current interference term depends on cos2 ${}_p$.

One has to remark that, since the associate Legendre polynomials $P_\ell^\mu(x)$ for x=1 differ from zero only when μ=0, for ϑ_p=0 and $\vartheta_p=\pi$, both the charge-current and the current-current interference term vanish, as well as one expected because in these situations the angle φ_p is not defined.

Now eq. (6) can be rewritten as:

$$\frac{d\sigma}{d\Omega_p dp d\Omega_{k_f} dk_f} = \frac{e^4}{2\varepsilon_i^3\varepsilon_f \sin^4\frac{\vartheta_e}{2}} \{V_S W_S + V_t W_t + 2V_I W_I \cos\varphi_p + 2V_S W_S \cos 2\varphi_p\} \tag{20}$$

with obvious meaning of the W coefficients. This is the expression of the coincidence cross section as it is known from the work of de Forest[31)]. One has to note that this author defined the V coefficients in a different way. The relation between the two different definitions of the V coefficients can be found in Ref. 37.

CHAPTER 2

The Nuclear Model

The multipole expansion eq. (10) of the nuclear final state requires a model for the excitation modes $|E,J,M,\pi;(I,\ell,j;p)\rangle$ which describes a system of A nucleons characterized by the excitation energy E, the total angular momentum J and parity π with at least one particle in the continuum.

The boundary conditions have to be chosen such that there is precisely one outgoing partial wave with total angular momentum j and orbital angular momentum ℓ, coupled to a residual nucleus with total angular momentum I. The momentum p of the outgoing particle is determined by the difference between the total excitation energy E and the energy of the residual nucleus.

In the present approach, the nuclear excited states are described within the continuum Random Phase Approximation by coherent superpositions of all one-particle one-hole (1p-1h) excitations relevant for a given range of excitation energies and momenta transfers:

$$
\begin{aligned}
|E,J,\pi;(c)\rangle = \sum_{c'=(p',h')} \int d\varepsilon' \; \Big[& X_{c,c'}(E,J,\pi;\varepsilon') \; [a^{+}_{p'}(\varepsilon') b^{+}_{h'}]_J \\
& - Y_{c,c'}(E,J,\pi;\varepsilon') \; [b_{h'} a_{p'}(\varepsilon')]_J \Big] |0\rangle
\end{aligned}
\tag{21}
$$

In eq. (21) the excitation energy has been denoted by E and the multipolarity of the mode has been associated with total angular momentum J and parity π. The projection quantum number M is never written down explicitly.

In the present model, all decay channels c are uniquely characterized by the quantum numbers of the particle p and of the hole state h involved which completely defines the state of the residual nucleus:

$$c \equiv \{p;h\} \equiv \{\varepsilon_p, \ell_p, j_p; \varepsilon_h, \ell_h, j_h\} \tag{22}$$

For convenience, also those configurations consisting of a bound particle state and a hole state are abbreviated by c and it is understood that the integration over the particle energy reduces to a summation in this case.

Note that, at a given excitation energy E above the emission particle threshold one has, in general, a set of degenerate wave functions because several channels c may be open for a particle emission. In eq. (21), the boundary conditions are such that the decay channel c is the only asymptotically outgoing channel.

In eq. (21) the particle and hole creation operators are represented by $a_p^+(\varepsilon)$ and b_h^+ and follow the anticommutation rules

$$\begin{aligned} \{a_p(\varepsilon), a_{p'}^+(\varepsilon')\} &= \delta_{pp'}\delta(\varepsilon-\varepsilon') \\ \{b_h, b_{h'}^+\} &= \delta_{hh'} \end{aligned} \tag{23}$$

The continuum RPA equations are briefly summarized in Appendix A.

Next we have to determine the expansion coefficients $X_{c,c'}$ and $Y_{c,c'}$. This is done in two steps: first, one solves the continuum RPA equations with boundary conditions which are easy to implement, second, one constructs the nuclear final state which is adequate for the physical process under consideration by making a suitable linear combination of the previous wave functions. The continuum RPA equations are:

$$
\begin{aligned}
&(\varepsilon-\varepsilon_h-E)\tilde{X}_{c_o,c}(E,J,\pi;\varepsilon) + \sum_{c'} \int d\varepsilon' \, [v^J_{c,c'}(\varepsilon,\varepsilon')\tilde{X}_{c_o,c'}(E,J,\pi;\varepsilon') \\
&+ u^J_{c,c'}(\varepsilon,\varepsilon')\tilde{Y}_{c_o,c'}(E,J,\pi;\varepsilon')] = 0 \\
&(\varepsilon-\varepsilon_h+E)\tilde{Y}_{c_o,c}(E,J,\pi;\varepsilon) + \sum_{c'} \int d\varepsilon' \, [v^{*J}_{c,c'}(\varepsilon,\varepsilon')\tilde{Y}_{c_o,c'}(E,J,\pi;\varepsilon') \\
&+ u^{*J}_{c,c'}(\varepsilon,\varepsilon')\tilde{X}_{c_o,c'}(E,J,\pi;\varepsilon')] = 0
\end{aligned}
\tag{24}
$$

The expression of the v and u matrix elements is given in Appendix A.

From the first of eqs. (24) it appears clear that the $\tilde{X}_{c_o,c}$ amplitudes have a pole for $\varepsilon=E+\varepsilon_h$. In order to treat this pole, we made the ansatz

$$
\begin{aligned}
&\tilde{X}_{c,c'}(E,J,\pi;\varepsilon') \equiv \delta_{c,c'}\delta(\varepsilon'-\varepsilon_{h'}-E) + P\,\frac{B_{c,c'}(E,J,\pi;\varepsilon')}{\varepsilon'-\varepsilon_{h'}-E} \\
&\tilde{Y}_{c,c'}(E,J,\pi;\varepsilon') \equiv \frac{C_{c,c'}(E,J,\pi;\varepsilon')}{\varepsilon'-\varepsilon_{h'}+E}
\end{aligned}
\tag{25}
$$

In eq. (25) P means the Cauchy's principal part distribution and $A_{cc'}$ is a constant which has to be determined from the asymptotic conditions. Using the ansatz (25) for the $\tilde{X}_{c,c'}$ and $\tilde{Y}_{c,c'}$ coefficients, the RPA equations (24) can be re-written as:

$$B_{c_o,c}(E,J,\pi;\varepsilon) + \sum_{c'} \int d\varepsilon' \, [v^J_{c,c'}(\varepsilon,\varepsilon') \frac{B_{c_o,c'}(E,J,\pi;\varepsilon')}{\varepsilon'-\varepsilon_{h'}-E}$$

$$+ u^J_{c,c'}(\varepsilon,\varepsilon') \frac{C_{c_o,c'}(E,J,\pi;\varepsilon')}{\varepsilon'-\varepsilon_{h'}+E}] = - \sum_{c'}^{cont} v^J_{c,c'}(\varepsilon,\varepsilon')A_{c_o,c'}\delta(\varepsilon'-\varepsilon_{h'}-E) \tag{26}$$

$$C_{c_o,c}(E,J,\pi;\varepsilon) + \sum_{c'} \int d\varepsilon' \, [v^{*J}_{c,c'}(\varepsilon,\varepsilon') \frac{C_{c_o,c'}(E,J,\pi;\varepsilon')}{\varepsilon'-\varepsilon_{h'}+E}$$

$$+ u^{*J}_{c,c'}(\varepsilon,\varepsilon') \frac{B_{c_o,c'}(E,J,\pi;\varepsilon')}{\varepsilon'-\varepsilon_{h'}-E}] = - \sum_{c'}^{cont} u^{*J}_{c,c'}(\varepsilon,\varepsilon')A_{c_o,c'}\delta(\varepsilon'-\varepsilon_{h'}-E)$$

Eqs. (26) form a system of N linearly independent equations, where N is the number of the open channels. If no channel is open all the terms on the right hand side of eqs. (26) are zero and the system becomes homongeneous. In this case the system has solutions different from the trivial one only if the determinant of the coefficients vanishes. The values of the excitation energy E, for which the determinant becomes zero, are the discrete resonance energies of the nucleus.

For any value of the excitation energy E above the continuum threshold, which is the case we are interested in, the system has always N linearly independent solutions. These solutions are, of course, determined by the value imposed to the known terms $A_{c,c'}$. As is shown in Appendix A, a convenient choice is:

$$A_{c,c'} = \delta_{c,c'} \tag{27}$$

The solutions $|\tilde{\Psi}(E,J,\pi)\rangle_c$ obtained using the choice (27) for the $A_{c,c'}$ coefficients have to be matched with the adequate boundary conditions.

Since the bound wave functions vanish for $r\to\infty$, only the continuum $\tilde{\chi}_{c,c'}$ amplitudes contribute asymptotically, therefore in coordinate space one has:

$$|\tilde{\Psi}(E,J,\pi;\vec{r})\rangle_c \underset{r\to\infty}{\to} \sum_{c'}^{\text{cont}} \int d\varepsilon' \, [\tilde{\chi}_{c,c'}(E,J,\pi;\varepsilon')R_{c'}(r,\varepsilon')\Omega_{c'}^{J^\pi}(A-1,\vec{r})] \tag{28}$$

where $\Omega_c^{J^\pi}$ indicates the surface function[39)]

$$\Omega_c^{J^\pi}(A-1,\vec{r}) \equiv \frac{1}{r}\sum_{m_p m_h} \langle j_p m_p j_h m_h | JM\rangle \, \vec{Y}_{j_p \ell_p}^{m_p}(\hat{r})\Phi_{j_h m_h}(\vec{r}_1-\vec{r}_{A-1}) \tag{29}$$

In eq. (28) we indicate the solution of the reduced radial Schrödinger equation for a particle scattered by a spherical potential; its asymptotic behaviour is:

$$R_c(r,\varepsilon) \underset{r\to\infty}{\to} \sin(pr - \frac{\ell_p}{2}\pi + \chi_c) \tag{30}$$

where χ refers to the sum of the nuclear and Coulomb phase-shifts and p is the momentum associated with the energy ε of the particle.

Using the ansatz (25) for the $\tilde{\chi}_{c,c'}$ coefficients with the choice (27) of the $A_{c,c'}$ known terms, the asymptotic expression of the nuclear final state can be written as[38)]:

$$\begin{aligned}|\tilde{\Psi}(E,J,\pi;\vec{r})\rangle_c \underset{r\to\infty}{\to} \sum_{c'}^{\text{cont}} &\{\delta_{c,c'}\sin(pr - \frac{\ell_p}{2}\pi + \chi_{c'})\Omega_{c'}^{J^\pi}(A-1,\vec{r}) \\ &+ \pi\, B_{c,c'}(E,J,\pi;\varepsilon')\cos(pr - \frac{\ell_p}{2}\pi + \chi_{c'})\Omega_{c'}^{J^\pi}(A-1,\vec{r})\}\end{aligned} \tag{31}$$

Defining the incoming and outgoing waves as:

$$I_c(p,\vec{r}) \equiv e^{-i(pr - \frac{\ell_p}{2}\pi)}\ \Omega_c^{J^\pi}(A-1,\vec{r})$$

$$O_c(p,\vec{r}) \equiv e^{i(pr - \frac{\ell_p}{2}\pi)}\ \Omega_c^{J^\pi}(A-1,\vec{r}) \tag{32}$$

Eq. (31) can be re-written as:

$$\left|\tilde{\Psi}(E,J,\pi;\vec{r})\right\rangle_c \underset{r\to\infty}{} \to \frac{i}{2}\sum_{c'} \{e^{-i\chi_{c'}}\ [\delta_{c,c'}-i\pi B_{c,c'}(E,J,\pi;\varepsilon')]\, I_{c'}(p',\vec{r}) - e^{+i\chi_{c'}}\left[\delta_{c,c'}+i\pi B_{c,c'}(E,J,\pi;\varepsilon')\right] O_{c'}(p',\vec{r})\ \} \tag{33}$$

The nuclear final state corresponding to the emission of one particle, eq. (10), is characterized by the presence of only one particle in an outgoing channel. This can be achieved by making a linear combination of the states of eq. (33) as follows:

$$|E,J,\pi;(c)\rangle = \sum_{c'\text{open}} e^{-i\chi_{c'}}\ [1+i\pi B(E,J,\pi;\varepsilon')]^{-1}_{c,c'}\ |\tilde{\Psi}(E,J,\pi)\rangle_{c'} \tag{34}$$

Here 1 indicates the unit matrix. Explicitly, the asymptotic expansion of eq. (11) reads:

$$\langle r|E,J,\pi;(c)\rangle \underset{r\to\infty}{\to} \frac{-i}{2}\ [O_c(p,\vec{r}) - \sum_d R_{c,d}\ I_d(p_d,\vec{r})] \tag{35}$$

with the R matrix defined as:

$$R_{c,d} = e^{-i\chi_c} \sum_f \, [1+i\pi B(E,J,\pi;\varepsilon_f)]^{-1}_{c,f}$$
$$\cdot \, [1-i\pi B(E,J,\pi;\varepsilon_d)]_{f,d} \, e^{-i\chi_d} \qquad (36)$$

If the particle-hole interaction vanishes the matrix of the B coefficients becomes zero, then the channel-to-channel coupling is suppressed and the quasi-free scattering limit is retrieved.

Whereas in inclusive experiments, where the emitted particle is not detected, one has to sum over all the possible states of the residual nucleus, in the present situation only those decay channels contribute which leave the residual nucleus in a definite state with angular momentum I. In our model this state is the hole state h.

Using the explicit representation eq. (34) for the final nuclear state to calculate the product of two components of the transition current $J_\eta J^+_{\eta'}$, one has to evaluate terms like:

$$e^{-i\chi_c}[1 + i\pi B(E,J,\pi;\varepsilon_d)]^{-1}_{c,d} \, ([1 + i\pi B(E,J,\pi;\varepsilon_{d'})]^{-1}_{c',d'})^{+} \, e^{+i\chi_{c'}} \qquad (37)$$

Using the properties of hermiticity and symmetry of the matrix of the B coefficients, with the help of some algebra it is possible to show that the expression (37) is equal to:

$$e^{-i(\chi_c-\chi_{c'})}\{[1 + \pi^2B^2]^{-1}_{c,d} \, [1 + \pi^2B^2]^{-1}_{c',d'}$$
$$+ \pi^2 \sum_f \, [1 + \pi^2B^2]^{-1}_{c,f} \, B_{f,d} \sum_{f'} B_{c',f'} \, [1 + \pi^2B^2]^{-1}_{f',d'}\} \qquad (38)$$

Defining two new quantities:

$$N(E,J,\pi;c;\eta) \equiv \sum_{d} \langle 0 \| W_{\eta} \| \tilde{\Psi}(E,J,\pi)\rangle_{d} \, [1+\pi^2 B^2]^{-1}_{d,c}$$

and (39)

$$P(E,J,\pi;c;\eta) \equiv \sum_{d} \langle 0 \| W_{\eta} \| \tilde{\Psi}(E,J,\pi)\rangle_{d} \, \sum_{f} [1+\pi^2 B^2]^{-1}_{d,f} \, B_{f,c}$$

the product of two components of the transition current eq. (16) explicitly reads:

$$\begin{aligned} J_{\eta} J^{+}_{\eta'} = \frac{32\pi^3}{p^2} & \sum_{J,\pi,c=(\ell_c,j_c;I_c=I)} \; \sum_{J',\pi',c'=(\ell_{c'},J_{c'};I_{c'}=I)} \\ & [N(E,J,\pi;c;\eta) N^{+}(E,J',\pi';c';\eta') \\ & + \pi^2 P(E,J,\pi;c;\eta) P^{+}(E,J',\pi';c';\eta')] \times e^{-i(\chi_c - \chi_{c'})} \\ & \times \sum_{m_I \sigma} A(J,\pi;\ell_c j_c;J',\pi';\ell_{c'} j_{c'};\sigma,m_I,I;\eta,\eta';p) \end{aligned} \quad (40)$$

The transition matrix elements between the ground state and the excited state $|\tilde{\Psi}(E,J,\pi)\rangle_c$ is reduced to sums over one-body matrix elements as follows:

$$
\begin{aligned}
{}_c\langle\tilde{\Psi}(E,J,\pi)\|W_\eta\|0\rangle = \sum_{\substack{c'=[p',h'] \\ (\text{bound})}} & [X_{c,c'}(E,J,\pi)\langle p'\|W_\eta\|h'\rangle \\
& + (-)^{J+j_{p'}-j_{h'}}\, Y_{c,c'}(E,J,\pi)\langle h'\|W_\eta\|p'\rangle] \qquad (41) \\
& + \sum_{c'=[p',h']} [P \int d\varepsilon' \, \frac{B_{c,c'}(E,J,\pi;\varepsilon')}{\varepsilon'-\varepsilon_{h'}-E} \langle p'(\varepsilon')\|W_\eta\|h'\rangle \\
& + (-)^{J+j_{p'}-j_{h'}} \int d\varepsilon' \, \frac{C_{c,c'}(E,J,\pi;\varepsilon')}{\varepsilon'-\varepsilon_{h'}+E} \langle h'\|W_\eta\|p'(\varepsilon')\rangle] \\
& + \langle p(\varepsilon=E+\varepsilon_h)\|W_\eta\|h\rangle
\end{aligned}
$$

The explicit expression of the single particle transition matrix elements $\langle p\|W_\eta\|h\rangle$ for the different electro-magnetic operators is given in Appendix B.

CHAPTER 3

Numerical Details

The single-particle wave functions have been generated using a Saxon-Woods potential of the form:

$$V(r) = \frac{-V_o}{1+\exp((r-R_o)/a_o)} - \left(\frac{\hbar}{m_\pi c}\right)^2 V_{SO} \frac{\vec{\ell}\cdot\vec{\sigma}}{r} \frac{d}{dr} \left[1 + \exp((r-R_{SO})/a_{SO})\right]^{-1} + V_c(r) \tag{42}$$

where m_π is the pion mass and $V_c(r)$ is the Coulomb potential

$$V_c(r) = \begin{cases} \frac{Ze^2}{2R_c}\left[3-(r/R_c)^2\right] & r<R_c \\ \frac{Ze^2}{r} & r>R_c \end{cases} \tag{43}$$

created by a uniform charge distribution of radius R_c.

In ^{16}O the parameters of the potential (see Table 1) have been fixed fitting the experimental single-particle energies in the vicinity of the Fermi level.

In Table 2 we compare the bound single-particle energies obtained using this parametrization of the Saxon-Woods potential with the experimental values deduced from the level schemes of the neighbouring nuclei[40]. This Saxon-Woods potential gives an rms charge radius of 2.69 fm close to the experimental one[41] of 2.73±0.025 fm.

Though ^{12}C is soft against nuclear deformation, a spherical approximation to the ground state of ^{12}C was employed, since the occupied Nilsson orbits show no level crossing with the unoccupied ones, at least for deformation parameters less than $\beta = 0.3$ [42,43].

The experimental splitting between the bound $p_{3/2}$ and $p_{1/2}$ levels is 14.0 MeV for protons and 13.8 MeV for neutrons. This splitting cannot be reproduced by spin-orbit forces of Saxon-Woods potentials developed for spherical nuclei[44]. Therefore we extrapolated the Saxon-Woods parameters from other spherical nuclei and chose the spin-orbit strength such as to reproduce the splitting between the $d_{5/2}$-$d_{3/2}$ continuum waves (see Table 1).

In both nuclei, ^{12}C and ^{16}O, the same Saxon-Woods potential used to generate the bound single-particle wave functions was also used to generate the continuous ones. This was done by solving the Schrödinger equation for positive energy eigenvalues up to 400 MeV.

In each of the two nuclei under consideration, the model space used in the continuum RPA computations was composed by all the bound states and by the continuous ones up to the $j_{15/2}$, $j_{13/2}$ waves for both, protons and neutrons, giving a total number of 30 partial waves.

For ^{16}O the continuum RPA equations have been solved using the experimental values of the bound single particle energies given in Table 2.

Also in the computations performed in ^{12}C we used the experimental single particle energies (see Table 3) with the exception of the $1p_{1/2}$ states. The huge energy gap between occupied and unoccupied levels in ^{12}C is probably due to deformation effects, then, to be consistent with our spherical approximation, we changed the energies of the $1p_{1/2}$ states in order to reproduce the energy gap given by the spherical Saxon-Woods potential. The values of the single particle energies of the $1p_{1/2}$ states we used in the continuum RPA equations are -13.5 MeV and -16.24 MeV respectively for protons and neutrons. We found, however, that in our calculations the electro-scattering coincidence cross section is not sensitive to the $1p_{1/2}$ bound levels.

The residual particle-hole interaction used is the zero-range density dependent Landau-Migdal force

$$V_{ph} = C_0[f_0(\rho)+f_0'(\rho)\vec{\tau}_1\cdot\vec{\tau}_2+g_0\vec{\sigma}_1\vec{\sigma}_2+g_0'(\vec{\sigma}_1\cdot\vec{\sigma}_2)(\vec{\tau}_1\cdot\vec{\tau}_2)] \tag{44}$$

where the density dependence is given by

$$f_0(\rho(r) = f_0^{ext} + (f_0^{int}-f_0^{ext})\rho(r)$$

$$\rho(r) = \frac{1}{1+\exp((r-R)/a)} \tag{45}$$

with R indicating the interpolation radius. The values of the force parameters, given in Table 5, have been chosen following Ref. 45. Note that this parametrization of the force has been fixed by fitting excitation energies, transition rates, electric and magnetic moments as well as isotope shifts in the lead region.

For the application to ^{12}C and ^{16}O we modified only the value of the overall constant C_0 and, of course, the interpolation radius R which scales with $A^{1/3}$. In ^{16}O the overall constant C_0 has been fixed by reproducing the lowest collective 3^- excited state at 6.13 MeV (see Table 5). The value of 193.0 MeV fm^3 used for the force constant C_0 in ^{12}C was extrapolated from Oxygen. With this value of C_0, within the present model, the first excited 2^+ state in ^{12}C is found at 5.74 MeV, while experimentally it comes at 4.44 MeV, and the first 3^-

state is obtained at 11.99 MeV, which has to be compared with the experimental value of 9.64 MeV.

Following the criteria discussed in Ref. 46, we used 15 Fourier-Bessel expansion coefficients in order to ensure the numerical stability of the method.

CHAPTER 4

Application to ^{16}O

^{16}O is one of the best studied nuclei, from the experimental as well as from the theoretical point of view. Since the 1p-1h continuum RPA gives a rather successful description of the excited states of this nucleus[47], ^{16}O is an ideal case to test the validity of our model and to probe the possibilities offered by coincidence electron-scattering experiments to investigate the decay of giant resonances.

a) Photoabsorption Cross Section

In Fig. 3 the theoretical total photoabsorption cross section, obtained including the contribution of the 1^-, 2^+, 3^- multipole modes is shown as a function of the excitation energy. The experimental data are taken from Ahrens et al.[48]. As expected in a configuration space limited to 1p-1h excitations, the magnitude of the cross section is overestimated by roughly a factor 2 in the vicinity of the dipole resonance, and correspondingly, the width of the resonance is underestimated.

Since the total photoabsorption cross section is practically sensitive only to the electric dipole excitation (in the energy range up to 40 MeV the 1^- contributes 97.1 % to the total cross section), in Fig. 3 only the validity of the 1^- solution of the continuum RPA has been tested.

The same underestimation of the spreading width and overestimation of the resonance peak applies to all other multipole modes as well, of course. These problems would be cured to a large extent by the inclusion of 2p-2h degrees of freedom, which so far were included only in calculations with a discretized continuum[49)].

The fact that the peak energy of the dipole resonance is 1.2 MeV larger than the experimental one may be traced back to the value of the parameter f_0' which determines the strength of the isospin-flip. The value of f_0' was fixed in Ref. 45 such as to reproduce the excitation energy of the dipole resonance of ^{208}Pb. This value of f_0' produces a symmetry energy of β = 53 MeV [2)], which is almost a factor of 2 larger than the bulk symmetry energy[50)] and of the value of 27.6 MeV obtained starting from a one-boson exchange potential by Nakayama et al.[51)]. This discrepancy led Brown, Dehesa and Speth to surmise that the large excitation energy of the giant dipole mode is due to the influence of 2p-2h degrees of freedom[52)], which the fitted value of f_0' takes effectively into account. Since the density of 2p-2h states is larger in ^{208}Pb as compared to ^{16}O, the value of f_0' = 1.5 overestimates the 2p-2h effects in ^{16}O, and consequently produces a too repulsive interaction.

b) Sensitivity of the Coincidence Cross Section to the Presence of Weak Multipole Modes

One of the motivations to perform coincidence experiments in the giant resonance region is given by the possibility to explore the distribution of multipole strength which is too weak to produce clear signatures in a one-arm experiment. In this chapter, we want to investigate in a quantitative way to which extent modes of large multipolarity influence the coincidence cross section.

A rough estimate whether a multipole mode of angular momentum J contributes to the coincidence cross section at a fixed momentum transfer q may be obtained as follows: if the nucleus is considered to be a homogeneous sphere of radius R, the overlap of the component $j_J(qr)$ of the virtual photon wave function with the nucleus will vanish for very large multipolarities.

Demanding that the value of the Bessel function at the edge of the nucleus be less than 0.01 for all multipolarities larger than a cut-off multipolarity J_{cut}, one is led to the condition:

$$\frac{(qR)^{J_{cut}}}{(2J_{cut}+1)!!} < 0.01 \tag{46}$$

Here the Bessel function has been approximated by the first term of the ascending expansion. Using $R = 1.2\ A^{1/3}$ as a reasonable approximation for the nuclear radius, for $q = 0.5\ fm^{-1}$ the cut-off J_{cut} results to be about 4, while for $q = 1\ fm^{-1}$ one obtains $J_{cut} \doteq 5$.

In Figs. 4, 5 and 6 we display the coincidence cross sections for the reaction $^{16}O(e,e'p_0)^{15}N$. The kinematical conditions are arranged such as to cover momentum transfers between $q = 0.6\ fm^{-1}$ and $q = 1.2\ fm^{-1}$. The cross sections are shown as a function of the proton scattering angle ϑ_p. The values $0^o < \vartheta_p < 180^o$ correspond to $\varphi_p = 0^o$, while the values $180^o < \vartheta_p < 360^o$ correspond to $\varphi_p = 180^o$. Recall that in the present choice of the coordinate system, a direct knock-out process would favour particle emission in the direction $\vartheta_p = 180^o$. In Fig. 4, the energy of the incident electron is $\varepsilon_i = 100$ MeV, while the excitation energy of the nucleus is E = 23 MeV corresponding to the maximum of the dipole resonance. The electron scattering angle of $\vartheta_e = 90^o$ gives a momentum transfer $q = 0.64\ fm^{-1}$.

According to the estimate, eq. (46), one would expect that multipolarities larger than J=4 are clearly negligible. Indeed, the actual calculation shows that already the multipole modes with J=4 (full line in Fig. 4a) give only a tiny correction to the cross section calculated with the modes $J^{\pi} = 0^{+}$, 1^{-} and 2^{+} alone (dashed line). With increasing momentum transfer the importance of multipole modes with larger angular momentum increases, of course. At a backward angle $\vartheta_e = 165^0$ of the electron, the momentum transfer has increased to $q = 0.89\ fm^{-1}$, Fig. 4b. Now the multipole modes $J^{\pi} = 0^{+}$, 1^{-} and 2^{+} produce only almost half of the cross section (dashed line), while clearly the multipole modes up to J=4 contribute the other half of the cross section (solid line). Note that multipole modes with $J \geqslant 4$ do not produce any sensitive change in Fig. 4 as expected from eq. (46).

At the nuclear excitation energy of E = 40 MeV, Fig. 5, one is sensitive only to the high energy tail of the giant dipole resonance. Here one would expect that coincidence experiments might provide information about the distribution of strength of larger multipolarities. Indeed at $\vartheta_e = 90^0$ which corresponds to a momentum transfer of $0.54\ fm^{-1}$, Fig. 5a, the multipolarities up to J=4 (continuous line) enhance the cross section computed with $J^{\pi} = 0^{+}$, 1^{-} and 2^{+} alone by roughly 40 % at the forward angle $\vartheta_p = 180^0$.

Multipolarities beyond J=5 produce negligible effects in agreement with eq. (46) (dotted line). At $\vartheta_e = 165^0$, Fig. 5b, the effects of the larger multipolarities come out even more clearly, but the relatively large momentum transfer of $q = 0.8\ fm^{-1}$ implies cross sections which are at the limit of what can probably be detected experimentally. In order to check the performance of the cut-off condition, eq. (46), we pushed the momentum transfer up to $q = 1.16\ fm^{-1}$ in Fig. 6. The nuclear excitation energy of 40 MeV is in a transition region between strong channel-to-channel coupling of the giant resonances and the quasi-free scattering. The angular distribution of the emitted proton should predominantly be determined by the Fourier transformation of a $p_{1/2}$-hole state. Indeed, a minimum in the cross section at $\vartheta_p = 180^0$ is seen which is characteristic of a p-wave. As expected from eq. (46), multipolarities up to J=5 (dashed line) have to be included in order to bring out this effect.

The search for monopole strength has been one of the exciting topics in the study of giant resonances because of the connection with the nuclear compression modulus. In light nuclei it is too fragmented to be unambiguously identified with one-arm experiments. We applied our modelto look for characteristic signatures of the monopole mode in ^{16}O.

In order to minimize the overwhelming presence of the giant dipole resonance we choose the excitation energy E = 20 MeV which lies in a minimum of the theoretical photoabsorption cross section (see Fig. 3). When searching for weak multipole modes one has to find a compromise between two objectives: first one would like to choose the momentum transfer which is optimal for the excitation of the weak mode, second the momentum transfer should be as small as possible in order to have reasonably large cross sections.

The optimal response of the nucleus to the electric monopole excitation results to be at q = 0.6 fm^{-1} in the present investigation.

We performed calculations with an energy of the incoming electron ε_i = 100 MeV changing the scattering angle ϑ_e of the electron in order to modify the values of the momentum transfer.

At $\vartheta_e = 90^0$ corresponding to a momentum transfer of 0.63 fm^{-1} the coincidence cross section turns out to be less than 3 nb/(MeV²sr²). In Fig. 7 we therefore display the results for the scattering angles $\vartheta_e = 40^0$ and $\vartheta_e = 60^0$. In both figures the full lines represent the result obtained including all the multipole modes up to J=4 and the dashed lines are showing the results obtained leaving out the monopole mode. In both cases the presence of the monopole strongly modifies the shape of the angular distribution with a pronounced enhancement at backward angle $\vartheta_p = 0^0$.

At $\vartheta_e = 40^0$ the coincidence cross section at $\vartheta_p = 0^0$ reaches a value of 16 nb/(MeV²sr²). Even though probably it has to be reduced by roughly a factor 2 because of 2p-2h effects, this order of magnitude of the cross section is accessible experimentally.

c) Symmetry Breaking Effects

The reflection symmetry

$$d\sigma(180^0-\vartheta_p) = d\sigma(180^0+\vartheta_p) \qquad (47)$$

is broken by the charge-current interference term, denoted with I in eq. (20), which depends explicitly on $\cos\varphi_p$. Qualitatively, the relative importance of the four individual terms may be inferred from the kinematical coefficients V_C, V_T, V_I and V_S (eq. (7)) which are displayed as a function of the electron scattering angle in Fig. 8 for an incoming electron energy of ε_i = 100 MeV and energy loss of 23 MeV. The coefficients V_I and V_S which are absent in a one-arm experiment roughly follow the charge coefficient V_C concerning magnitude and shape. At $\vartheta_e = 180^o$, however, the charge-current interference term V_I vanishes much more slowly than the charge-charge term V_C and the current-current term V_I.

Collective states of natural parity, in general display large charge transition densities, whereas the corresponding current densities are comparatively much more smaller.

The individual contributions of the four interference terms to the coincidence cross section, at the theoretical peak energy of 23 MeV of the giant dipole resonance, are shown as a function of the proton angle ϑ_p for the electron scattering angle $\vartheta_e = 90^o$ (Fig. 9) and $\vartheta_e = 165^o$ (Fig. 10). At $\vartheta_e = 90^o$ the coincidence cross section is clearly dominated by the charge-charge term, while at $\vartheta_e = 165^o$, the current-current term starts to become the most important one, as one would expect from one-arm electron scattering experiments and the behaviour of the kinematical coefficients displayed in Fig. 8.

The contribution due to the interference between the components J_+ and J_- of the transverse current is almost negligible both at $\vartheta_e = 90^o$ and in particular at $\vartheta_e = 165^o$.

On the other hand, the charge-current interference term produces a contribution to the coincidence cross section which leads to a clearly recognizable breaking of the reflection symmetry (47) in Figs. 4, 5, 6. Consequently, the charge-current interference term should not be left out in any analysis of coincidence experiments.

The fact that the forward-backward symmetry

$$d\sigma(\vartheta_p) = d\sigma(180^o+\vartheta_p) \qquad (48)$$

may be broken in coincidence experiments if two multipole modes of opposite parity overlap is generally referred to as a Bohr theorem[53].

In our model this fact can easily be seen because the angular distribution of the emitted particle is completely determined by the product of the two spherical harmonics of eq. (17). Then, taking out the dependence from the angle φ_p, which is explicitly taken into account in eq. (20), one has to consider the product between two factors of this kind:

$$F^{\mu}_{\ell}(\ _p) = (-)^{\mu} \frac{[\ell]}{\sqrt{4\pi}} \left[\frac{(\ell-\mu)!}{(\ell+\mu)!}\right]^{1/2} P^{\mu}_{\ell}(\cos\vartheta_p) \qquad (49)$$

where P^{μ}_{ℓ} is the Legendre polynomial and $\mu=-\sigma-m_I-\eta'$ following the notation of eq. (17).

Using the effective ϑ'_p defined between 0 and 2π, (recall that this simplifies the plotting of the angular distribution), one finds the relation:

$$F^{\mu}_{\ell}(\vartheta'_p+\pi) = (-)^{\ell} F^{\mu}_{\ell}(\vartheta'_p) \qquad (50)$$

Then the forward-backward symmetry is related with:

$$F^{\mu}_{\ell}(\vartheta'_p+\pi)F^{\mu'}_{\ell'}(\vartheta'_p+\pi) = (-)^{\ell+\ell'} F^{\mu}_{\ell}(\vartheta'_p)F^{\mu'}_{\ell'}(\vartheta'_p) \qquad (51)$$

where ℓ and ℓ' are the orbital quantum numbers of the emitted particle. Because one detects a particle coming from a fixed hole state with orbital angular momentum ℓ_h the phase of eq. (51) becomes

$$(-)^{\ell+\ell'} = (-)^{\ell+\ell_n} (-)^{\ell'+\ell_n} = (-)^{\pi} (-)^{\pi'} \tag{52}$$

where π and π' are, by definition, the parities of the nuclear excited states.

It is clear now that the phase of eq. (51) is equal to one only if the two nuclear excited states have the same parity.

d) Energy and Momentum Dependence of the Coincidence Cross Section

In Fig. 11 we show the coincidence cross section for the reaction $^{16}O(e,e'p_0)^{15}N$ as a function both of the nuclear excitation energy and of the angle of the emitted proton. This calculation has been performed keeping fixed the energy of the incoming electron at ε_i = 100 MeV and the scattering angle at $\vartheta_e = 90^0$. The nuclear excitation energy was changed by varying the energy of the detected electron in steps of 0.25 MeV. Because of this energy variation the value of the momentum transfer varies from q = 0.66 fm^{-1} to 0.61 fm^{-1} as one goes from the particle emission threshold to E = 40 MeV. The proton, knocked-out from the $1p_{1/2}$ bound level, is detected in the scattering plane. All the multipole excitation modes up to J=4 are included.

In Fig. 11 one can distinguish three regions: a first one, starting at the particle emission threshold and going up to about 22 MeV, is characterized by the presence of sharp resonances, a second region containing the huge bump of the giant resonances, and, after that, a third region in which the angular distribution of the emitted particle is mainly concentrated in the direction of the transferred momentum.

At the peak energy of E = 23.5 MeV the strong forward-backward asymmetry presented by the angular distribution of the emitted particle is a clear signature of the presence of large interference terms between the electric dipole and quadrupole excitation modes.

Within the present model, the peak of the electric quadrupole resonance lies at 23.5 MeV excitation energy, see Fig. 12, while experimentally[54,8] the centroid energy of the resonance is known to be at ~ 21 MeV. This discrepancy has to be ascribed to our choice of the Saxon-Woods potential which gives a too high resonance energy for the continuum proton and neutron $f_{7/2}$ waves. Recall that the coupling of the $f_{7/2}$ partial wave with the $p_{3/2}$ hole states generates the particle-hole configuration with the largest contribution to the isoscalar giant quadrupole[55].

Note, however, that the present model produces a large overlap between the electric giant dipole and quadrupole resonances (compare Fig. 12 with Fig. 3), as it is known experimentally. The strong effects of the interference between dipole and quadrupole modes appear clearly in Fig. 13 where the angular distribution at the excitation energy of E = 23.5 MeV of Fig. 11 (full line) is compared with the result of calculations performed leaving out the 2^+ (dashed line) and 1^- (dotted line). In both calculations the forward-backward symmetry is rather well conserved, as well as one expects in the case that the angular distribution is strongly dominated only by one isolated resonance. In forward direction, $\vartheta_p = 180^0$, the values of the cross section given by the calculations performed without 2^+ and 1^- are respectively 10.2 and 28.1 nb/(MeV²sr²). Since at this angle, $\vartheta_p = 180^0$, the value of the coincidence cross section computed including all the multipole modes is 59.3 nb/(MeV²sr²), one concludes that the interference between 1^- and 2^+ gives a constructive contribution resulting in an enhancement of about 55 % of the incoherent sum of the two contributions.

The relative importance of the two modes can be changed by changing the value of the momentum transfer. In Fig. 14 the momentum dependence of the individual contribution of the dipole and quadrupole modes to the $^{16}O(e,e'p_0)^{15}N$ cross section at the proton angle $\vartheta_p = 180^0$ and at the excitation energy E = 23.5 MeV is shown. The value of the angle of the scattered electron was kept fixed at $\vartheta_e = 90^0$. The value of the transferred momentum was changed by changing the energy of the incoming electron.

From Fig. 14 one can see that for the momentum transfer q = 0.63 fm^{-1}, which is the value of the momentum transfer involved in the calculations of Fig. 13, the contributions of the 1^- and 2^+ resonances to the coincidence cross section have the same order of magnitude. This fact originates the big effects of the interference between the two multipole modes we have shown in Fig. 13. Increasing the momentum transfer, the influence of the dipole resonance is reduced. Since, in ^{16}O, multipole modes of multipolarity larger than 2^+ are no longer expected to form energetically concentrated resonances, one may study predominantly the strength distribution of the quadrupole resonance by increasing the value of the momentum transfer.

Fig. 15 shows the result of a computation analogous to the one of Fig. 11 where, to probe the momentum region going from q = 1.15 fm^{-1} to q = 1.23 fm^{-1}, we have increased the energy ε_i of the incoming electron at 180 MeV keeping the same value of the scattering angle $\vartheta_e = 90^0$. In this calculation the stability of the angular distribution was obtained inserting all the positive and negative multipole modes up to J=6.

In Fig. 15, at the peak energy of E = 23.5 MeV, the angular distribution of the emitted particle presents a rather well conserved forward-backward symmetry which indicates the presence of one multipole excitation mode which strongly dominates all the other ones. The sensitivity of the angular distribution of the emitted particle at the peak energy E = 23.5 MeV to the electric quadrupole and dipole excitation modes is analysed in Fig. 16. There the result of the calculation of Fig. 15 (full line) is compared with the results of the calculations performed without 2^+ (dashed line) and without 1^- (dotted line). Fig. 16 clearly shows that, at $q = 1.2\ fm^{-1}$, the electric quadrupole excitation gives the main contribution to the coincidence cross section, while the presence of the electric dipole and of the other multipole modes generates a weak breaking of the forward-backward symmetry.

If one compares Fig. 11 with Fig. 15 one can see that in the region before the giant resonance bump a lot of the structure present at low momentum transfer disappears at high q. The sharp resonance at E = 19MeV, however, is present in both cases.

The solution of the continuum RPA equations for the 3^- multipole resonance shows a sharp peak at 19 MeV (see Fig. 17) and in effect we found that the sharp bump at E = 19 MeV in the $^{16}O(e,e'p_0)^{15}N$ cross section is due to the excitation of the electric octupole mode (see Fig. 18). This state mainly consists of a $1d_{5/2}$ particle coupled with a $1p_{3/2}$ hole state[55]. Even though this state has no dominant components in the single-particle continuum, the coupling with the continuum is sufficiently strong to make this state accessible to investigations with coincidence techniques. This state may be identified with the isovector 3^- state found experimentally at 19.21 MeV excitation energy in pick-up reaction with a ^{17}O target[56,57].

The large selectivity of the coincidence electron scattering experiments is demonstrated in Fig. 16 where the kinematic conditions of Fig. 15 have been deep, i.e. the energy of the incoming electron is ε_i = 180 MeV and the scattering angle of the electron is $\vartheta_e = 90^o$, but the residual nucleus is left in the $p_{3/2}$ state.

The sharp bump at the excitation energy E = 20MeV, dominated by the current transition density (see Fig. 20), is due to the excitation of the 4^- state (see Fig. 21). This 4^- state, in our model is practically composed only by the $(1d_{5/2}, 1p_{3/2}^{-1})$ particle-hole configurations; the coupling with the $1p_{1/2}$ hole state is so weak that, in the $^{16}O(e,e'p_o)^{15}N$ reaction of Fig. 15 no 4^- state was seen.

Experimentally[56,58,59] one finds four peaks of multipolarity 4^- in the 18-19 MeV region. Our approach gives two 4^- peaks, one isovector, the other isoscalar. In Fig. 16 they are not resolved because we used an energy resolution of 0.25 MeV. The additional splitting in the other two peaks is probably due to the coupling with 3p-3h configurations, as widely discussed by Barker et al.[60].

e) Effects of the Channel-to-Channel Coupling and Quasi-Free Behaviour

In Figs. 11, 15 and 19, at energies above the giant dipole resonance, particle emission is predominantly concentrated along the direction of the momentum transfer. The question immediately arises, whether a quasi-free knock-out process already takes place at the comparatively low excitation energies starting at about 30 MeV. Since the present model contains the quasi-free scattering as a limiting case when the particle-hole interaction vanishes, the problem can be tackled by comparing two calculations performed with and without residual interaction.

In Fig. 22 the full line represents the angular distribution of the emitted particle of Fig. 11 at the peak energy of E = 23.5 MeV. In the same figure the dashed line represents the result of the calculation performed switching off the residual interaction. The large difference between the two calculations of Fig. 22 is not astonishing since they have been performed at the peak energy of the giant resonance, where collective degrees of freedom are fundamental ingredients of the nuclear excitation mechanism.

In an extreme quasi-free scattering picture, where the wave function of the emitted particle is considered to be a plane wave, and the nucleus is described in the Independent Particle Shell Model, the angular distribution of the emitted particle results to be proportional to the Fourier transformation of the hole wave function[61]:

$$\frac{d^4\sigma}{d\Omega_p dp d\Omega_{k_f} dk_f} \sim \left| \int drr^2 \, e^{i(\vec{p}-\vec{q})\cdot\vec{r}} \varphi_h(\vec{r}) \right|^2 \qquad (53)$$

The dashed line of Fig. 22 shows the characteristic angular distribution of a particle knocked-out from a p-shell, when the quasi-free kinematical conditions are fulfilled.

There are two reasons why the cross section calculated without residual interaction is not exactly zero at $\vartheta_p = 180^o$, as one would expect from eq. (53). The first reason is due to the fact that in the kinematic conditions of Fig. 22 the magnitude of momentum transfer $\vec{q}$ is not exactly equal to the magnitude of the momentum $\vec{p}$ of the emitted particle.

The second reason has a more general origin. Even though the p-h interaction is zero, the emitted particle is still interacting with the residual nucleus through the central Saxon-Woods potential. This breaks the simple picture leading to eq. (7) since the wave function of the emitted particle is not any more a plane wave.

In Figs. 23 and 24 we compare the results of calculations performed with (full line) and without (dashed line) residual interaction for the nuclear excitation energy E = 40 MeV. The two calculations of Figs. 23 and 24 have been performed for two different values of the energy of the incoming electron.

The kinematic conditions of Fig. 23, where the same value of the incoming electron energy ε_i = 100 MeV of Fig. 22 is kept, allowed a minimum value of $\vec{p}-\vec{q}$ of 0.6 fm^{-1}. This means that only the external tail of the Fourier transformation (53) is probed, and the two bumps of the dashed line of Fig. 22 merge in Fig. 23 in a unique bump peaked around ϑ_p =180°.

On the other hand, in Fig. 24 the kinematic conditions have been fixed such as $\vec{p} = \vec{q}$ and the angular distributions show the characteristic p-wave behaviour. The asymmetry between the two peaks of the angular distribution is due to the $\cos\varphi_p$ dependence of the charge-current interference term (see eq. (20)). The position of these two peaks around $\vec{p}-\vec{q}$ = 0.45 fm^{-1} is in good agreement with the experimental momentum distribution of the $1p_{1/2}$ hole state obtained from knock-out coincidence experiments performed at much higher values of the nuclear excitation energy[18)] (E ~ 150 MeV).

The interesting feature of Figs. 23 and 24 consists in the fact that the angular distributions calculated with (full lines) and without (dashed lines) particle-hole interaction have a rather similar shape and they differ only in the magnitude. This remark can lead to the conclusion that in this region all the multipole modes are excited with approximately the same strength, and the only effect of the residual interaction is on the overall magnitude of the cross section.

To investigate quantitatively this question we compared the values obtained integrating the coincidence cross section, calculated with and without residual p-h interaction, over the angle ϑ_p of the emitted particle.

In Fig. 25 we show, for two different values of the energy of the incoming electron, ε_i = 100 MeV and ε_i = 180 MeV, the dependence of the integrated coincidence cross sections from the nuclear excitation energies. In Fig. 25 the full lines represent the results of the calculations performed including the residual interaction and the dashed lines have been computed without residual interaction.

The first remark which arises from the analysis of Fig. 25 is that the particle-hole interaction shifts strengths from the high energy region into the giant resonance region, as it has been already pointed out by Balashov[62)]. The difference between the calculations performed with and without residual interaction is more pronounced in Fig. 25b where higher values of the momentum transfer are probed. This is probably a consequence of the fact that we are using a zero range p-h interaction. In effect, more realistic nucleon-nucleon interactions[51)], based on the one-boson exchange picture, decrease for high values of the transferred momentum. In Fig. 25b the effects of the p-h interaction are probably overestimated since under the kinematic conditions involved ($q \sim 1.2\ fm^{-1}$) the long range terms of the residual interaction start to become important. The percentage of the charge term contribution to the integrated cross section of Fig. 25 is given in Table 6.

For both energies of the incoming electron, ε_i = 100 MeV and ε_i = 180 MeV, the calculations performed using the p-h interaction show that the importance of the charge term decreases with the increasing of the energy. In the giant resonance region the charge term is responsible for about 90 % of the integrated coincidence cross section, while at the excitation energy E = 40MeV the contribution of the charge term amounts to 82.8 % and 76.5 % respectively for ε_i = 100 MeV and ε_i = 180 MeV.

One has to remark that, since the charge-current interference term is mirror antisymmetric, $I(\vartheta_p) = -I(-\vartheta_p)$, as discussed in section c) of this chapter, its contribution to the integrated cross section is exactly zero. It is interesting to note that, in Table 6, the results of the calculations performed without residual interaction present the same behaviour with respect to the calculations performed using the p-h interaction. In both cases, for ε_i = 100 MeV and ε_i = 180 MeV, the charge term contribution is underestimated in the giant resonance region and overestimated at the excitation energy E = 40 MeV. This result seems to indicate that, in the giant resonance region, collective degrees of freedom are enhancing the role of the nuclear excitation mechanisms connected with the charge operator, while with the increasing of the energy the situation changes and the collectivity of the nuclear excitation results to be contained in the excitation terms generated by the nuclear current.

CHAPTER 5

Application to ^{12}C

The nucleus ^{12}C is not one of the ideal cases to investigate with nuclear models like RPA based on a spherical approximation of the nucleus. Deformation effects are known to be important in the description of the ground state of this nucleus[43)]. In spite of this, the possibility to compare the results of our calculations directly with experimental data[25)], the only data of this kind available up to now, makes the application of our model to the description of the decay of ^{12}C worth-while.

In Fig. 26 the photoabsorption cross section for the dipole resonance is compared with the experimental data of Ahrens et al.[48)] as a check of our model. The peak of the theoretical dipole strength is found 1.5 MeV below the experimental peak at 22.5 MeV. As expected in a 1p-1h approximation, the magnitude of the cross section is overestimated roughly by a factor two, while the width is underestimated. Explicit inclusion of 2p-2h effects is expected to improve the agreement with the experimental data[49)]. Since the dominant features of the dipole strength are reproduced, we feel encouraged to apply our model to the (e,e'p) data of Calarco et al.[25)].

The comparison between the result of our calculations and the data of Calarco is shown in Fig. 27. Note that all the theoretical energies are shifted up by 1.5 MeV in order to compensate for the discrepancy between the experimental and the theoretical peak of the photoabsorption cross section. Since the theoretical angular distributions overshoot the experimental data, and at present we are interested in the shape of the angular distribution of the emitted particle, we determined a scaling factor of $\lambda = 0.4$ in order to facilitate the comparison between the theoretical and experimental angular distribution at the peak energy of 22.47 MeV of the dipole resonance. At all the other excitation energies, the comparison was made using the same scaling factor.

The first result obtained is that the model is able to reproduce the relative magnitudes of the coincidence cross sections at all experimentally investigated excitation energies. The scaling factor effectively takes into account effects of 2p-2h configurations and branching to decay modes other than proton or neutron emission.

In Fig. 27 the solid lines include all multipolarities of both positive and negative parity up to J=4, larger multipolarities were found to be negligible.

The shape of the experimental angular distribution at the peak of the giant dipole resonance (22.47 MeV) is essentially preserved at 21.65 MeV and 22.98 MeV; this confirms the dominant influence of this excitation mode in the energy interval considered, as expected from the photoabsorption cross section. In the present version of the model, the width of the dipole resonance is underestimated, and consequently, the dipole-like decay pattern is only qualitatively reproduced at 22.98 MeV and not at all at 21.65 MeV. Clearly the inclusion of 2p-2h effects into continuum calculations would improve this situation.

On the other hand, at low energies, not only the relative magnitudes but also the shapes of the cross sections are very well reproduced. The strong forward-backward asymmetry striking in the angular distribution at E = 19.28, 19.92 and 20.63 MeV is a clear signature of the presence of positive parity strength interfering with the tail of the giant dipole resonance.

Calarco et al.[25] suggested that in addition to the 2^+ strength (found in $(\alpha\alpha')$[9]), also 0^+ strength might be present at 20.63 MeV. In order to demonstrate the effects of 0^+ strength, we repeated the calculation without monopole strength (dashed line). A surprisingly large influence of the 0^+ strength is found: without monopole strength a series of bumps in both forward and backward direction is found between 19.28 and 20.63 MeV, while only the inclusion of the monopole is able to reproduce the large experimental bumps in backward direction.

The large effect of the monopole strength at 20.63 MeV does not imply that the monopole is a concentrated resonance. The omission of monopole strength continues to have a large effect on the relative magnitude of the cross section up to 22.98 MeV, even though there are no obvious effects on the shape of the cross section.

In Fig. 28 the exhaustion of the energy weighted sum rule is shown for the monopole, the dipole and the quadrupole strength. The sum rule exhaustion has been calculated using the classical energy weighted sum rule

$$\int dE\, E\, \sigma_\gamma^J(E) = 4\pi^2 \frac{e^2}{\hbar c} \sum_f E_f \left| \langle f | Q_{JM} | 0 \rangle \right|^2 \tag{54}$$

where σ_γ^J is the photoabsorption cross section for a nuclear excitation to a state $|f\rangle$ with angular momentum J, and Q_J is the electric multipole operator. Using the long wave approximation the multipole operator is expressed as:

$$Q_{JM} = \sum_i r_i^J\, Y_{JM}(\hat{r}_i)\, \tfrac{1}{2}(1-\tau_3(i)) \tag{55}$$

Then, supposing that the potential term of the nuclear Hamiltonian commutes with Q_{JM}, one obtains:

$$\sum_f E_f \left|\langle f|Q_{JM}|0\rangle\right|^2 = \frac{\hbar^2}{2m}\frac{J(2J+1)^2}{4\pi}\sum_i \langle i|r^{2J-2}|i\rangle \tag{56}$$

where with $|i\rangle$ we indicate the single particle states of the nuclear ground state. Since the Landau-Migdal interaction we used as p-h interaction contains isospin dependent terms, the potential part of the nuclear Hamiltonian does not commute with the operator Q_{JM}. For this reason in Fig. 28 the curves representing the sum rule exhaustion of 1^- and 2^+ are overshooting the 100 % of the sum rule value calculated with eq. (56). In Fig. 28 the full curve of the 0^+ remains below the 100 % of the sum rule value since the monopole excitation is practically only isoscalar, i.e. it is not sensitive to the isospin dependent terms of the Landau-Migdal interaction.

While the dipole strength is exhausted within an energy interval of approximately 10 MeV, a very broad monopole strength distribution is found which needs an energy interval of at least 20 MeV to exhaust its sum rule. A large width of the monopole strength is due to the fact that the monopole mode is predominantly given by the excitation of the $p_{3/2}$ hole to the $p_{3/2}$ partial wave, which does not show any resonant behaviour in ^{12}C. Nevertheless, in the energy region between 19 and 20.5 MeV, the monopole strength and the dipole strength are comparable, which causes large interference effects. Beyond 20.5 MeV, the dipole strength is much larger than the monopole strength, and therefore, the interference effects are overwhelmed by the huge dipole resonance. The quadrupole strength extends between 20 and 50 MeV. The quadrupole strength in ^{12}C is mainly formed by a coupling of the $p_{3/2}$ hole with the $f_{7/2}$ partial wave which exhibits no resonance. This agrees qualitatively with the experimental results obtained in α-scattering[9] and elastic photon scattering[63].

The present model appears to leave relatively small probabilities for decay modes other than nucleon decay. Since the presence of 2p-2h configurations in a discretized calculation[49] reduces the dipole strength by a factor 0.5, while a factor λ = 0.4 was necessary to reproduce the magnitude of all (e,e'p) cross sections between 19.28 and 22.98 MeV, a rough estimate for the branching ratio to nucleon decay channel is 90 %. Indeed, Calarco et al.[25] found a branching ratio to α-particles of less than 10 %. In the analysis of α-induced decay of ^{12}C, mainly α-particles were emitted[8]. Since the α-particle does not excite the isovector dipole resonance, a possible explanation is that the dipole mainly decays via nucleon emission, while only the quadrupole resonance decays predominantly via α-emission.

As a last remark we would like to point out that the data of Calarco et al. were taken at $q = 0.4\ fm^{-1}$ while, within our model, the maximum response for the monopole excitation is found at $q = 0.75\ fm^{-1}$.

CONCLUSIONS

In this work we developed a model describing the nucleon emission induced by electro-scattering processes in terms of multipole excitation of the nucleus. In the present version of the model these nuclear modes are treated within the 1p-1h continuum RPA framework.

Our model is particularly suitable to describe coincidence knock-out processes (e,e'N) in the energy region of the giant resonances, but it can be used also in the quasi-free scattering region. In contrast to the work of Balashov[62,64,65] all the four terms of the coincidence cross section, eq. (20), were taken into account in the calculations, which is necessary in order to have a realistic description of the angular distributions of the emitted particles.

Studying the electro-excitation of ^{16}O it was found that, in the giant resonance region, the interference term between the two transverse components of the current density, J_+ and J_-, gives a negligible contribution to the cross section. The charge-current interference, however, is usually fairly large and has to be included in order to understand the breaking of the reflection symmetry around the axis defined by the momentum transfer.

The model has been extensively applied to the description of the decay of the electro-excited ^{16}O and it has been used to analyse the (e,e'p) experimental data of Calarco et al.[25] in ^{12}C.

Our results show that electron scattering coincidence experiments are a suitable tool to investigate weak multipole excitation modes. The interference between modes of different multipolarity enhances the presence of weak modes which, in the one-arm experiments, are hidden in the background.

The angular distribution presented by Calarco's data in ^{12}C exhibits clear effects due to the presence of monopole strength, even though the solution of the continuum RPA equations does not show presence of an energetically concentrated monopole resonance. In this context our model has been used to show that the presence of monopole strength can be identified in ^{16}O most clearly in the excitation energy region around 20 MeV, since here it can interfere with the beginning tail of the dipole resonance. Even though the angular distribution of the emitted particle is extremely sensitive to the presence of weak multipole modes, no evident signature of electric octupole excitation was found in ^{16}O.

Another feature of the electron scattering coincidence processes, which has been pointed out by our calculation, is the high selectivity of the (e,e'p) reaction in exciting sharp states embedded in the continuum. We showed, for example, that in ^{16}O the 4^- state emerges very clearly only when the proton coming from the $p_{3/2}$ bound level is detected.

Within the present model, in ^{16}O, for energies above the giant resonance region the quasi-free knock-out process starts to take place. In this energy region the major effect of the channel-to-channel coupling consists in an overall reduction of the cross section, while the shape of the angular distribution, which favours particle emission in the direction of the momentum transfer, does not differ from the one obtained without channel-to-channel coupling.

A comparison between the results of our model and of the quasi-free approach with the experimental data available in the quasi-elastic region could be used to investigate the microscopic origin of the optical potential used in the quasi-free approach. Specifically it would be interesting to know up to which extent the channel-to-channel coupling included in our model is able to explain the asymmetry in the angular distribution of the reduced cross section found in the (e,e'p) experiments of Saclay[18)]. So far this asymmetry has been explained in the quasi-free approach with the presence of an imaginary term in the spin-orbit part of the nuclear central potential which is at least partly contained in the present coupled-channel approach. This kind of investigations requires the use of a more reliable p-h interaction which takes into account the finite-range terms of the nucleon-nucleon interaction.

From the discussion of the results we have presented it appears clear that the strongest approximation of our model consists in restricting the description of the nuclear excited states to a superposition of 1p-1h configurations. The approximations made to describe the electron-nucleus interaction (one-photon exchange, plane wave Born approximation, electromagnetic operators not including sub-nucleonic degrees of freedom, etc.) are orders of magnitude smaller. For a more accurate analysis of the experimental data, the evaluation of the spreading width generated by the 2p-2h degrees of freedom becomes fundamental.

APPENDIX A

In this Appendix we briefly sketch the method used to solve the continuum RPA equations. We work with a set of single particle wave functions defined as

$$|\vec{r}\varepsilon;\ell\,{}^1\!/_2\;\;j;m\rangle = R_{j\ell}(r,\varepsilon)\sum_{\mu\sigma}\langle\ell\mu\,{}^1\!/_2\,\sigma|jm\rangle\,Y_{\ell\mu}(\hat{r})\chi_\sigma^{1/2} \tag{A1}$$

and in the following we shall indicate with j the angular part of the wave function. The matrix elements of eq. (26) we have to solve are defined as:

$$v^J_{ph,p'h'}(\varepsilon,\varepsilon') = \sum_K (-)^{J+j_h+j_{p'}}(2K+1)\begin{Bmatrix} j_p & j_h & J \\ j_{p'} & j_{h'} & K \end{Bmatrix} \tag{A2}$$

$$[\langle j_p(\varepsilon)j_{h'}K|V_{ph}|j_hj_{p'}(\varepsilon')K\rangle - (-)^{j_{p'}+j_h-J}\langle j_{p'}(\varepsilon')j_h|V_{ph}|j_p(\varepsilon)j_{h'}\rangle]$$

$$u^J_{ph,p'h'}(\varepsilon,\varepsilon') = (-)^{j_{h'}-j_{p'}-J}\;v^J_{ph,h'p'}(\varepsilon,\varepsilon') \tag{A3}$$

where $|j_pj_hK\rangle$ is the product of the two single particle wave functions coupled to the angular momentum K. Using the zero range Landau-Migdal particle-hole interaction (37) to compute the matrix elements (A2)-(A3) one arrives to express eq. (26) as:

$$B_{c_0,c\equiv(p,h)}(E,J,\pi;\varepsilon) + \sum_{c'}^{\text{cont}} v^J_{c,c'}(\varepsilon,\varepsilon')A_{c_0,c'}\;\delta(\varepsilon'-\varepsilon_{h'}-E)$$

$$+ F\int dr\; R_p(r,\varepsilon)R_h(r)\langle j_p\|Y_J\|j_h\rangle\cdot\rho_{c_0}(E,J,\pi;r)$$

$$+ G\sum_\ell\int dr\; R_p(r,\varepsilon)R_h(r)\langle j_p\|[Y_\ell\otimes\vec{\sigma}]_J\|j_h\rangle\sigma_{c_0}(E,J,\pi,\ell;r) = 0 \tag{A4}$$

$$C_{c_o,c\equiv(p,h)}(E,J,\pi;\varepsilon) + \sum_{c'}^{\text{cont}} u^{*J}_{c,c'}(\varepsilon,\varepsilon')A_{c_o,c'}\ \delta(\varepsilon'-\varepsilon_{h'}-E)$$

$$+ (-)^J\ F \int drr^2 R_p(r,\varepsilon)R_h(r)\langle j_p \| Y_J \| j_h\rangle \rho_{c_o}(E,J,\pi;r)$$

$$+ G \sum_{\ell} (-)^{\ell+1} \int drr^2 R_p(r,\varepsilon)R_h(r)\langle j_p \| [Y_\ell \otimes \vec{\sigma}]_J \| j_h\rangle \sigma_{c_o}(E,J,\pi,\ell;r)$$

where we have defined a scalar transition density ρ_c and a spin transition density σ_c as follows:

$$\rho_{c_o}(E,J,\pi;r) \equiv \sum_{ph} \frac{\langle j_p \| Y_J \| j_h\rangle}{[J]^2} \int d\varepsilon\ R_p(r,\varepsilon)R_h(r)$$

$$\left[\frac{B_{c_o,c}(E,J,\pi;\varepsilon)}{\varepsilon-\varepsilon_h-E} + (-)^J \frac{C_{c_o,c}(E,J,\pi;\varepsilon)}{\varepsilon-\varepsilon_h+E}\right]$$

$$\sigma_{c_o}(E,J,\pi,\ell;r) \equiv \sum_{ph} \frac{\langle j_p \| [Y_\ell \otimes \vec{\sigma}]_J \| j_h\rangle}{[J]^2} \int d\varepsilon\ R_p(r,\varepsilon)R_h(r) \tag{A5}$$

$$\left[\frac{B_{c_o,c}(E,J,\pi;\varepsilon)}{\varepsilon-\varepsilon_h-E} + (-)^{\ell+1} \frac{C_{c_o,c}(E,J,\pi;\varepsilon)}{\varepsilon-\varepsilon_h+E}\right]$$

For simplicity, in eq. (A4) we consider only the F and G coefficients. The additional isospin dependence of F' and G' can be included easily.

Inserting eqs. (A4) in (A5) one obtains

$$\rho_c(E,J,\pi;r) = -F\int dr_1 r_1^2 G^{J,E}(r,r_1)\rho_c(E,J,\pi;r_1)$$

$$- G\sum_{\ell}\int dr_1 r_1^2 H_{\ell}^{J,E}(r,r_1)\sigma_c(E,J,\pi,\ell;r_1) - Q_c(J;r)$$

$$\sigma_c(E,J,\pi,\ell;r) = -F\int dr_1 r_1^2 H_{\ell}^{J,E}(r_1,r)\rho_c(E,J,\pi;r_1) \tag{A6}$$

$$- G\sum_{\ell'}\int dr_1 r_1^2 U_{\ell,\ell'}^{J,E}(r,r_1)\sigma_c(E,J,\pi,\ell';r_1) - W_c(J,\ell;r)$$

where we used the definitions:

$$G^{J,E}(r,r_1) \equiv \sum_{ph}\left[⨍ d\varepsilon \frac{D_{ph}^{J}(\varepsilon,r)D_{ph}^{J}(\varepsilon,r_1)}{\varepsilon-\varepsilon_h-E} + \int d\varepsilon \frac{D_{ph}^{J}(\varepsilon,r)D_{ph}^{J}(\varepsilon,r_1)}{\varepsilon-\varepsilon_h+E}\right] \tag{A7}$$

$$H_{\ell}^{J,E}(r,r_1) \equiv \sum_{ph}\left[⨍ d\varepsilon \frac{D_{ph}^{J}(\varepsilon,r)F_{ph}^{J,\ell}(\varepsilon,r_1)}{\varepsilon-\varepsilon_h-E} + (-)^{J+\ell+1}\int d\varepsilon \frac{D_{ph}^{J}(\varepsilon,r)F_{ph}^{J,\ell}(\varepsilon,r_1)}{\varepsilon-\varepsilon_h+E}\right]$$

$$U_{\ell,\ell'}^{J,E}(r,r_1) \equiv \sum_{ph}\left[⨍ d\varepsilon \frac{F_{ph}^{J,\ell}(\varepsilon,r)F_{ph}^{J,\ell'}(\varepsilon,r_1)}{\varepsilon-\varepsilon_h-E} + (-)^{\ell+\ell'}\int d\varepsilon \frac{F_{ph}^{J,\ell}(\varepsilon,r)F_{ph}^{J,\ell'}(\varepsilon,r_1)}{\varepsilon-\varepsilon_h+E}\right]$$

with

$$D_{ph}^{J}(\varepsilon,r) \equiv \frac{R_p(r,\varepsilon)R_h(r)}{[J]}\langle j_p \| Y_J \| j_h\rangle$$

$$F_{ph}^{J,\ell}(\varepsilon,r) \equiv \frac{R_p(r,\varepsilon)R_h(r)}{[J]}\langle j_p \| [Y_{\ell}\otimes\vec{\sigma}]_J \| j_h\rangle \tag{A8}$$

The two terms W and Q of eq. (A6) are the known terms containing A_{ph} and they are defined as:

$$Q_c(J,r) \equiv \sum_{c=(ph)} \frac{\langle j_p \| Y_J \| j_h \rangle}{[J]^2} \int d\varepsilon\, R_p(r,\varepsilon) R_h(r)$$

$$\sum_{p'h'} \left[\left(\frac{v^J_{c,c'}}{\varepsilon-\varepsilon_{p'}-E} + (-)^J \frac{u^J_{c,c'}}{\varepsilon-\varepsilon_{h'}+E}\right) A_{c',c}\ \delta(\varepsilon'-\varepsilon_{h'}-E)\right]$$

$$W_c(J,\ell,r) \equiv \sum_{c=(ph)} \frac{\langle j_p \| [Y_\ell \otimes \vec{\sigma}]_J \| j_h \rangle}{[J]^2} \int d\varepsilon\, R_p(r,\varepsilon) R_h(r) \tag{A9}$$

$$\sum_{p'h'} \left[\left(\frac{v^{*J}_{c,c'}}{\varepsilon-\varepsilon_{p'}-E} + (-)^{\ell+1} \frac{u^{*J}_{c,c'}}{\varepsilon-\varepsilon_{h'}+E}\right) A_{c',c}\ \delta(\varepsilon'-\varepsilon_{h'}-E)\right]$$

Since the ρ and σ terms defined in (A6) contain the information about the B coefficients of eq. (A5) we solve directly eqs. (A6) by expanding in Fourier-Bessel series[46].

We make the following expansions:

$$\rho_c(E,J,\pi;r) = \sum_{\mu=1}^{M} \rho^c_\mu\, j_J(q_\mu r)$$

$$\sigma_c(E,J,\pi,\ell;r) = \sum_{\mu=1}^{M} \sigma^{c,\ell}_\mu\, j_J(q_\mu r)$$

$$D^J_{ph}(\varepsilon,r) = \sum_{\mu=1}^{M} D^{ph,J}_\mu(\varepsilon)\, j_J(q_\mu r)$$

$$F^{J,\ell}_{ph}(\varepsilon,r) = \sum_{\mu=1}^{M} F^{ph,J,\ell}_\mu(\varepsilon)\, j_J(q_\mu r)$$

$$G^J(r,r_1) = \sum_{\mu\nu}^{M} G^J_{\mu\nu}\, j_J(q_\mu r)\, j_J(q_\nu r_1)$$

$$H^J_\ell(r,r_1) = \sum_{\mu\nu}^{M} H^{J,\ell}_{\mu\nu}\, j_J(q_\mu r)\, j_J(q_\nu r_1) \tag{A10}$$

$$U^J_{\ell,\ell'}(r,r_1) = \sum_{\mu\nu}^{M} U^{J,\ell,\ell'}_{\mu\nu} \; j_J(q_\mu r) \; j_J(q_\nu r_1)$$

$$Q_c(J;r) = \sum_{\mu=1}^{M} Q^c_\mu \, j_J(q_\mu r)$$

$$W_c(J,\ell;r) = \sum_{\mu=1}^{M} W^{c,\ell}_\mu \, j_J(q_\mu r)$$

where M is the number of the expansion coefficients.

Now defining two new quantities

$$T_{\eta\mu} = \int drr^2 \; j_J(q_\eta r) \; F \; j_J(q_\mu r)$$

$$S_{\eta\mu} = \int drr^2 \; j_J(q_\eta r) \; G \; J_J(q_\mu r) \tag{A11}$$

and inserting (A10) in (A6) one obtains:

$$\rho^c_\nu = - \sum_{\mu\eta}^{M} (G^J_{\nu,\eta} \; T_{\eta,\mu} \; \rho^c_\mu + \sum_\ell H^{J,\ell}_{\nu,\eta} \; S_{\eta,\mu} \; \sigma^{c,\ell}_\mu) - Q^c_\nu$$

$$\sigma^{c,\ell}_\nu = - \sum_{\mu\eta}^{M} (H^{J,\ell}_{\nu,\eta} \; T_{\eta,\mu} \; \rho^c_\mu + \sum_{\ell'} U^{J,\ell,\ell'}_{\nu,\eta} \; S_{\eta,\mu} \; \sigma^{c,\ell}_\mu) - W^{c,\ell}_\nu \tag{A12}$$

Specializing eqs. (A12) for protons (p) and neutrons (n) and considering that for natural parity states ℓ=J we write in matrix form:

$$\begin{bmatrix} (G^p\ T^{pp}+1) & G^p\ T^{pn} & H^{p,J}\ S^{pp} & H^{p,J}\ S^{pn} \\ G^n\ T^{np} & (G^n\ T^{nn}+1) & H^{n,J}\ S^{np} & H^{n,J}\ S^{nn} \\ H^{p,J}\ T^{pp} & H^{p,J}\ T^{pn} & (U^{p,J,J}\ S^{pp}+1) & U^{p,J,J}\ S^{pn} \\ H^{n,J}\ T^{np} & H^{n,J}\ T^{nn} & U^{n,J,J}\ S^{np} & (U^{n,J,J}\ S^{nn}+1) \end{bmatrix} \begin{bmatrix} \rho^{c,p} \\ \rho^{c,n} \\ \sigma^{c,J,p} \\ \sigma^{c,J,n} \end{bmatrix} = \begin{bmatrix} Q^{c,p} \\ Q^{c,n} \\ W^{c,J,p} \\ W^{c,J,n} \end{bmatrix} \qquad \text{(A13)}$$

where writing G^τ $H^{\tau,J}$ $U^{\tau,JJ}$ we dropped a common index J.

For unnatural parity states $C_\mu=0$ and $\ell=J\pm1$ then the system of equations to solve is:

$$\begin{bmatrix} (U^{p,J+1,J+1}S^{pp}+1) & U^{p,J+1,J+1}S^{pn} & U^{p,J+1,J-1}S^{pp} & U^{p,J+1,J-1}S^{pn} \\ U^{n,J+1,J+1}S^{np} & (U^{n,J+1,J+1}S^{nn}+1) & U^{n,J+1,J-1}S^{np} & U^{n,J+1,J-1}S^{nn} \\ U^{p,J-1,J+1}S^{pp} & U^{p,J-1,J+1}S^{pp} & (U^{p,J-1,J-1}S^{pp}+1) & U^{p,J-1,J-1}S^{pn} \\ U^{n,J-1,J-1}S^{np} & U^{n,J-1,J+1}S^{nn} & U^{n,J-1,J-1}S^{np} & (U^{n,J-1,J-1}S^{nn}+1) \end{bmatrix} \begin{bmatrix} \sigma^{c,J+1,p} \\ \sigma^{c,J+1,n} \\ \sigma^{c,J-1,p} \\ \sigma^{c,J-1,n} \end{bmatrix} = \begin{bmatrix} W^{c,J+1,p} \\ W^{c,J+1,n} \\ W^{c,J-1,p} \\ W^{c,J-1,n} \end{bmatrix}$$

(A14)

To obtain the B and C coefficients of eq. (A5) from the solutions of (A13) and (A14) one has to calculate:

$$B^\tau_{c,c'}(\varepsilon') = -\sum_{\tau'}\sum_{\mu\nu}\left[D^{c',J}_{\mu(\varepsilon')}\ T^{\tau\tau'}_{\mu\nu}\ \rho^{c,\tau'}_\nu + F^{c',J,J}_\mu(\varepsilon')\ S^{\tau\tau'}_{\mu\nu}\ \sigma^{c,J,\tau'}_\nu\right]$$

(A15)

$$C^\tau_{c,c'}(\varepsilon') = -\sum_{\tau'}\sum_{\mu\nu}\left[(-)^J D^{c',J}_\mu(\varepsilon')\ T^{\tau\tau'}_{\mu\nu}\ \rho^{c,\tau'}_\nu + (-)^{J+1}\ F^{c',J,J}_\mu(\varepsilon)\ S^{\tau\tau'}_{\mu\nu}\ \sigma^{c,J,\tau'}_\nu.\right]$$

for natural parity states and

$$B^{\tau}_{c,c'}(\varepsilon') = - \sum_{\tau'} \sum_{\mu\nu} [F_{\mu}^{c',J,J+1}(\varepsilon')\ S^{\tau\tau'}_{\mu\nu}\ \sigma_{\nu}^{c,J+1,\tau'} + F_{\mu}^{c',J,J-1}(\varepsilon')\ S^{\tau\tau'}_{\mu\nu}\ \sigma_{\nu}^{c,J-1,\tau'}]$$

$$C^{\tau}_{c,c'}(\varepsilon') = - \sum_{\tau'} \sum_{\mu\nu} [(-)^{J} F_{\mu}^{c',J,J+1}(\varepsilon')\ S^{\tau\tau'}_{\mu\nu}\ \sigma_{\nu}^{c,J+1,\tau'} \tag{A16}$$

$$+ (-)^{J} F_{\mu}^{c',J,J-1}(\varepsilon')\ S^{\tau\tau'}_{\mu\nu}\ \sigma_{\nu}^{c,J-1,\tau'}]$$

for unnatural parity states, where the index τ runs over protons and neutrons.

APPENDIX B

In this Appendix, we give the expressions for the single particle transition matrix elements of eq. (34). The basis of the single particle states has been defined in (A1) and we shall use the notation:

$$|jm\rangle \equiv |r\varepsilon;\ell\,\tfrac{1}{2}\,j;m\rangle \tag{B1}$$

We assume that the electromagnetic operators are local and that the electromagnetic field interacts with one nucleon at once. The charge operator is defined as

$$\rho(\vec{r}) = \tfrac{1}{2}\,[1+\tau_3(i)]\,\delta(\vec{r}-\vec{r}_i) \tag{B2}$$

where τ_3=1 for protons and $\tau_3(i)$=-1 for neutrons.

The current operator is defined as sum of convection and magnetization current:

$$J(\vec{r}) = j_c(\vec{r}) + \vec{\nabla}x\mu(\vec{r}) \tag{B3}$$

where

$$j_c(\vec{r}) = \frac{1}{i2m}\,[\vec{\nabla}_j-\vec{\nabla}_j]\,\delta(\vec{r}-\vec{r}_j)\,\tfrac{1}{2}\,[1+\tau_3(j)] \tag{B4}$$

and

$$\mu(\vec{r}) = [\frac{\mu_p+\mu_n}{2} + \frac{\mu_p-\mu_n}{2}\,\tau_3(i)]\,\frac{1}{2m}\,\vec{\sigma}\,\delta(\vec{r}-\vec{r}_i) \tag{B5}$$

with m the nucleon mass and $\mu_p = 2.79$, $\mu_n = -1.91$. We give here the expression of the reduced single particle matrix elements of the W_0 and S operators defined in eqs. (13) and (15):

$$\frac{1}{2}\langle j_p \| W_0(q) \| j_h\rangle = (-)^{j_p+1/2} \frac{[j_p][j_h][J]}{\sqrt{4\pi}} \begin{pmatrix} j_p & J & j_h \\ 1/2 & 0 & -1/2 \end{pmatrix}$$

$$\int drr^2\, j_J(qr) R_p(r) R_h(r)\, 1/2\, [1+(-)^{\ell_p+\ell_h+J}] \tag{B6}$$

$$\langle j_p \| S_{J,J+1}(q) \| j_h\rangle = \frac{1}{i2m} (-)^{j_h+1/2+J} \frac{[j_p][j_h]}{\sqrt{4\pi}}$$

$$\begin{pmatrix} j_p & j_h & J \\ 1/2 & -1/2 & 0 \end{pmatrix} 1/2\, [1+(-)^{\ell_p+\ell_h+J}]$$

$$\cdot \left\{ \sqrt{J+1} \int drr^2 j_{J+1}(qr) [R_p(r) \frac{\partial}{\partial r} R_h(r) - R_h(r) \frac{\partial}{\partial r} R_p(r)] \right. \tag{B7}$$

$$\left. + \frac{(x_p-x_h)(1+x_p+x_h)}{\sqrt{J+1}} \int drr^2 \frac{R_p(r)R_h(r)}{r} j_{J+1}(qr) \right\}$$

$$+ iq \frac{\mu_i}{2m} (-)^{\ell_p} \frac{[j_p][j_h]}{\sqrt{4\pi}} \sqrt{J} \begin{pmatrix} j_p & j_h & J \\ 1/2 & 1/2 & -1 \end{pmatrix} \int drr^2 j_J(qr) R_p(r) R_h(r)\, 1/2\, [1+(-)^{\ell_p+\ell_h+J}]$$

$$\langle j_p \| S_{J,J}(q) \| j_h\rangle = \frac{1}{i2m} (-)^{j_h+1/2+J} \frac{[j_h][j_p][J]}{\sqrt{4\pi}} \begin{pmatrix} j_p & j_h & J \\ 1/2 & -1/2 & 0 \end{pmatrix} 1/2\, [1+(-)^{\ell_p+\ell_h+J+1}]$$

$$\frac{(x_p+x_h)(x_p+x_h+1)-J(J+1)}{\sqrt{J(J+1)}} \int drr^2 j_J(qr) \frac{R_p(r)R_h(r)}{r}$$

$$+ \; iq \frac{\mu_i}{2m} \frac{(-)^{j_p+1/2}}{\sqrt{4\pi}} \frac{[j_p][j_n]}{[J]} \begin{pmatrix} j_p & j_h & J \\ -1/2 & 1/2 & 0 \end{pmatrix} 1/2 \, [1+(-)^{\ell_p+\ell_h+J+1}]$$

$$[(\frac{J+1}{J})^{1/2} (\chi_p+\chi_h-J) \int drr^2 j_{J-1}(qr) R_p(r) R_h(r)$$

$$- (\frac{J}{J+1})^{1/2} (\chi_p+\chi_h+J+1) \int drr^2 j_{J+1}(qr) R_p(r) R_h(r)]$$

$$\langle j_p \| S_{J,J-1}(q) \| j_h \rangle = \frac{1}{i2m} (-)^{J+j_h+1/2} \frac{[j_p][j_h]}{\sqrt{4\pi}}$$

$$\begin{pmatrix} j_h & j_p & J \\ 1/2 & -1/2 & 0 \end{pmatrix} 1/2 \, [1+(-)^{\ell_p+\ell_h+J}]$$

$$\Bigg\{ \frac{(\chi_p-\chi_h)(\chi_p+\chi_h+1)}{\sqrt{J}} \int drr^2 j_{J-1}(qr) \frac{R_p(r)R_h(r)}{r}$$

$$- \sqrt{J} \int drr^2 j_{J-1}(qr) [R_p(r) \frac{\partial}{\partial r} R_h(r) - R_h(r) \frac{\partial}{\partial r} R_p(r)] \Bigg\}$$

$$- \; iq \frac{\mu_i}{2m} (-)^{\ell_p} \frac{[j_p][j_h]}{\sqrt{4\pi}} \sqrt{J+1} \begin{pmatrix} j_p & j_h & J \\ 1/2 & 1/2 & -1 \end{pmatrix} 1/2 \, [1+(-)^{\ell_p+\ell_h+J}]$$

$$\int drr^2 j_J(qr) R_p(r) R_h(r)$$

where $\chi = (-)^{\ell+j+1/2} (j+1/2)$.

ACKNOWLEDGMENTS

I would like to express my gratitude to Prof. J. Speth for the suggestion of the subject and for his encouragement during the development of the work.

I wish to give my wider thanks to Siggi Krewald not only for his invaluable contribution to this work, for the daily help, advice and teaching, for having shared with me enthusiasm and disillusions in all the phases of the work, but also for his friendship.

A special thank to Ewald Brökel for his continuous, careful and paternal assistance in the computing work and for his help in drawing the more complicated figures.

Thanks to Madda Heese who transformed, with an incredible speed and efficiency, a long and complicated manuscript into an accurate typescript.

I would like to thank also Bernd Hoffmann who wrote, and modified following my needs, the plotting routine used to draw the main part of the figures.

I am grateful to all my colleagues of the theory group who, discussing, advising and teaching me, created a friendly and stimulating environment.

A particular thank to Raphael de Haro Jr. for the illuminating discussions about the Fourier-Bessel approach to the continuum RPA and for having explained to me how to use his continuum RPA code.

For the permission of quoting their unpublished data I would like to thank Prof. J. Ahrens and Prof. J. Calarco.

Thanks to Prof. G.J. Wagner for the profitable discussion about some experimental aspects of coincidence experiments and to Prof. Boffi for having clarified a point of his work I misunderstood.

Finally I would like to thank the Kernforschungsanlage Jülich for the financial support.

REFERENCES

1) K. Goeke, J. Speth, Ann. Rev. Nucl. Part. Sci. 32 (1982) 65.

2) A.B. Migdal, Nucl. Phys. 57 (1964) 29.

3) J.P. Blaizot, Phys. Rep. C64 (1980) 171.

4) R.R. Doering, A. Galonsky, D.M. Patterson, G.F. Bertsch, Phys. Rev. Lett. 35 (1975) 1691;
C.D. Goodman et al., Phys. Rev. Lett. 44 (1980) 1755;
D.E. Bainum et al., Phys. Rev. Lett. 44 (1980) 1751.

5) J. Speth, A. van der Woude, Rep. Prog. Phys. 44 (1981) 719.

6) A. Moalem, W. Benenson, G.M. Crawley, T.L. Khoo, Phys. Lett. 61B (1976) 167.

7) D.H. Youngblood, A.D. Bacher, D.R. Brown, J.D. Bronson, J.M. Moss, C.M. Rozsa, Phys. Rev. C15 (1977) 246.

8) K.T. Knöpfle, G.J. Wagner, P. Paul, H. Breuer, C. Mayer-Böricke, M. Rogge, P. Turek, Phys. Lett. 74B (1978) 191.

9) H. Riedesel, K.T. Knöpfle, H. Breuer, P. Doll, G. Mairle, G.J. Wagner, Phys. Rev. Lett. 41 (1978) 377.

10) G.J. Wagner, Lecture Notes in Physics 92 (1979) 269;
L.S. Cardman, Nucl. Phys. A354 (1981) 173c;
G.J. Wagner, in: Giant Multipole Resonances, ed. F. Bertrand, Harwood Academic Publ. (1980), p. 251.

11) A. Faessler, D.J. Millener, P. Paul, D. Strottman, Nucl. Phys. A330 (1979) 333.

12) W.G. Love, M.A. Franey, Phys. Rev. C24 (1981) 1073;
COSY-Studie, Jül-Spez-242 (1984).

13) H. Hermingaus, A. Feder, K.H. Kaiser, W. Manz, H.v.d. Schmitt, Nucl. Instr. and Meth. 138 (1976) 1.

14) Proc. Int. Conf. on Nuclear Physics with Electromagnetic Interactions, Mainz (1979), eds. H. Arenhövel and D. Drechsel, Lecture Notes in Physics 108 (Springer Verlag 1979);
Proc. Symp. on Perspectives in Electro- and Photonuclear Physics, Saclay (1980), eds. A. Gérard and C. Samour, Nucl. Phys. A358 (1981).

15) D. Drechsel, invited talk at the Conf. on Electron Physics and Accelerators - The Next Generation, Charlottesville, Virginia, USA (1982), preprint.

16) J. Mougey, M. Bernheim, A. Bussière, A. Gillebert, Phan Xuan Ho, M. Priou, D. Royer, I. Sick, G.J. Wagner, Nucl. Phys. A262(1976) 461.

17) K. Nakamura, S. Hiramatsu, T. Kamae, H. Muramatsu, N. Izutsu, Y. Watase, Nucl. Phys. A268 (1976) 381.

18) M. Bernheim, A. Bussière, J. Mougey, D. Royer, D. Tarnowski, S. Turk-Chieze, S. Frullani, S. Boffi, C. Giusti, F.D. Pacati, G.P. Capitani, E. de Sanctis, G.J. Wagner, Nucl. Phys. A375 (1982) 381.

19) S. Boffi, C. Giusti, F.D. Pacati, S. Frullani, Nucl. Phys. A319 (1979) 461.

20) S. Boffi, C. Giusti, F.D. Pacati, Nucl. Phys. A336 (1980) 416.

21) C. Giusti, F.D. Pacati, Nucl. Phys. A336 (1980) 427.

22) S. Boffi, C. Giusti, F.D. Pacati, Nucl. Phys. A336 (1980) 437.

23) R.K. Natarajan, N. Arunachalam, V. Girija, V. Devanathan, Phys. Rev. C28 (1983) 88;
V.P. Berezovoj, Yu.P. Mel'Nik, A.V. Shebeko, Nucl. Phys. A404 (1983) 443.

24) W. Eyrich, K. Fuchs, A. Hofmann, U. Scheib, M. Steur, H. Rebel, Phys. Rev. C29 (1984) 418.

25) J.R. Calarco et al., Proc. Symp. on Highly Excited States in Nuclear Reactions, eds. H. Ikegami and M. Muraoka, Osaka (1980), p. 543, and private communication.

26) G.O. Bohne, L.J. Koester, L.S. Cardman, R.W. Doerfler, B.L. Miller, C.N. Papanicolas, H. Rothas, contributed paper to the Conf. on Highly Excited States and Nuclear Structure, Orsay, Sept. 5-8, 1983, eds. N. Marty and N. Van Giai.

27) Ch. Cremer, Th. Kihm, K.T. Knöpfle, H. Riedesel, H.J. Emrich, G. Fricke, R. Neuhausen, R. Schneider, J.R. Calarco, Proc. DPG Meeting Innsbruck (1984).

28) D. Drechsel, Proc. Miniconf. on Coincidence Reaction with Electromagnetic Probes, Amsterdam, Nov. 14-15, 1983, preprint.

29) J.D. Bjorken and S.D. Drell, Relativistic Quantum Mechanics, McGraw-Hill, New York, 1964.

30) T. de Forest, J.D. Walecka, Adv. in Phys. 15 (1966) 1.

31) T. de Forest, Jr., Ann. Phys. 45 (1967) 365.

32) H. Arenhövel, D. Drechsel, Nucl. Phys. A233 (1974) 153.

33) W. Fabian, H. Arenhövel, Nucl. Phys. A258 (1976) 461.

34) W. Fabian, H. Arenhövel, Nucl. Phys. A314 (1979) 253.

35) H. Arenhövel, Nucl. Phys. A384 (1982) 287.

36) A.R. Edmonds, Angular Momentum in Quantum Mechanics, Princeton University Press, Princeton, 1957.

37) S. Boffi, C. Giusti, F.D. Pacati, Nucl. Phys. A386 (1982) 599.

38) C. Bloch, Prov. XXXVI Int. School of Physics, Enrico Fermi Course, Academic Press, New York, 1966.

39) C. Mahaux, H.A. Weidenmüller, Shell Model Approach to Nuclear Reactions, North-Holland, Amsterdam, 1969.

40) C.M. Lederer and V.S. Shirley, Table of Isotopes, 7th edition, J. Wiley, New York, 1978.

41) I. Sick, J.S. McCarthy, Nucl. Phys. A150 (1970) 631.

42) S.G. Nilsson, Kgl. Danske Videnskab. Selskab. Mat. Fys. Medd. 29 (1955) 1.

43) Y. Abgrall, B. Morand, E. Caurier, Nucl. Phys. A192 (1972) 372.

44) C.M. Perey, G.F. Perey, At. Data Nucl. Data Tables 13 (1973) 293.

45) G.A. Rinker, J. Speth, Nucl. Phys.A306 (1978) 360.

46) R. de Haro, S. Krewald, J. Speth, Nucl. Phys. A388 (1982) 265.

47) B. Buck, A.D. Hill, Nucl. Phys. A95 (1967) 271;
J. Raynal, M.A. Melkanoff, T. Sawada, Nucl. Phys. A101 (1967) 369;
S. Krewald, J. Birkholz, A. Faessler, J. Speth, Phys. Rev. Lett. 33 (1974) 1385;
M. Cavinato, M. Marangoni, P. Ottaviani, A.M. Saruis, Nucl. Phys. A373 (1982) 445.

48) J. Ahrens, H. Borchert, K.H. Czock, H.B. Eppler, H. Gimm, H. Gundrum, M. Kröning, P. Riehn, G. Sita Ram, A. Zieger, B. Ziegler, Nucl. Phys. A251 (1975) 479, and private communication.

49) J.S. Dehesa, S. Krewald, J. Speth, A. Faessler, Phys. Rev. C15 (1977) 1858.

50) W.D. Myers, W.J. Swiatecki, Nucl. Phys. 81 (1966) 1.

51) K. Nakayama, S. Krewald, J. Speth, G. Love, to be published.

52) G.E. Brown, J.S. Dehesa, J. Speth, Nucl. Phys. A330 (1979) 290.

53) A. Bohr, Nucl. Phys. 10 (1959) 486.

54) K.T. Knöpfle, G.J. Wagner, H. Breuer, M. Rogge, C. Mayer-Böricke, Phys. Rev. Lett. 35 (1975) 779.

55) S. Krewald, Jül-Spez 1315 (1976) (unpublished).

56) G. Mairle, G.J. Wagner, P. Doll, K.T. Knöpfle, H. Breuer, Nucl. Phys. A299 (1978) 39.

57) H. Breuer, G.J. Wagner, K.T. Knöpfle, G. Mairle, P. Doll, Phys. Lett. 96B (1980) 35.

58) D.B. Holtkamp, W.J. Braithwaite, W. Cottingame, S.J. Greene, R.J. Joseph, C.F. Moore, J. Piffaretti, E.R. Siciliano, H.A. Thiessen, D. Dehnhard, Phys. Rev. Lett. 45 (1980) 420.

59) W. Bertozzi, Nucl. Phys. A374 (1982) 109c.

60) F.C. Barker, R. Smith, I. Morrison, K. Amos, J. Phys. G7 (1981) 657.

61) A.E.L. Dieperink, T. de Forest Jr., Ann. Rev. Nucl. Sci. 25 (1975) 1.

62) V.V. Balashov, S.I. Grishanova, N.M. Kabachnik, V.M. Kulikov, N.N. Titarenko, Nucl. Phys. A216 (1973) 574.

63) W.R. Dodge, E. Hayward, R.G. Leicht, B.H. Patrik, R. Starr, Phys. Rev. Lett. 44 (1980) 1040.

64) V.V. Balashov, N.M. Kabachnik, V.I. Markov, Nucl. Phys. A129 (1969) 369.

65) V.V. Balashov, E.F. Kishyakov, V.L. Korotkikh, R. Wünsch, Nucl. Phys. A345 (1980) 367.

TABLE CAPTIONS

Table 1: Parameters of the Saxon-Woods potential of eq. (42) for ^{12}C and ^{16}O. Note that we used $a_{SO}=a$ and $R_{SO}=R_C=R_o$.

Table 2: Energies in MeV of the bound single particle levels of ^{16}O. The experimental values have been taken from the level scheme of the neighbouring nuclei[40)].

Table 3: The same as Table 2 for ^{12}C.

Table 4: Parameters of the Landau-Migdal density dependent p-h interaction used in the present work. This parametrization of the force has been taken from Ref. 45.

Table 5: Values of the force constant C_0, interpolation radius R and diffuseness α used for ^{12}C and ^{16}O (see eq. (45)).

Table 6: Contribution, in percentage, of the charge term of eq. (20) to the integrated cross sections of Fig. 25.

TABLE 1

		V_o (MeV)	R (fm)	a_o (fm)	V_{SO} (MeV)
^{12}C	protons	62.0	2.86	0.57	3.20
	neutrons	60.0	2.86	0.57	3.15
^{16}O	protons	52.5	3.2	0.53	7.0
	neutrons	52.5	3.2	0.53	6.54

TABLE 2

^{16}O		protons		neutrons	
		exp	s.w.	exp	s.w.
p	$2s_{1/2}$	-0.10	-0.86	-3.27	-3.95
	$1d_{5/2}$	-0.60	-3.71	-4.14	-6.88
	$1p_{1/2}$	-12.11	-12.67	-15.65	-16.66
h	$1p_{3/2}$	-18.44	-16.84	-21.81	-20.54
	$1s_{1/2}$	-	-29.81	-	-34.00

TABLE 3

^{12}C	protons		neutrons	
	exp.	S.W.	exp.	W.S.
$1d_{5/2}$			-1.10	-3.54
$2s_{1/2}$			-1.86	-3.31
$1p_{1/2}$	-1.94	-15.14	-4.96	-17.34
$1p_{3/2}$	-15.96	-17.45	-18.72	-19.61
$1s_{1/2}$	-	-33.13	-	-36.2

TABLE 4

f_{in}	f_{ext}	f'_{int}	f'_{ext}	g	g'
0.20	-2.45	1.50	1.50	0.55	0.70

TABLE 5

	C_0 (MeV fm^3)	interp. radius R (fm)	diffuseness (fm)
^{12}C	193.019	2.46	0.60
^{16}O	253.531	2.71	0.60

TABLE 6

E (MeV)	ε_i = 100 MeV		ε_i = 180 MeV	
	no p-h int.	with p-h int.	no p-h int.	with p-h int.
25	81.8	92.1	77.7	91.0
30	90.1	89.8	82.7	84.9
35	88.8	89.0	82.4	85.8
40	85.6	82.8	81.3	76.5

FIGURE CAPTIONS

Fig. 1: One photon-exchange diagram for the process (e,e'N).

Fig. 2: Geometry of the (e,e'N) process. The initial and final electron momenta are denoted $\vec{k}_i$ and $\vec{k}_f$ respectively, while $\vec{p}$ represents the momentum of the emitted particle forming an angle φ_p with the scattering plane fixed by the two vectors $\vec{k}_i$ and $\vec{k}_f$.

Fig. 3: Energy dependence of the total photo-absorption cross section compared with the experimental data of Ahrens et al.[48)]. The theoretical curve has been computed including the $1^-,2^+,3^-$ multipole excitation modes. Note that the electric dipole gives a contribution of 97.1 % to the total cross section up to an excitation energy of 40 MeV.

Fig. 4: Sensitivity of the angular distribution of the emitted particle to the presence of large multipole excitation modes. The detected proton is coming from the $1p_{1/2}$ bound state. The dashed lines have been calculated including the $0^+,1^-,2^+$ excitation modes, the full curves with all the positive and negative multipole excitations up to J=4. The contributions of higher order multipoles do not produce any sensitive difference in the figure. Note that, for our choice of the reference system, a direct knock-out reaction would have maximal cross section for $\vartheta_p = 180^0$. The value of the momentum transfer is 0.64 fm^{-1} for Fig. a and 0.89 fm^{-1} for Fig. b.

Fig. 5: The same as Fig. 4 but for a nuclear excitation energy of 40 MeV. Full and dashed lines have the same meaning as in Fig. 4, the dotted lines represent the result of a computation performed including all the modes up to J=6. Note that for $\vartheta_e = 165^0$ the emitted particle angular distribution starts to be sensitive to the higher multipole excitation modes. The value of the momentum transfer is 0.59 fm^{-1} in a) and 0.80 fm^{-1} in b).

Fig. 6: The same as Fig. 5 but for a different value of the incoming electron energy. The emitted proton is coming from the $1p_{1/2}$ state. The full curve represents the result of the calculation performed using all the multipole excitation modes up to J=4, the dashed curve up to J=5 and the dotted one up to J=6. In this case the shape of the angular distribution of the emitted particle is deeply modified by the presence of multipoles with angular momentum higher than J=4. The value of the momentum transfer is 1.16 fm^{-1}.

Fig. 7: Sensitivity of the angular distribution of the emitted proton for the reaction $^{16}O(e,e'p_0)^{15}N$, to the presence of monopole strength. In both figures the full lines have been calculated using all the positive and negative multipole modes up to J=4. The dashed lines represent the results of the calculations performed leaving out the 0^+ excitation mode. The values of the transfer momentum are q = 0.33 fm^{-1} in Fig. a and q = 0.46 gfm^{-1} in Fig. b respectively.

Fig. 8: Dependence of the four kinematical factors defined in eq. (7) from the angle of the scattered electron under the kinematical conditions of Fig. 4.

Fig. 9: Contribution of the four terms of the coincidence cross section of eq. (20) to the angular distribution of the emitted particle under the kinematical conditions of Fig. 4a. The contributions of the current and current-current interference terms are enhanced by a factor 30. While all the terms are symmetric under a reflection around $\vartheta_p = 180^o$, the charge-current term is antisymmetric because of its $\cos\varphi_p$ dependence which changes sign for ϑ_p larger than 180^o. The breaking of the reflection symmetry in the total emitted particle angular distribution is given by the presence of the charge-current interference term.

Fig. 10: The same as Fig. 9 but for a higher value of the angle of the scattered electron. In this plot the current-current interference term has been enhanced 100 times. Note that the dominant contribution here is given by the current term.

Fig. 11: The angular distribution of the emitted particle as a function of the excitation energy of the nucleus for fixed values of the incoming electron energy ε_i = 100 MeV and of the scattering angle $\vartheta_e = 90^o$. The emitted particle, coming from the $1p_{1/2}$ state, is detected in the scattering plane. The calculation has been performed including all the positive and negative multipole modes up to J=4. The values of the momentum transfer are going from 0.61 fm^{-1} up to 0.66 fm^{-1}.

Fig. 12: Contribution of the 2^+ multipole excitation mode to the total photoabsorption cross section shown in Fig. 3.

Fig. 13: Emitted particle angular distribution at the peak energy 23.5 MeV. The full line is the angular distribution of the calculation of Fig. 11. The dashed line has been computed without the 2^+ excitation mode and the dotted line without the 1^-.

Fig. 14: Momentum distribution of electric dipole and quadrupole excitations at the peak energy of 23.5 MeV for a proton emitted from $1p_{1/2}$ bound level. The value of the momentum transfer was changed modifying the incoming electron energy.

Fig. 15: The same as Fig. 11 but for a different value of the incoming electron energy ε_i. The computation has been performed including all the positive and negative multipole modes up to J=6. The range of the momentum transfer values covered by the computation is $1.15<q<1.23$ fm^{-1}. This figure is plotted in the same scale as used in Fig. 11.

Fig. 16: Angular distribution of the emitted particle at the peak energy E = 23.5 MeV under the kinematic conditions of Fig. 15. The full line is the angular distribution of the calculation of Fig. 15. The dashed line has been computed without the 2^+ excitation mode and the dotted line without the 1^- mode. The rather good forward ($\vartheta_p = 180^0$) backward ($\vartheta_p = 0^0$) symmetry of the full line is a signature of the fact that at this momentum transfer, q = 1.2 fm^{-1}, the contribution of the

electric dipole is rather small and the resonance is built up practically by the 2^+ mode alone.

Fig. 17: Contribution of the 3^- excitation mode to the total photoabsorption cross section of Fig. 3.

Fig. 18: The full line is the angular distribution of the calculation of Fig. 15 at the excitation energy E = 19 MeV. The dashed line has been calculated without the 3^- excitation mode.

Fig. 19: The same as Fig. 15 but for the detection of the proton coming from the $1p_{3/2}$ state.

Fig. 20: Contribution of the four terms of the coincidence cross section to the angular distribution of the emitted particle of Fig. 19 at the excitation energy E = 20 MeV. The fact that the current term strongly dominates the others is a possible indication of the presence of magnetic states. Note that in the figure the charge term has been enhanced 20 times.

Fig. 21: Comparison between the angular distribution of the emitted particle of Fig. 19 at E = 20 MeV (full line) and the result of the computation performed without the 4^- multipole excitation mode (dashed line).

Fig. 22: The full line is the angular distribution of the emitted particle of Fig. 11 at the peak energy of the giant resonance. The dashed line is

the result of an analogous computation performed switching off the particle-hole interaction to simulate the quasi-free scattering approach. The dashed line has the characteristic behaviour of the Fourier transformation of the $1p_{1/2}$ hole state. The value of the momentum of the emitted proton $\vec{p}$ is 0.74 fm^{-1} and the value of the transfer momentum $\vec{q}$ is 0.64 fm^{-1}.

Fig. 23: The same as Fig. 22 but for the excitation energy E = 40 MeV. Under this kinematic conditions the momentum of the emitted proton is $\vec{p}$ = 1.16 fm^{-1} and the transfer momentum value $\vec{q}$ is 0.59 fm^{-1}.

Fig. 24: The same as Fig. 23 but for an incoming electron energy of 180 MeV. In this case the stability of the cross section was reached including all the multipole positive and negative modes up to J=6. The values of $\vec{p}$ and $\vec{q}$ under these kinematic conditions are roughly equal (1.16 fm^{-1}) and the characteristic shape given by the $1p_{1/2}$ hole is present. The asymmetry between the two bumps is given by the $\cos\varphi_p$ dependence of the charge-current interference term.

Fig. 25: The coincidence cross section for the reaction $^{16}O(e,e'p_0)^{15}N$ integrated over the angle ϑ_p of the emitted particle is shown as a function of the nuclear excitation energy E. The dashed lines present the results of the computations performed without p-h interaction and the continuous lines show the results of the calculations with p-h interaction included. In a) the two curves have been computed under the kinematic conditions of Fig. 11, and in b) under the kinematic conditions of Fig. 15.

Fig. 26: The photoabsorption cross section of ^{12}C by Ahrens et al.[48] is compared with the 1^- solution of the continuum random-phase-approximation.

Fig. 27: The experimental double differential cross section by Calarco et al.[25] is compared with the result of our theoretical calculation. The full lines represent the result of the calculation performed including all positive and negative parity states up to J=4. The dashed lines represent the result of the calculation performed without monopole strength. Note that all the theoretical energies have been shifted up by 1.5 MeV and the magnitudes of all theoretical cross sections are scaled by a factor λ = 0.4.

Fig. 28: The exhaustion of the energy-weighted sum rule as a function of the excitation energy for monopole (full line), dipole (dashed line), and quadrupole (dotted line) strength.

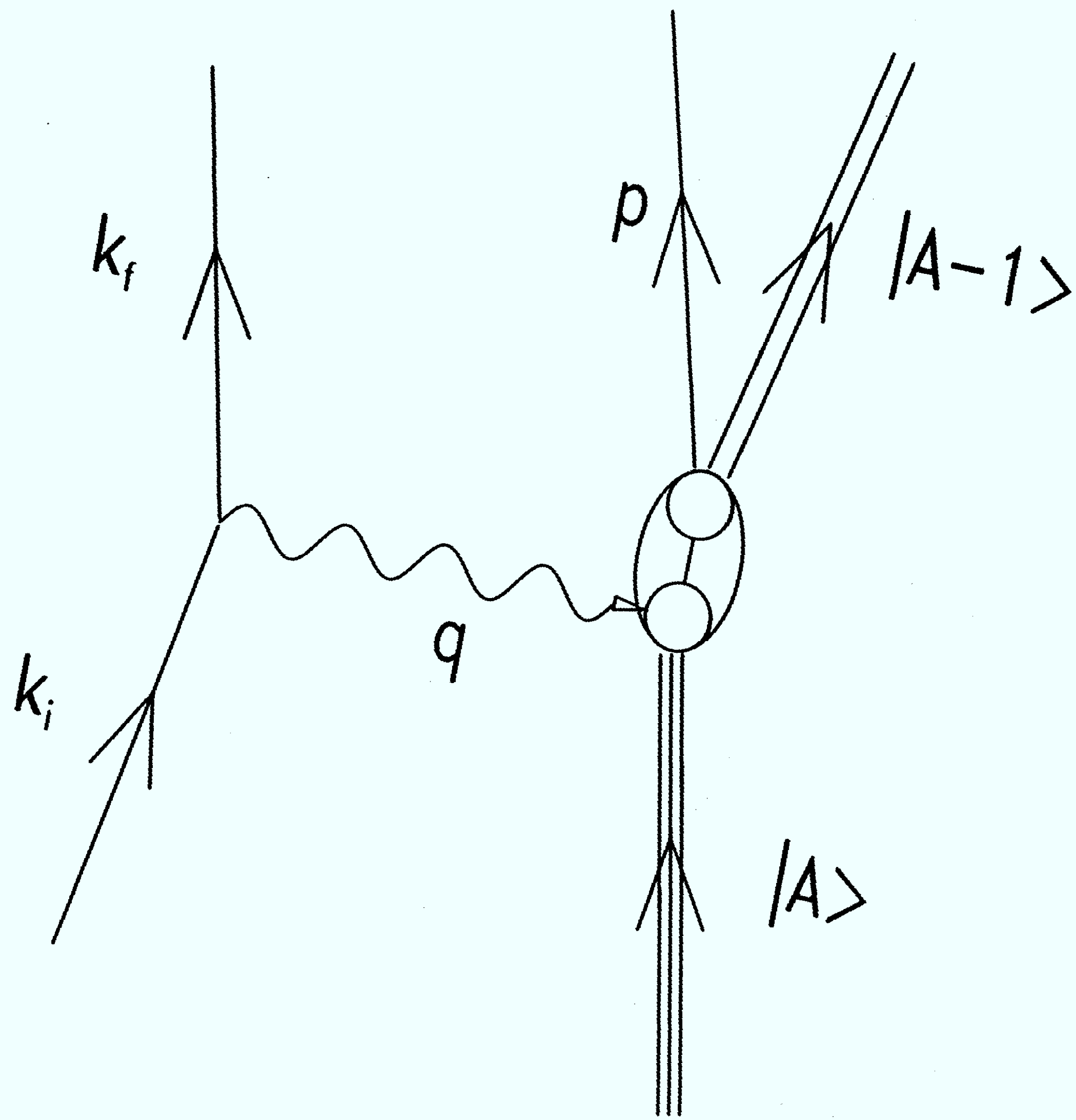

Fig. 1

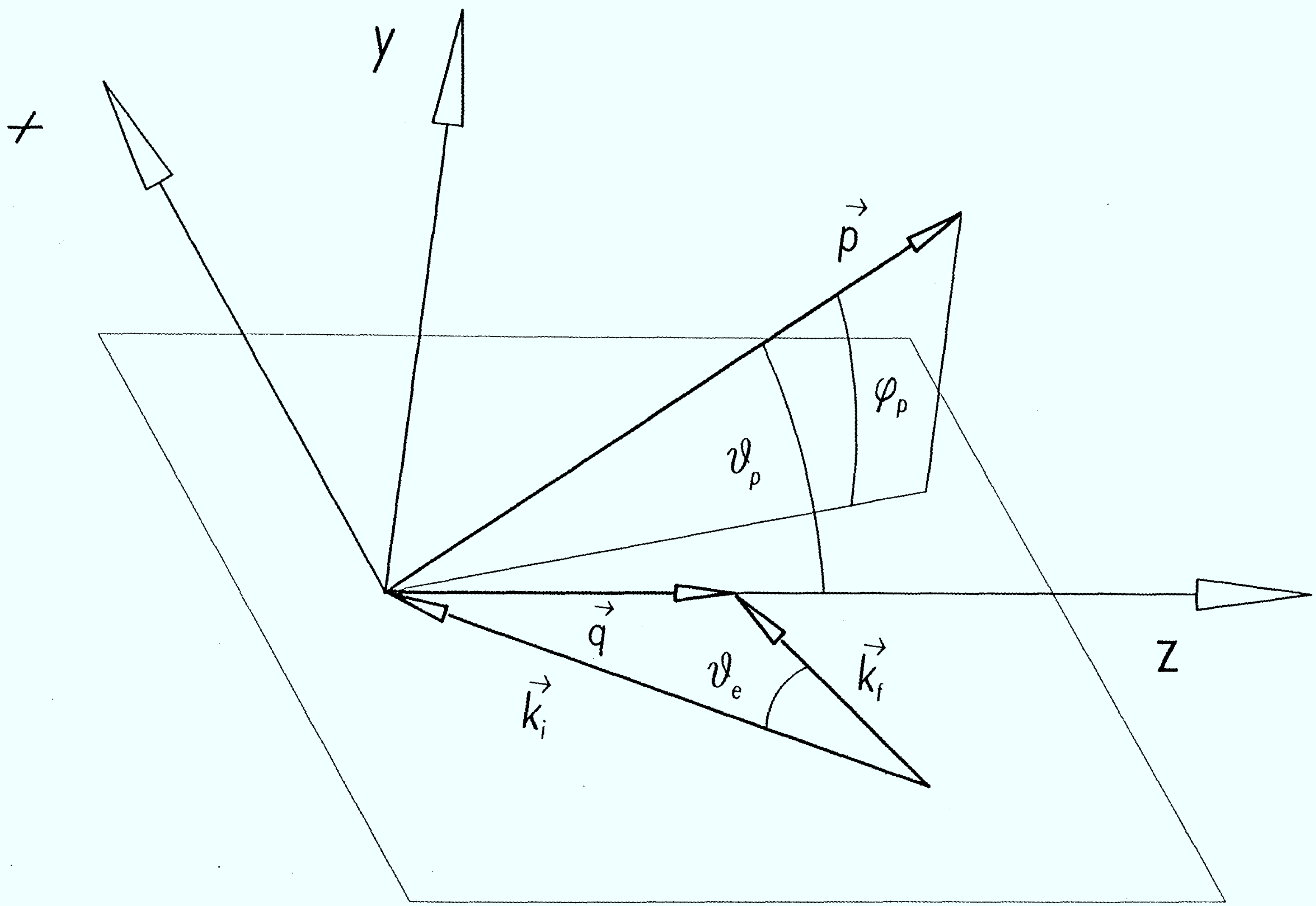

Fig. 2

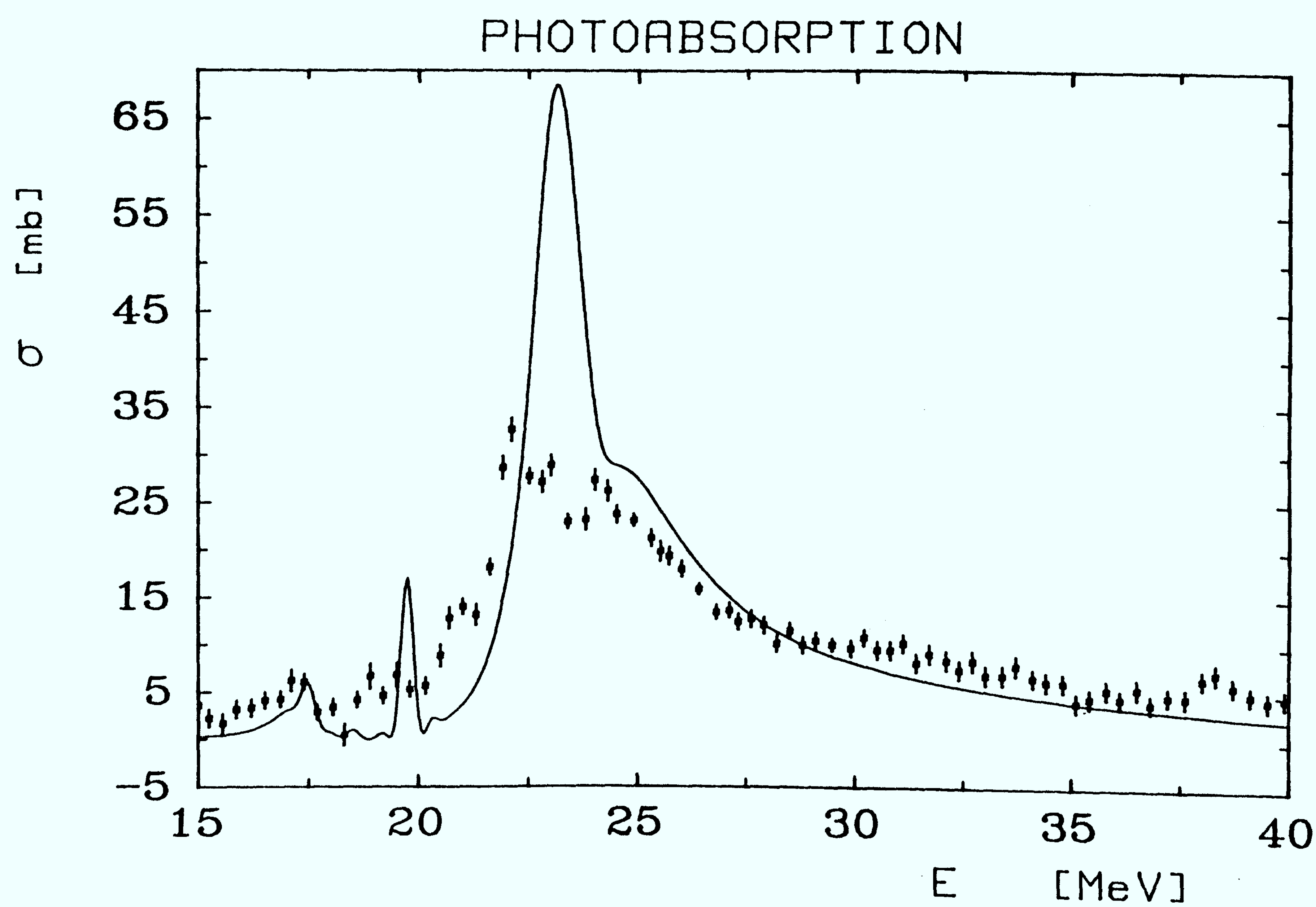

Fig. 3

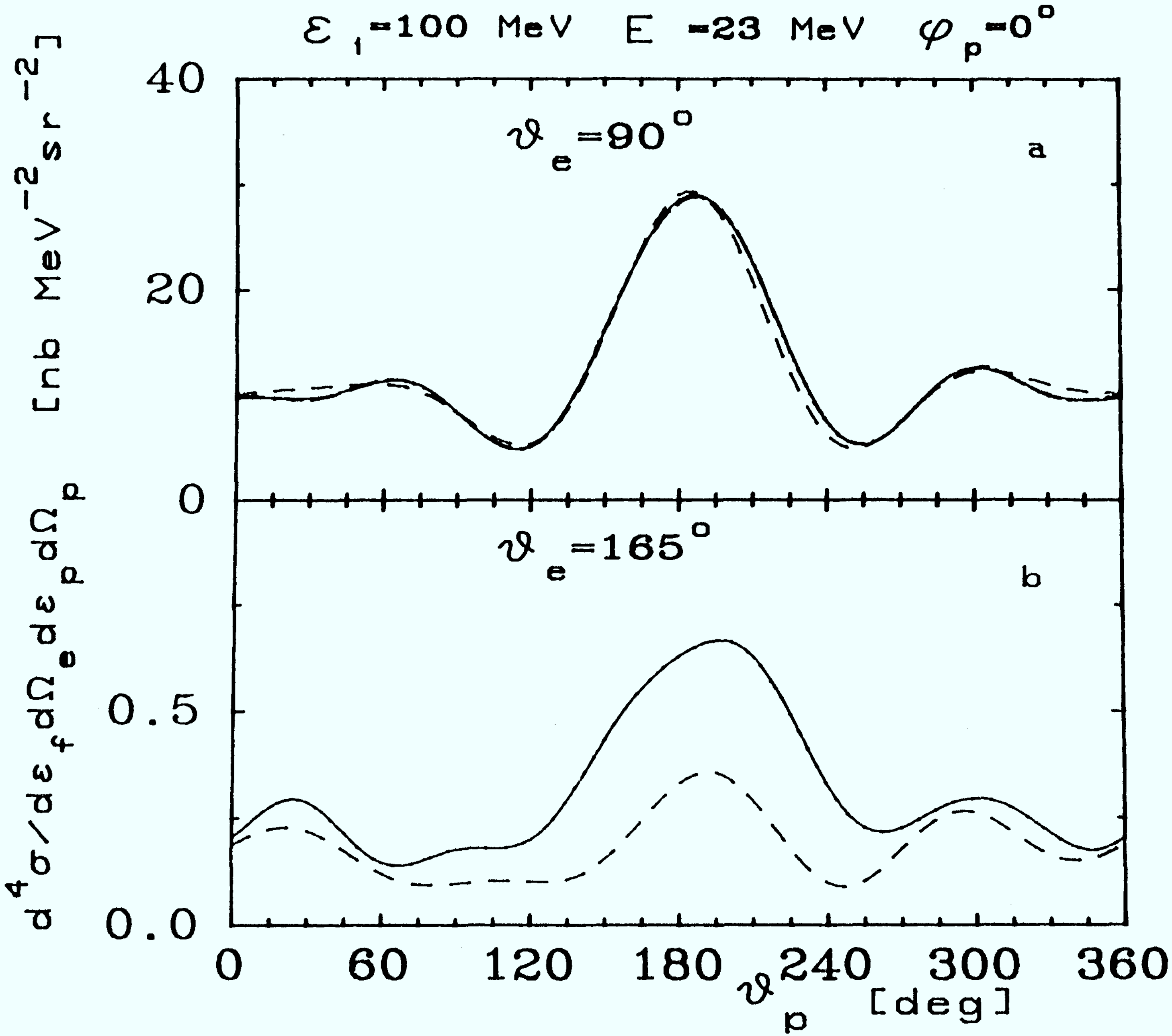

ε i=100 MeV E =23 MeV φp=0°
ϑe=90°
a
ϑe=165°
b
40
20
0
0.5
0.0
0
60
120
180
240
300
360
ϑp [deg]
d4σ/dεfdΩedεpdΩp [nb MeV-2sr-2]

Fig. 4

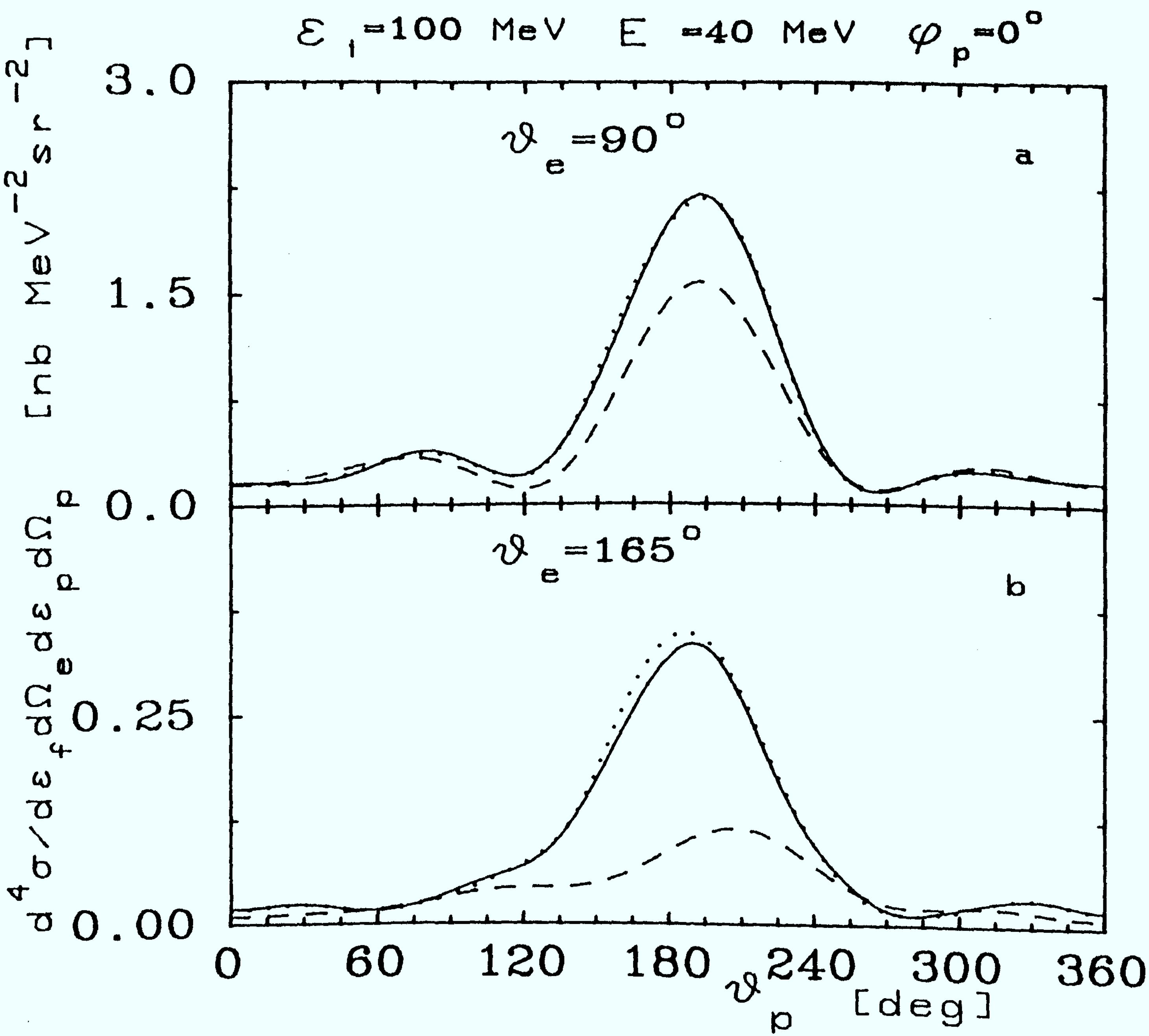
ε1=100 MeV E =40 MeV φp=0°
ϑe=90°
a
ϑe=165°
b
3.0
1.5
0.0
0.25
0.00
d4σ/dεfdΩedεpdΩp [nb MeV-2sr-2]
0
60
120
180
240
300
360
ϑp [deg]

Fig. 5

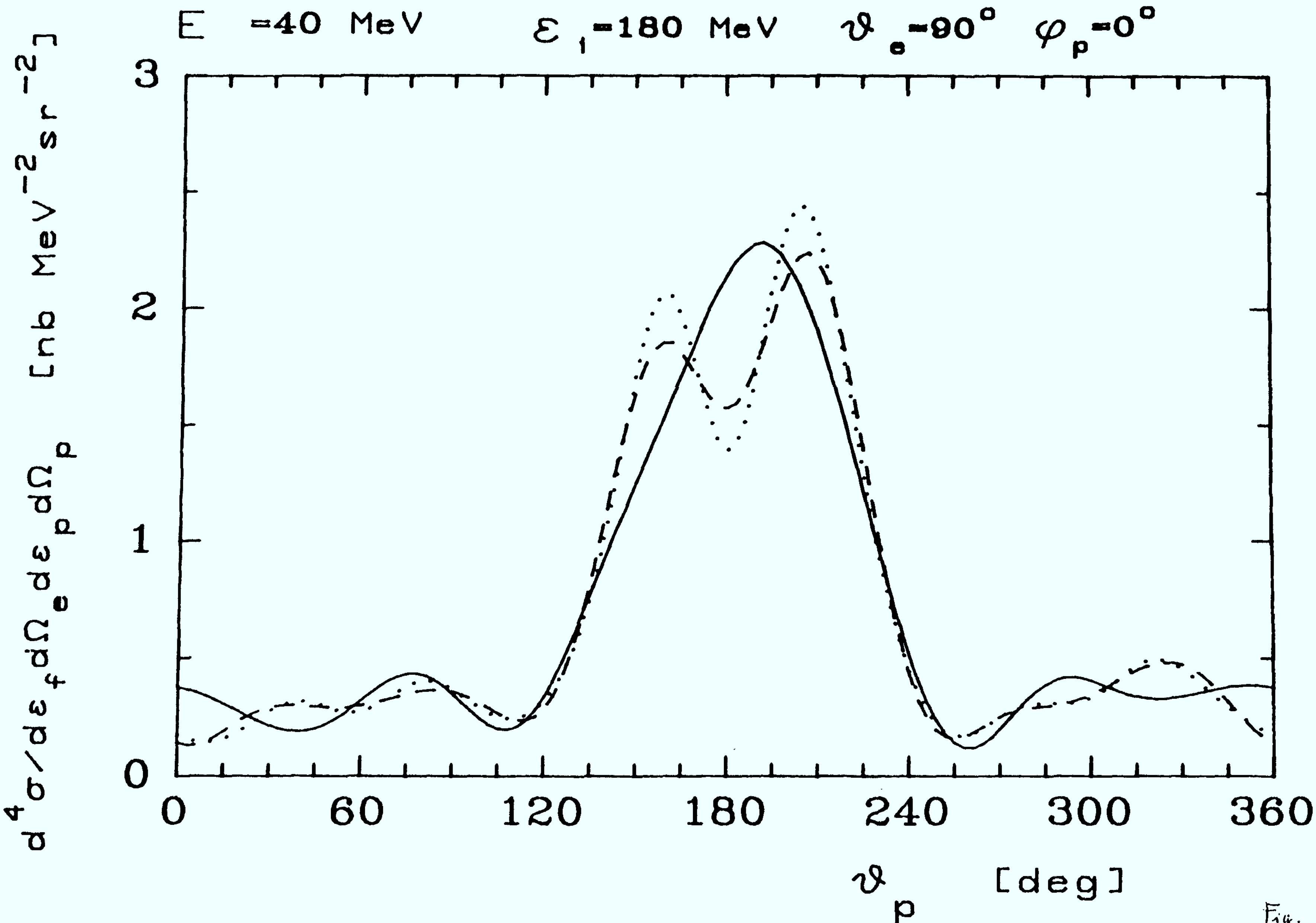
E =40 MeV
ε_1=180 MeV
ϑ_e=90°
φ_p=0°
$d^4\sigma/d\varepsilon_f d\Omega_e d\varepsilon_p d\Omega_p$ [nb MeV^{-2}sr^{-2}]
0
1
2
3
0
60
120
180
240
300
360
ϑ_p [deg]

Fig. 6

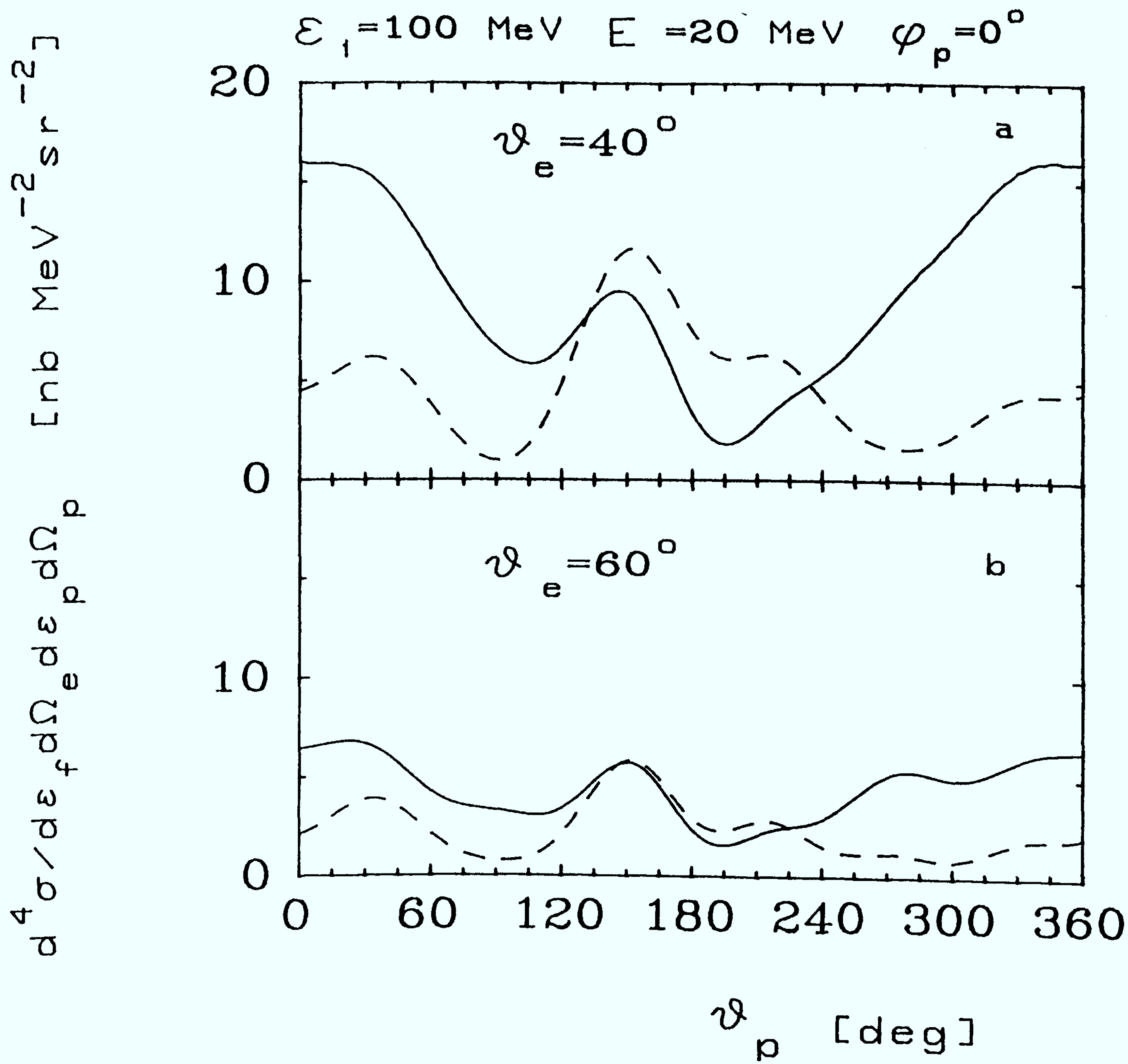

ε_i=100 MeV E =20 MeV φ_p=0°
ϑ_e=40°
a
ϑ_e=60°
b
20
10
0
10
0
0
60
120
180
240
300
360
$d^4\sigma/d\varepsilon_f d\Omega_e d\varepsilon_p d\Omega_p$ [nb MeV^{-2}sr^{-2}]
ϑ_p [deg]

Fig. 7

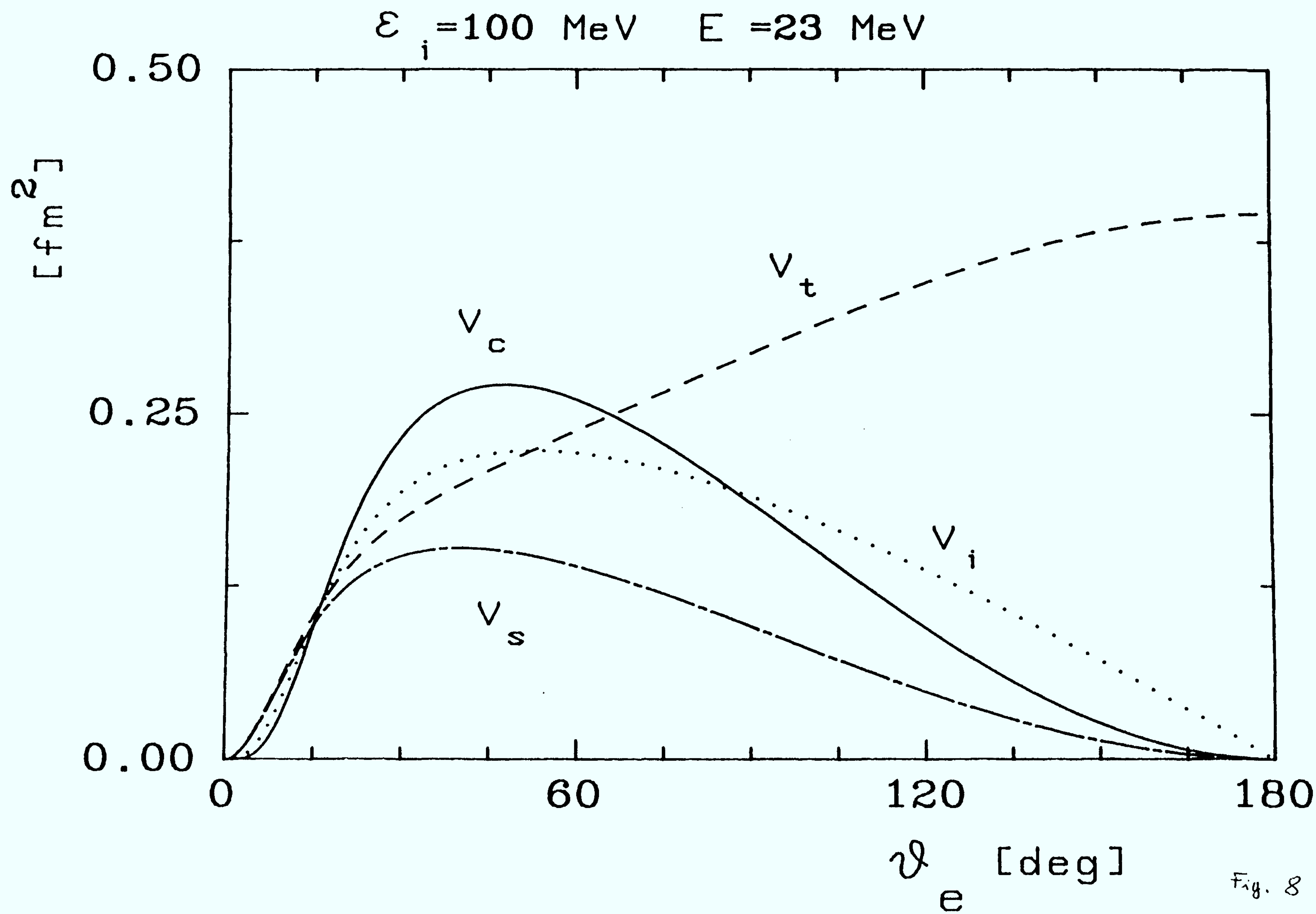

Fig. 8

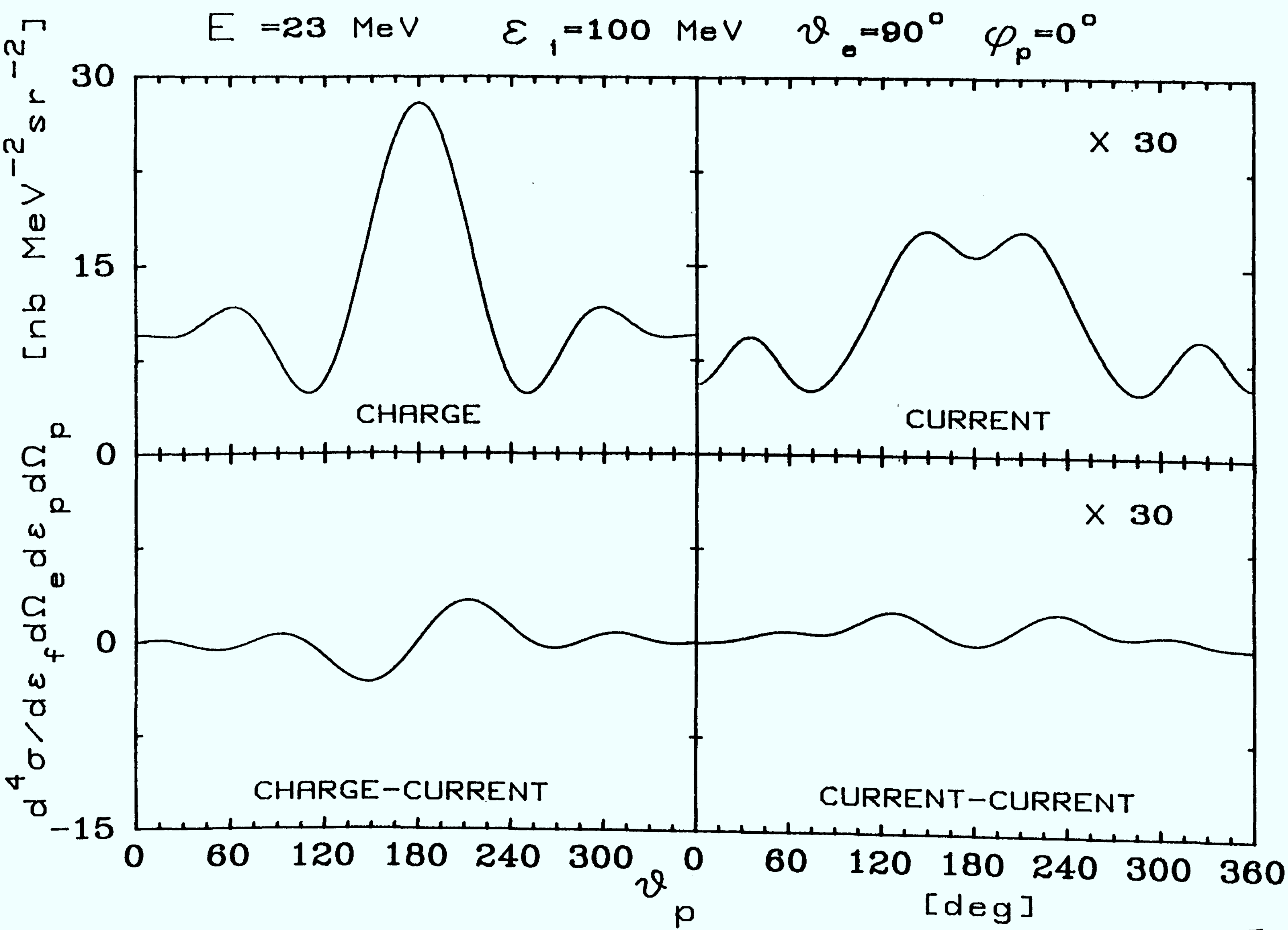

E =23 MeV
ε1=100 MeV
ϑe=90°
φp=0°
d4σ/dεfdΩedεpdΩp [nb MeV-2sr-2]
30
15
0
0
-15
CHARGE
CURRENT
CHARGE-CURRENT
CURRENT-CURRENT
X 30
X 30
0
60
120
180
240
300
0
60
120
180
240
300
360
ϑp
[deg]

Fig. 9

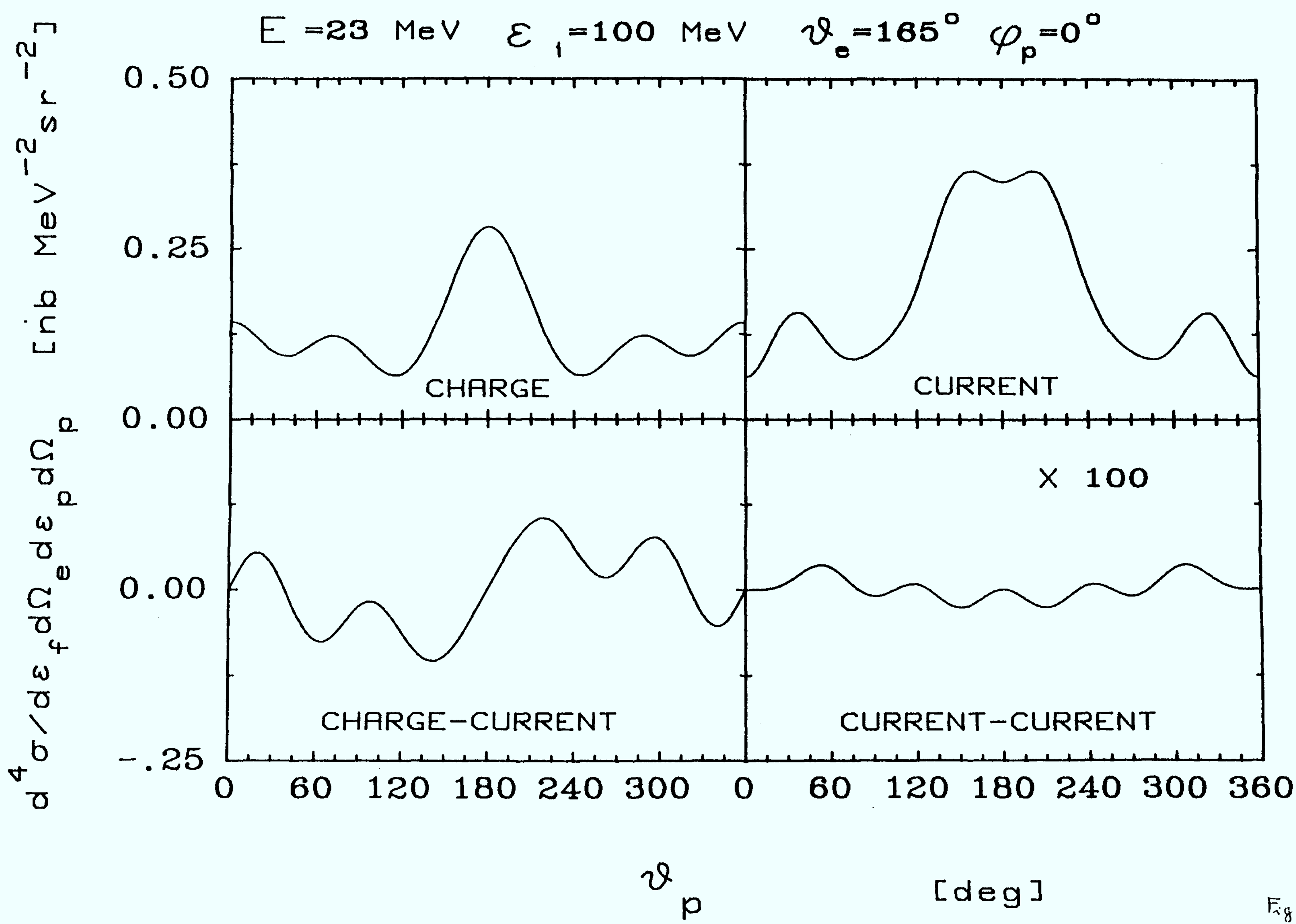

E =23 MeV ε 1=100 MeV ϑe=165° φp=0°
0.50
0.25
0.00
0.00
-.25
[nb MeV-2sr-2]
d4σ/dεfdΩedεpdΩp
CHARGE
CURRENT
X 100
CHARGE-CURRENT
CURRENT-CURRENT
0 60 120 180 240 300 0 60 120 180 240 300 360
ϑp
[deg]

Fig. 10

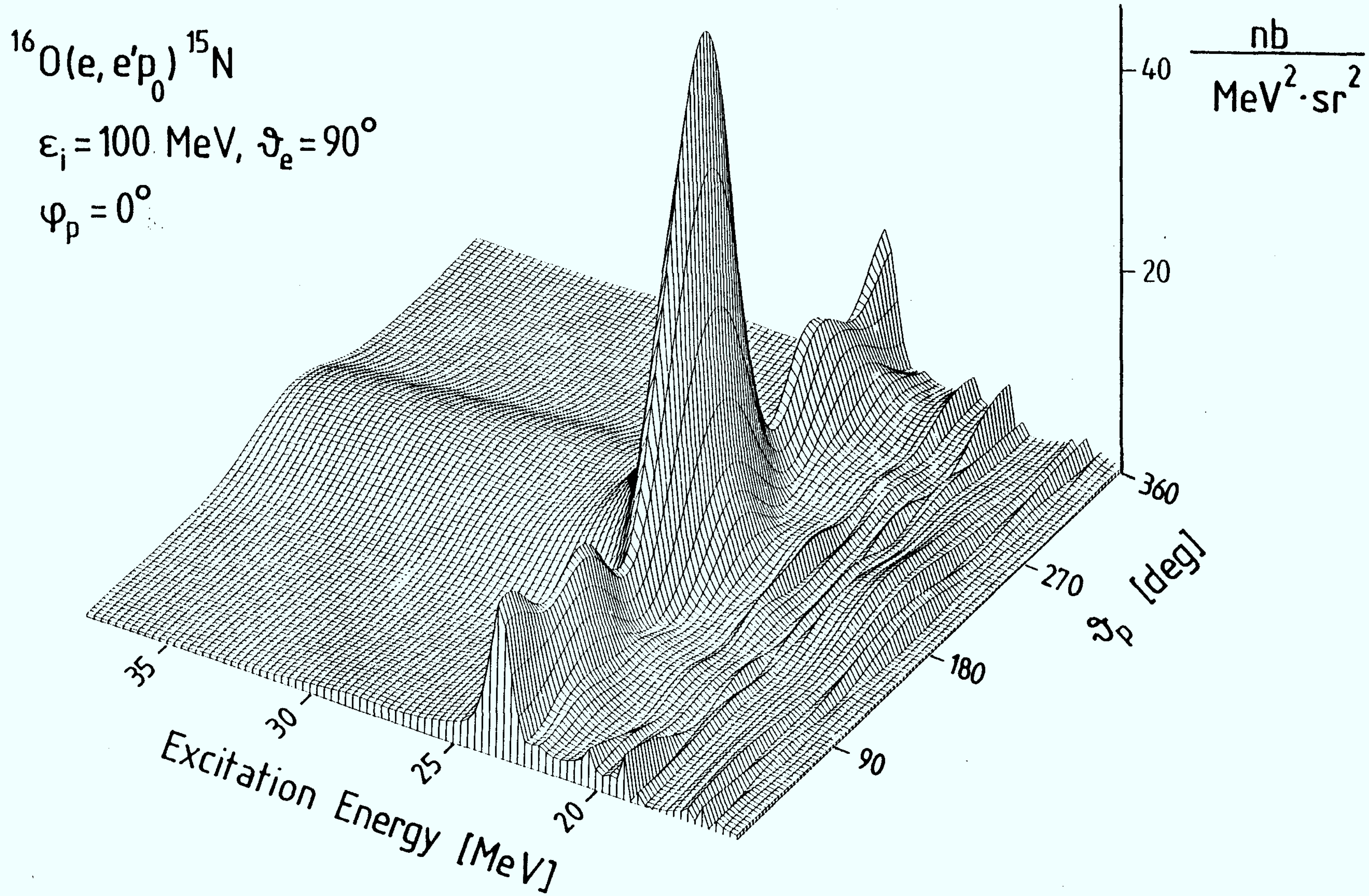

$^{16}O(e,e'p_0)^{15}N$
$\varepsilon_i = 100$ MeV, $\vartheta_e = 90°$
$\varphi_p = 0°$
nb / MeV^2·sr^2
40
20
360
270
180
90
ϑ_p [deg]
35
30
25
20
Excitation Energy [MeV]

Fig. 11

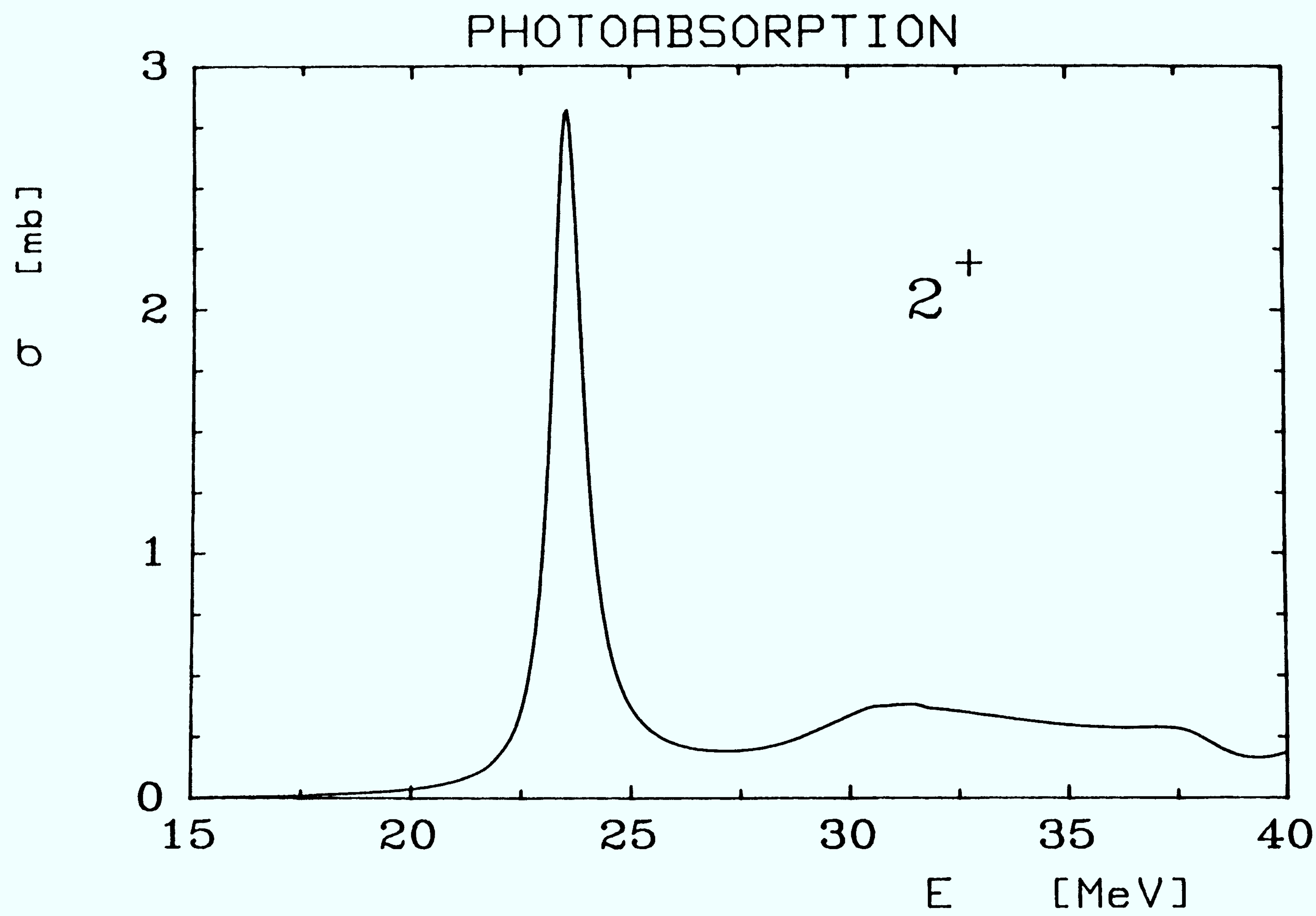

Fig. 12

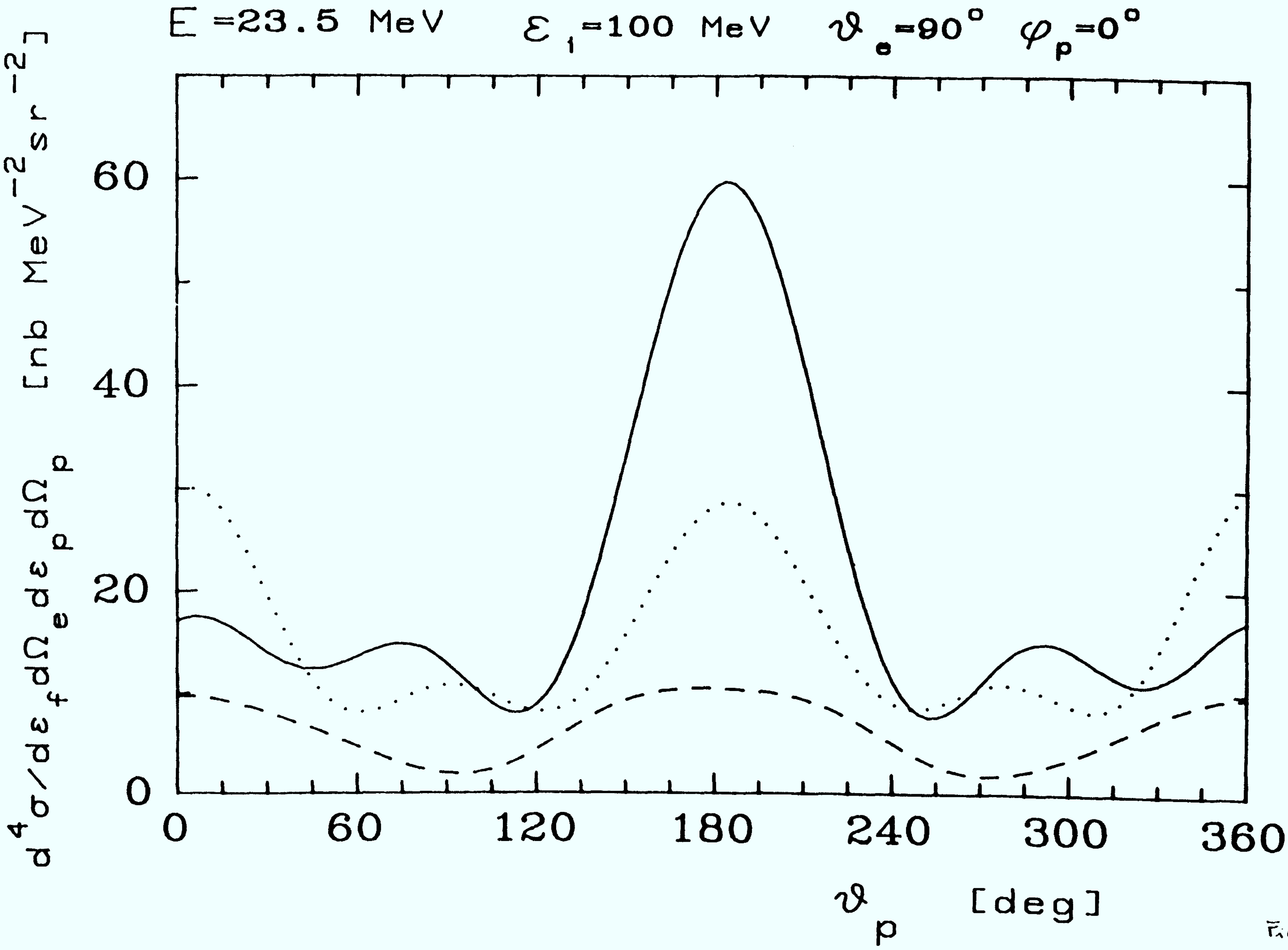
E =23.5 MeV
$\mathcal{E}_1$=100 MeV
ϑ_e=90°
φ_p=0°
$d^4\sigma/d\varepsilon_f d\Omega_e d\varepsilon_p d\Omega_p$ [nb MeV^{-2}sr^{-2}]
60
40
20
0
0
60
120
180
240
300
360
ϑ_p [deg]

Fig. 13

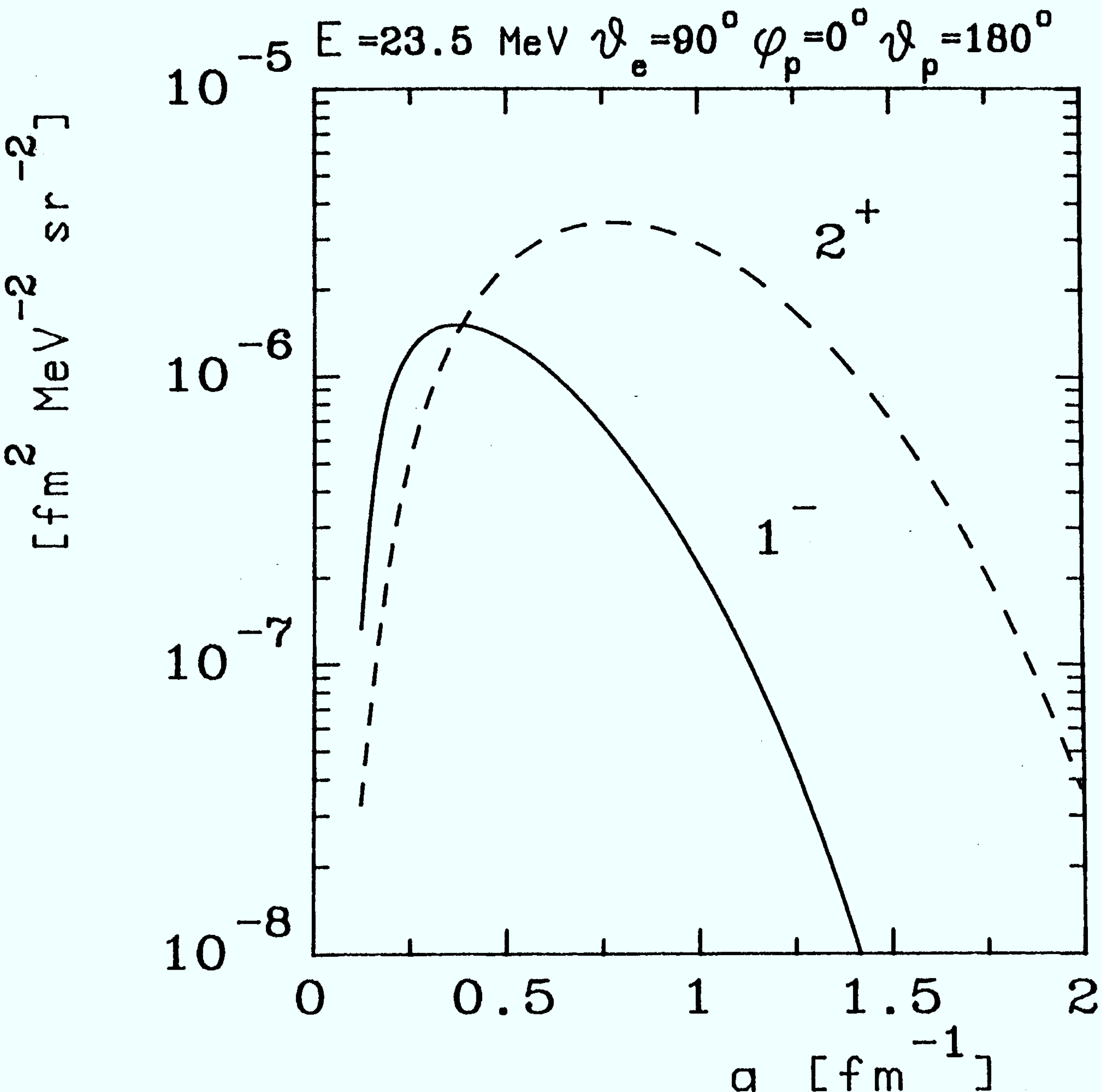
E =23.5 MeV ϑ_e=90° φ_p=0° ϑ_p=180°
10^{-5}
10^{-6}
10^{-7}
10^{-8}
[fm^2 MeV^{-2} sr^{-2}]
2^+
1^-
0
0.5
1
1.5
2
q [fm^{-1}]

Fig. 14

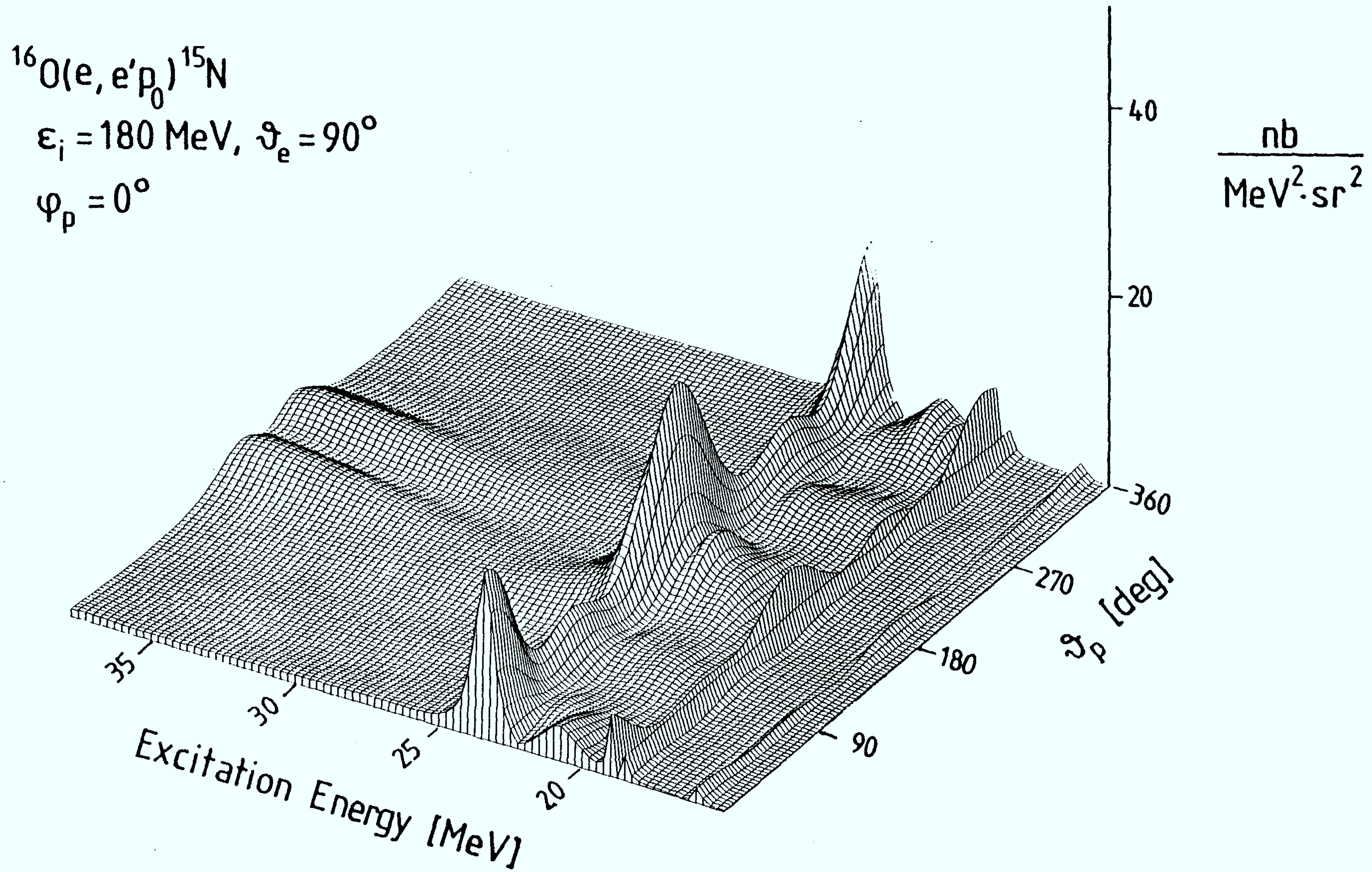
$^{16}O(e, e'p_0)^{15}N$
$\varepsilon_i = 180$ MeV, $\vartheta_e = 90°$
$\varphi_p = 0°$
40
20
360
$\frac{nb}{MeV^2 \cdot sr^2}$
270
180
90
ϑ_p [deg]
35
30
25
20
Excitation Energy [MeV]

Fig. 15

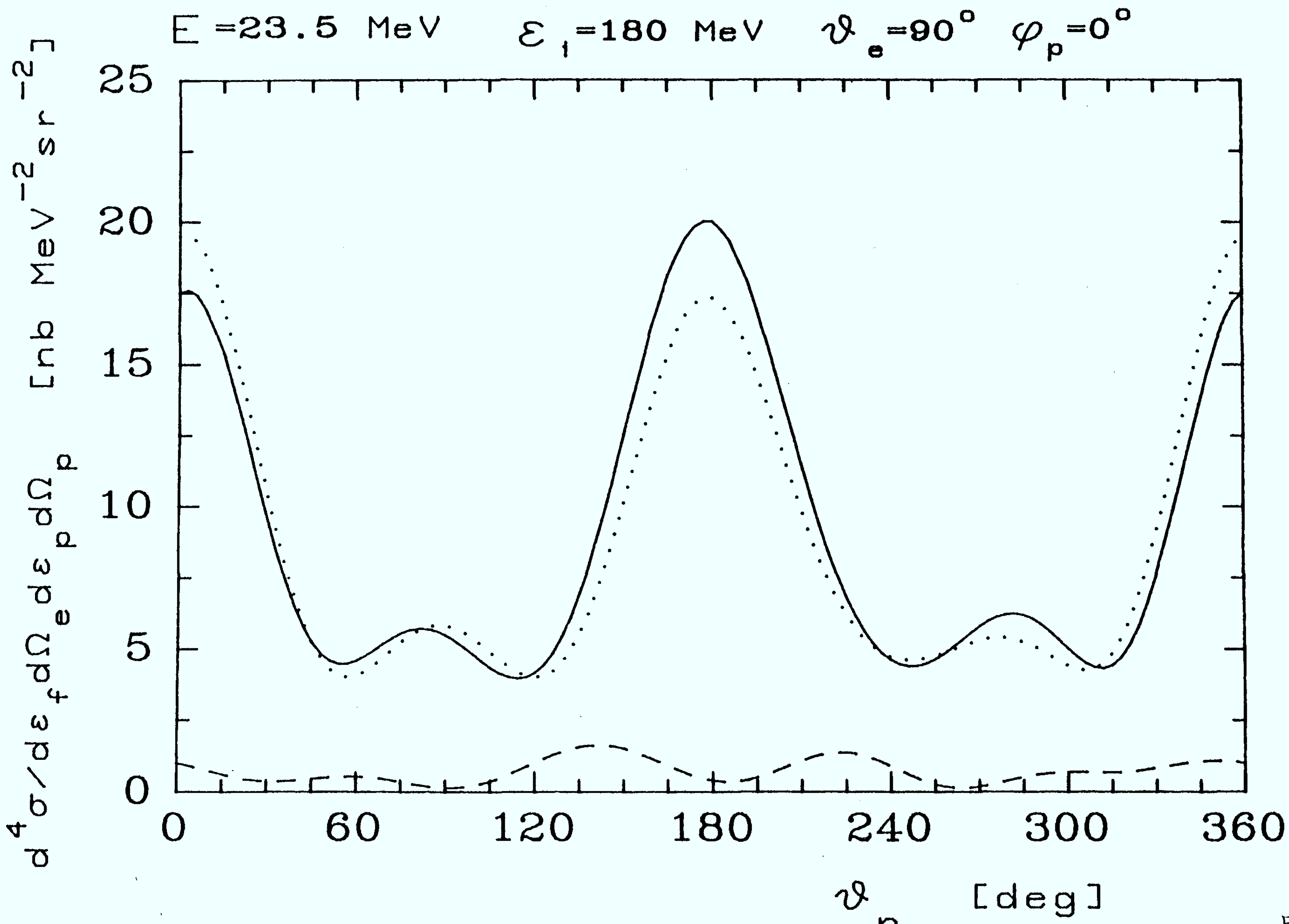

E =23.5 MeV   ε₁=180 MeV   ϑ_e=90°   φ_p=0°
d⁴σ/dε_f dΩ_e dε_p dΩ_p   [nb MeV⁻² sr⁻²]
25
20
15
10
5
0
0
60
120
180
240
300
360
ϑ_p   [deg]

Fig. 16

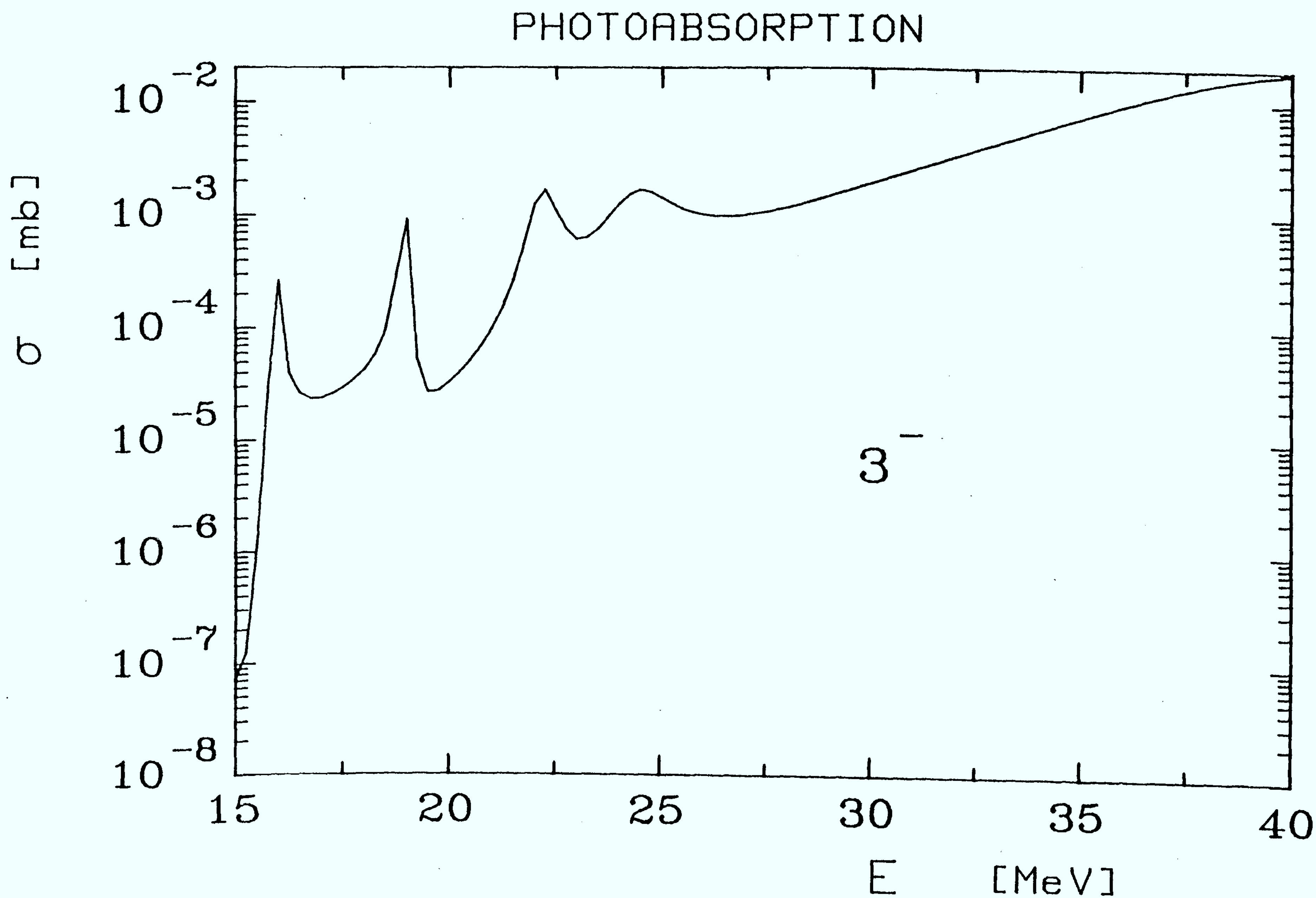
PHOTOABSORPTION
σ [mb]
10^-2
10^-3
10^-4
10^-5
10^-6
10^-7
10^-8
3^-
15
20
25
30
35
40
E [MeV]

Fig. 17

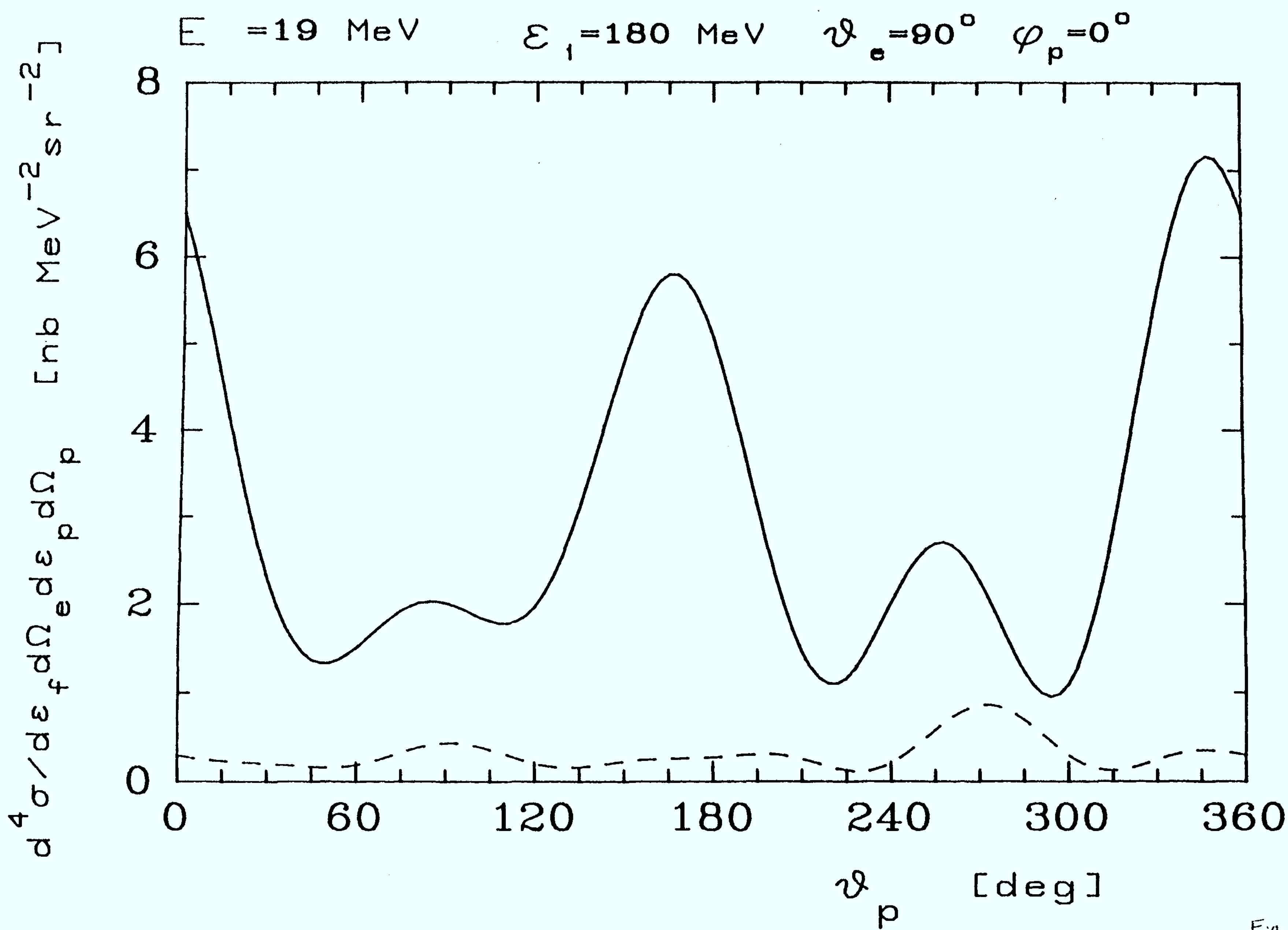

E =19 MeV
ε_1=180 MeV
ϑ_e=90°
φ_p=0°
$d^4\sigma/d\varepsilon_f d\Omega_e d\varepsilon_p d\Omega_p$ [nb MeV^{-2}sr^{-2}]
0
2
4
6
8
0
60
120
180
240
300
360
ϑ_p [deg]

Fig. 18

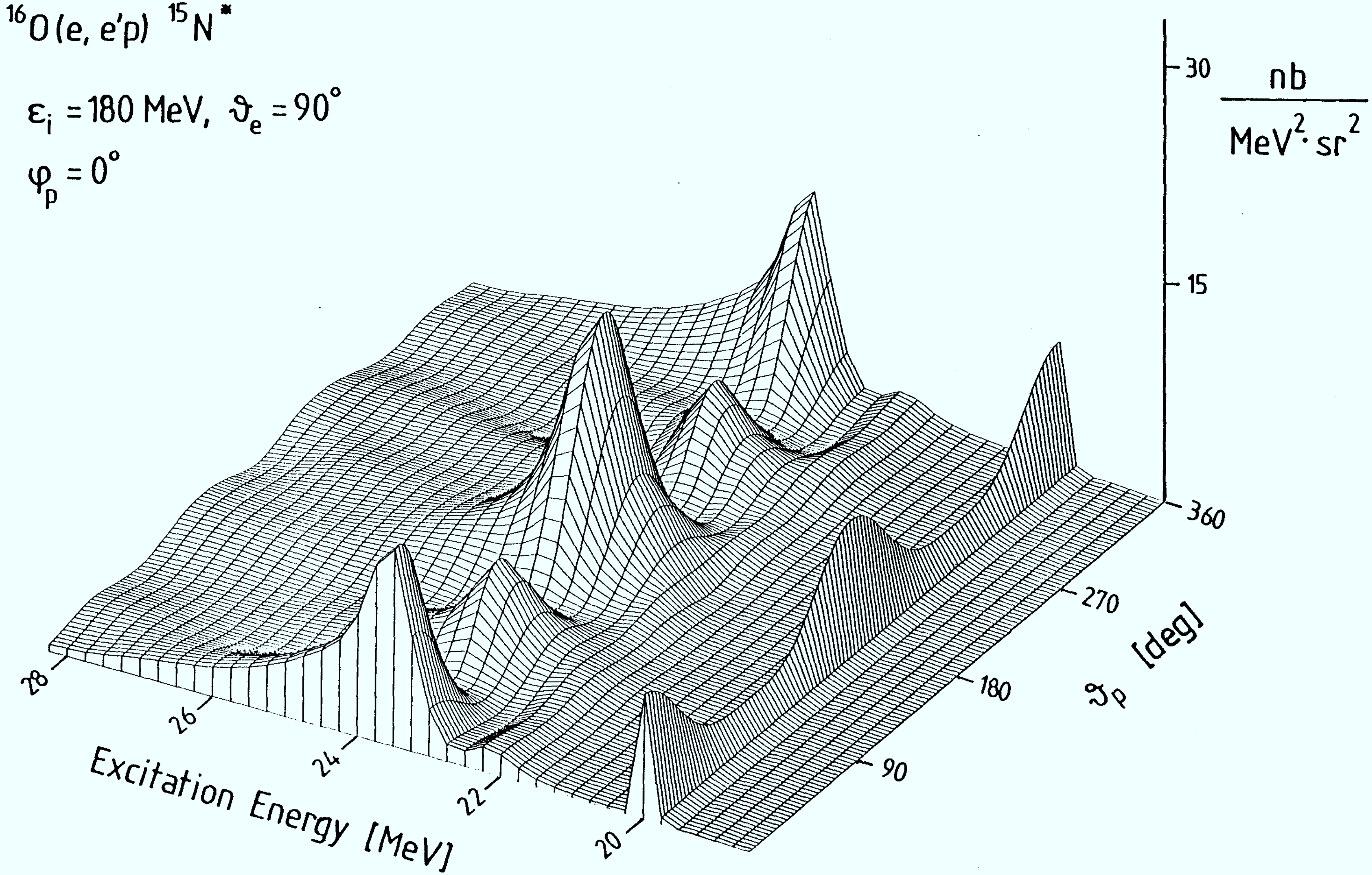

$^{16}O(e, e'p)\ ^{15}N^*$
$\varepsilon_i = 180$ MeV, $\vartheta_e = 90°$
$\varphi_p = 0°$
30
15
360
$\frac{nb}{MeV^2 \cdot sr^2}$
270
180
90
ϑ_p [deg]
20
22
24
26
28
Excitation Energy [MeV]

Fig. 19

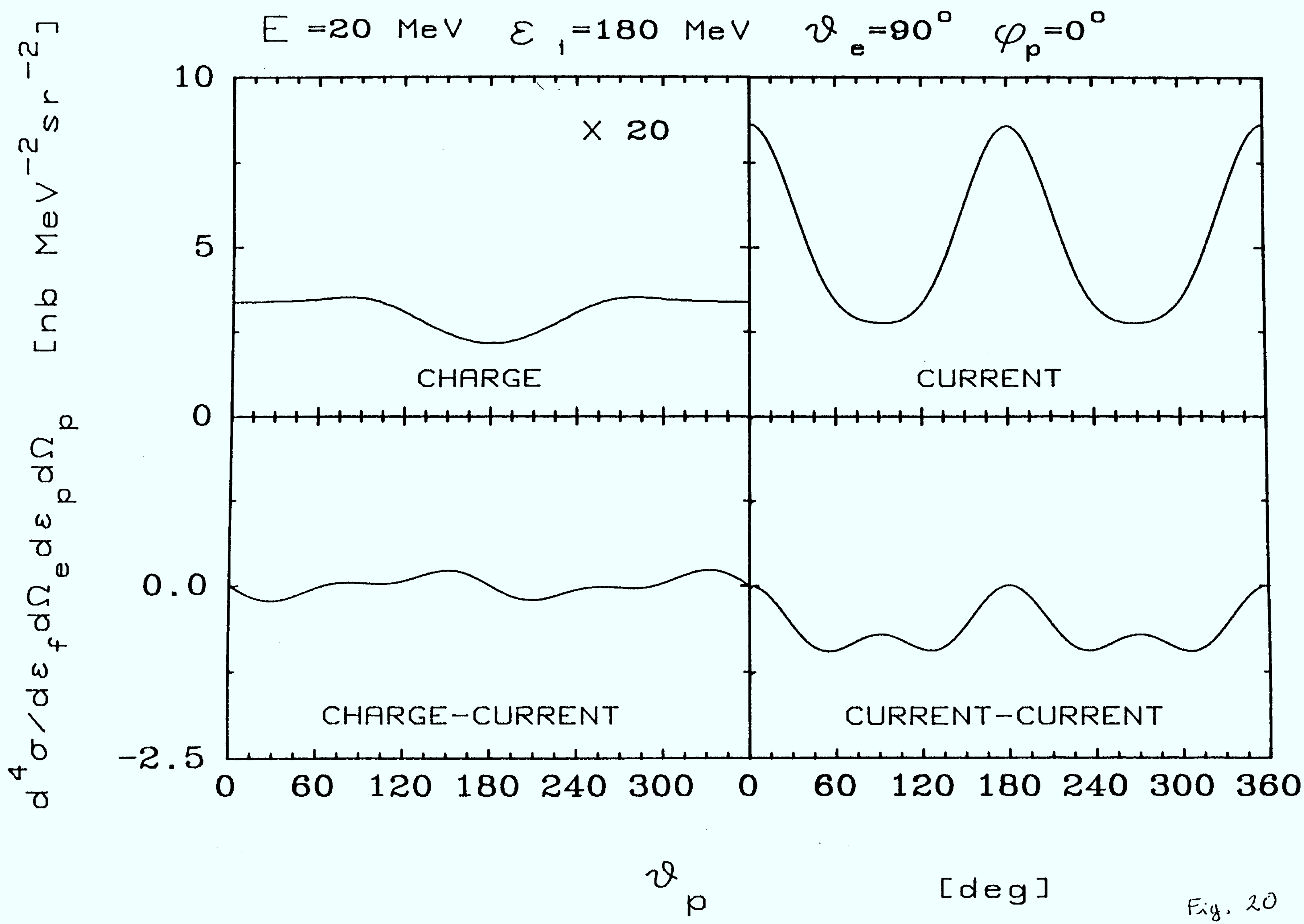
E =20 MeV ε i =180 MeV ϑ e =90° φ p =0°
× 20
CHARGE
CURRENT
CHARGE-CURRENT
CURRENT-CURRENT
10
5
0
0.0
-2.5
0 60 120 180 240 300 0 60 120 180 240 300 360
d4σ/dεf dΩe dεp dΩp [nb MeV-2 sr-2]
ϑ p [deg]

Fig. 20

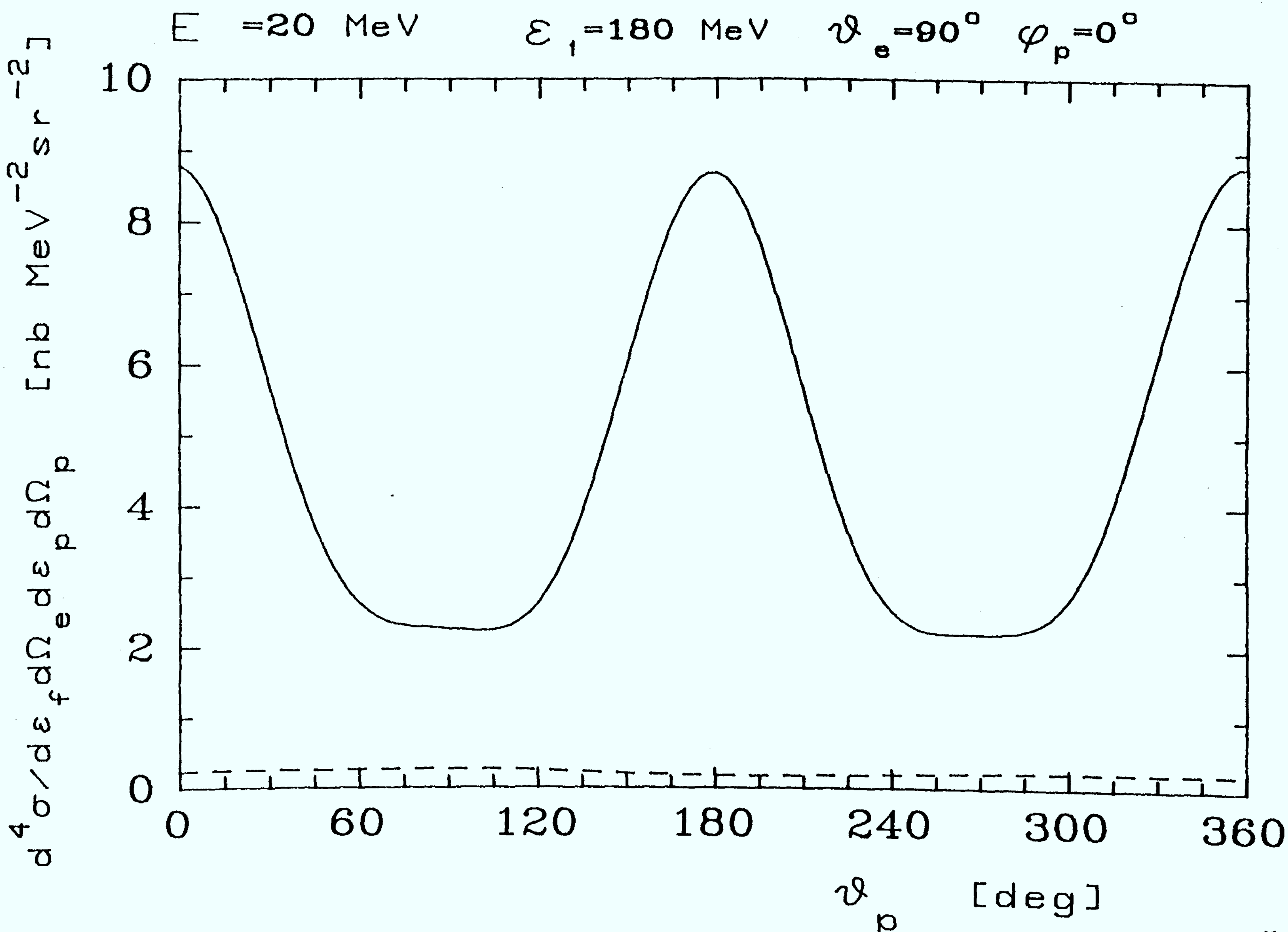
E =20 MeV
$\mathcal{E}_1$=180 MeV
ϑ_e=90°
φ_p=0°
10
8
6
4
2
0
60
120
180
240
300
360
$d^4\sigma/d\varepsilon_f d\Omega_e d\varepsilon_p d\Omega_p$ [nb MeV^{-2}sr^{-2}]
ϑ_p [deg]

Fig. 21

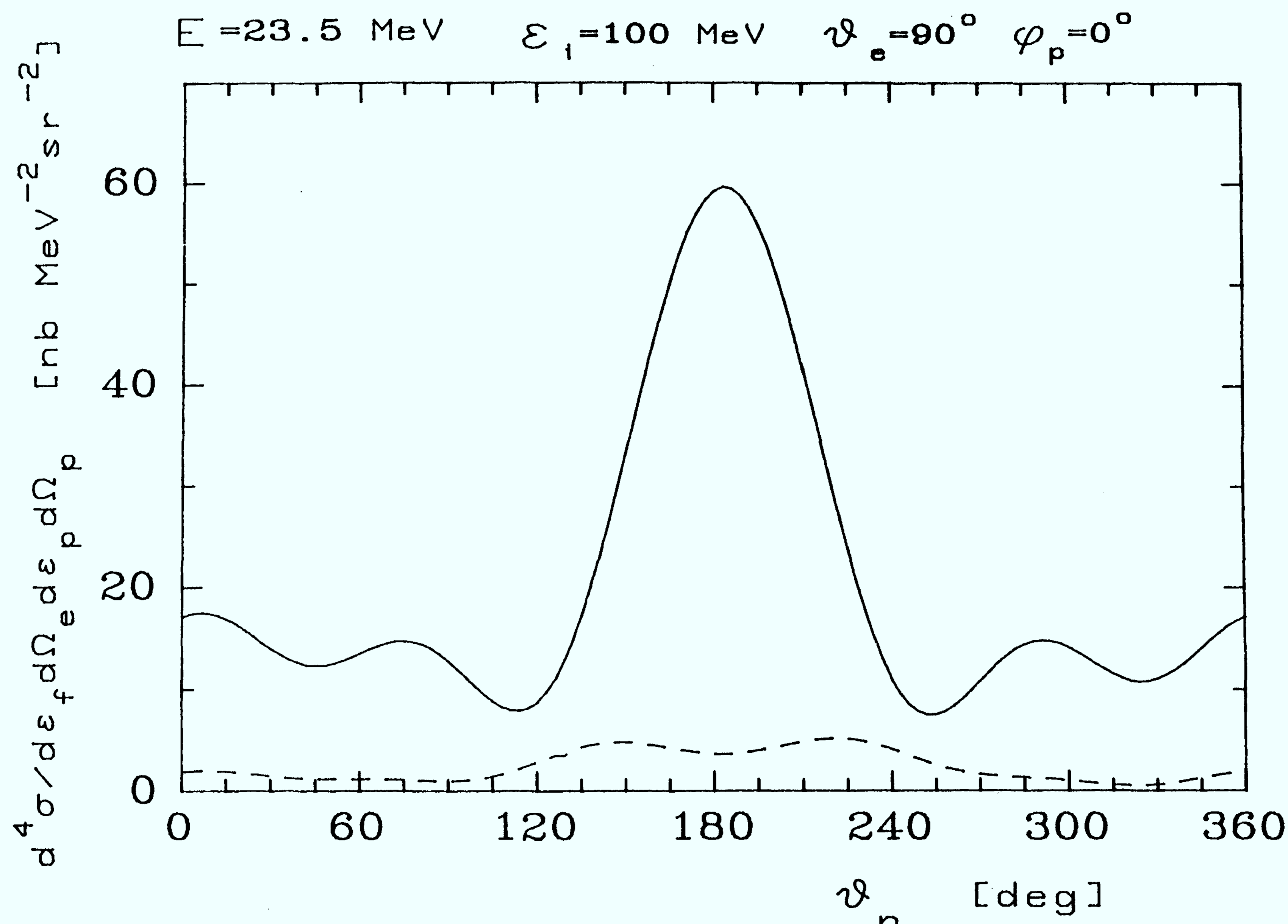

E =23.5 MeV
ε1=100 MeV
ϑe=90°
φp=0°
d4σ/dεfdΩedεpdΩp [nb MeV-2sr-2]
0
20
40
60
0
60
120
180
240
300
360
ϑp [deg]

Fig. 22

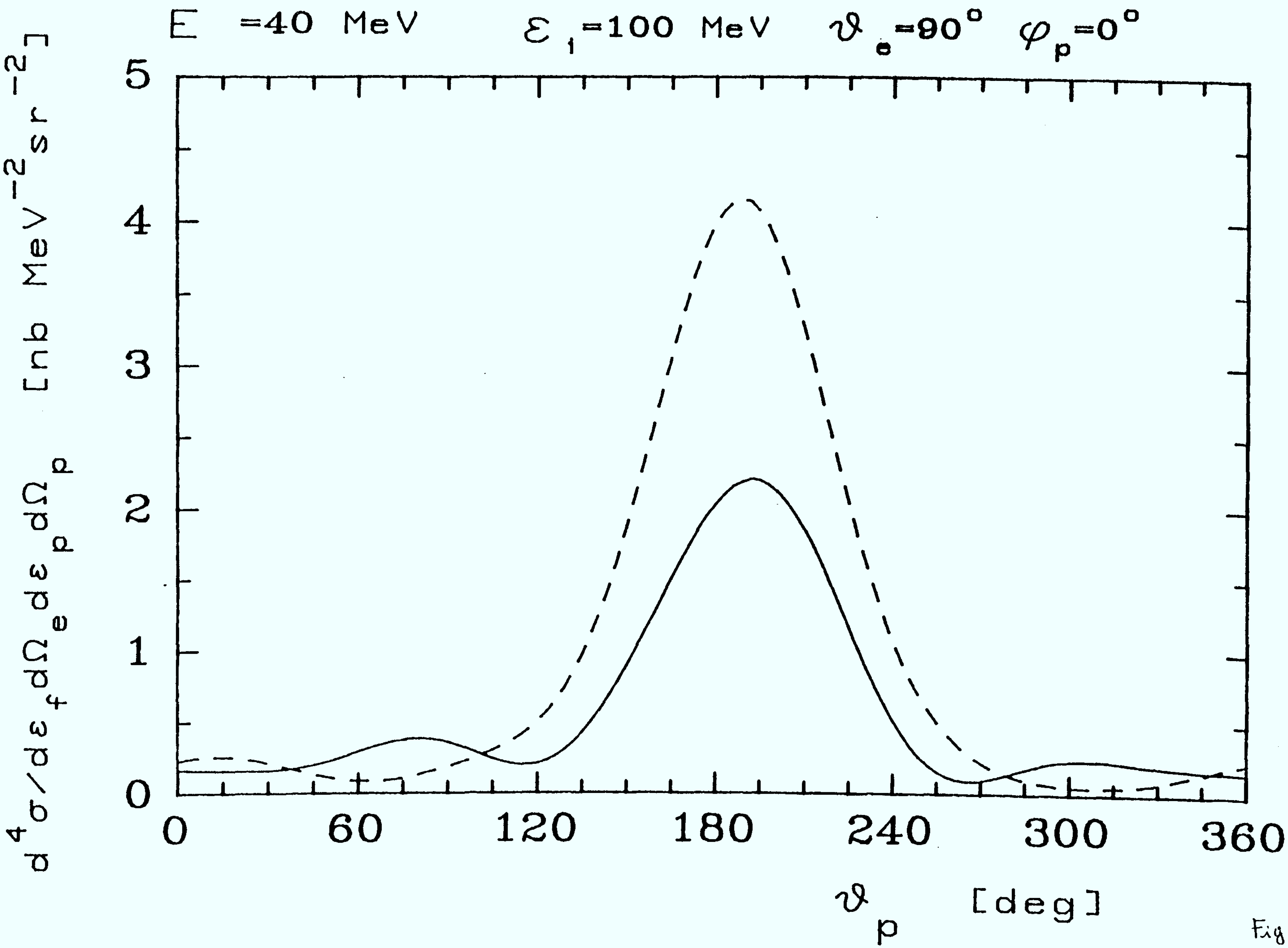
E =40 MeV
ε_i=100 MeV
ϑ_e=90°
φ_p=0°
d^4σ/dε_f dΩ_e dε_p dΩ_p [nb MeV^-2 sr^-2]
0
1
2
3
4
5
0
60
120
180
240
300
360
ϑ_p [deg]

Fig. 23

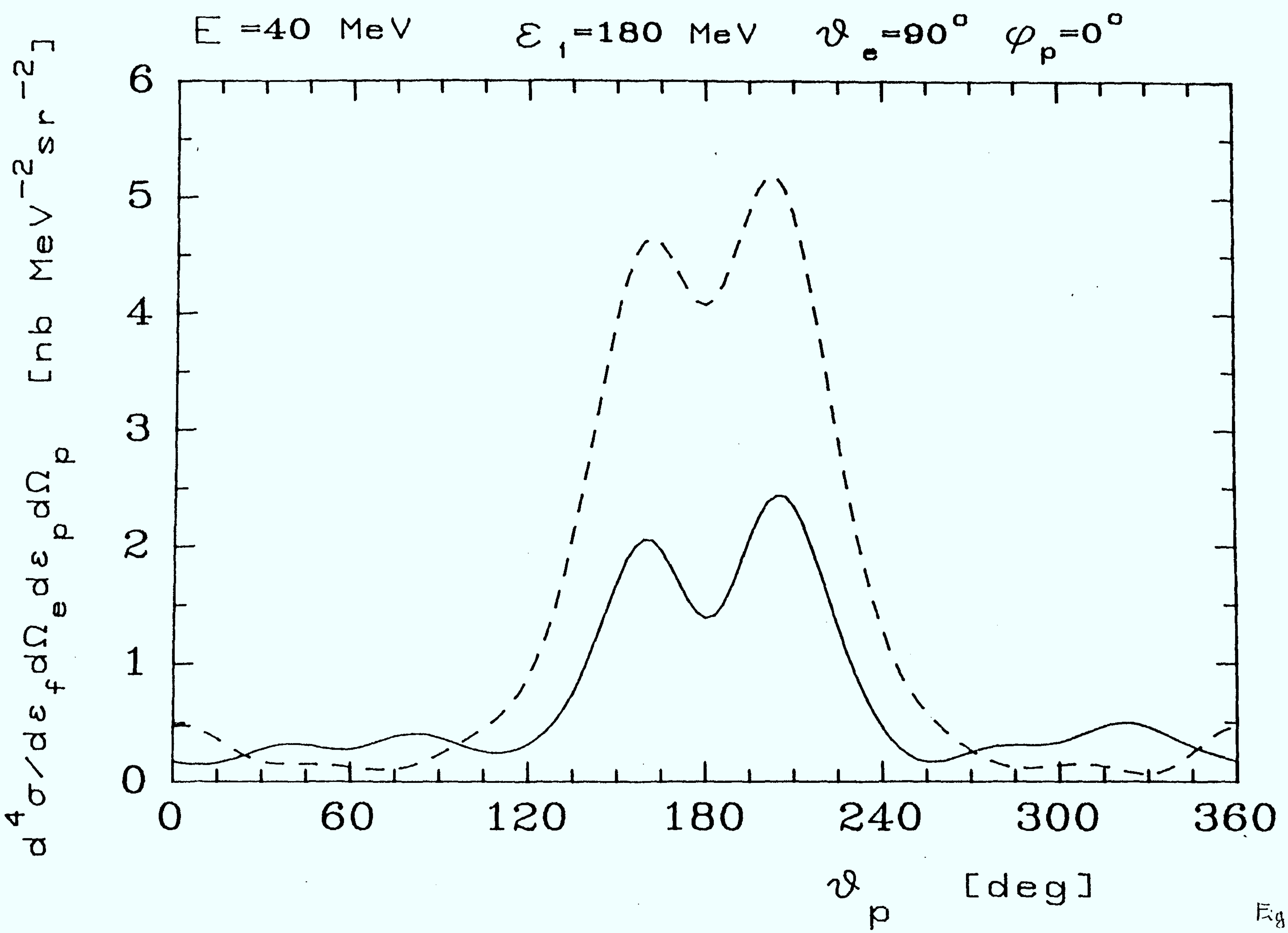

E =40 MeV
ε₁=180 MeV
ϑe=90°
φp=0°
d⁴σ/dεf dΩe dεp dΩp [nb MeV⁻² sr⁻²]
0
1
2
3
4
5
6
0
60
120
180
240
300
360
ϑp [deg]

Fig. 24

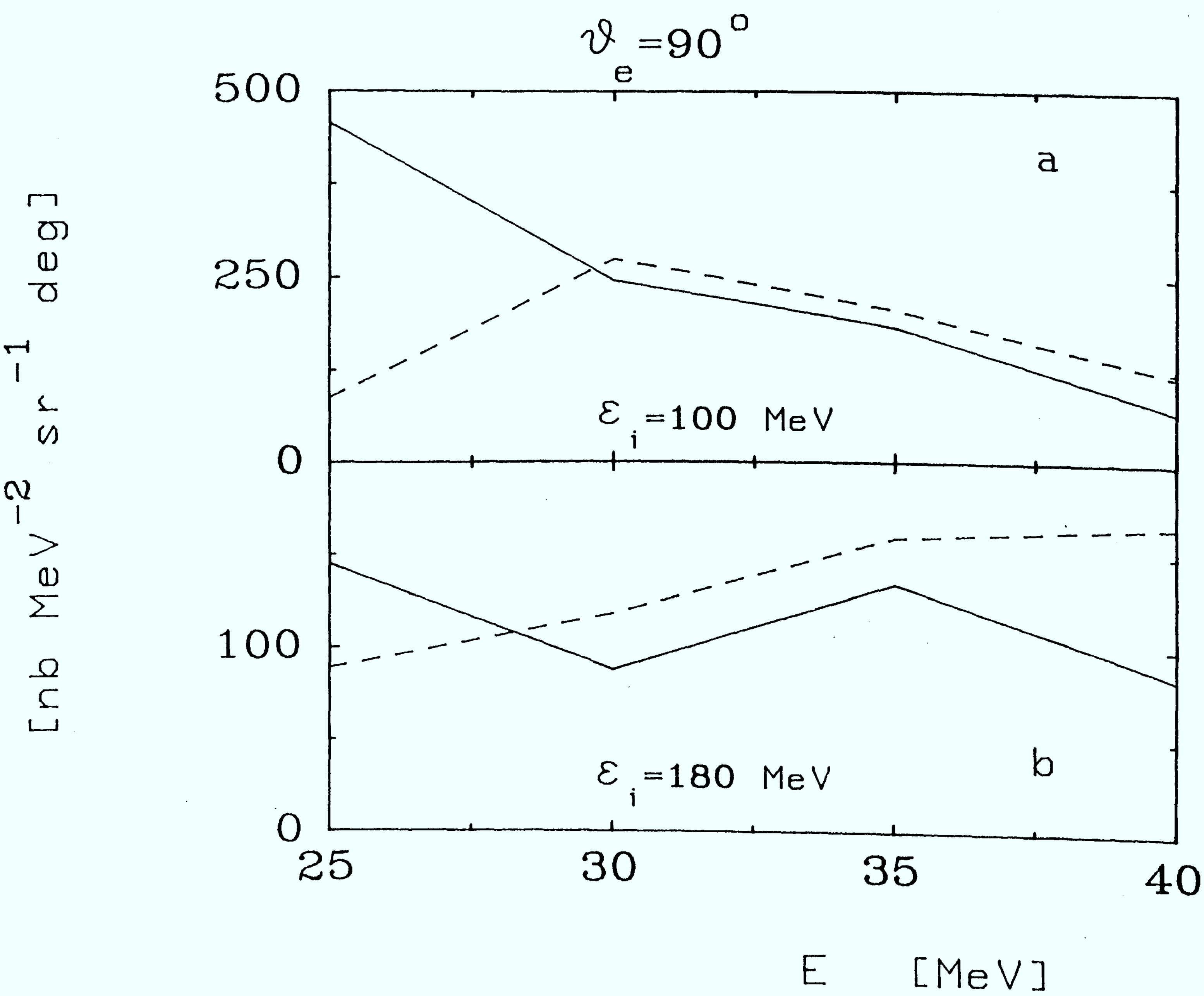

$\vartheta_e=90^o$
500
250
0
100
0
a
b
ε_i=100 MeV
ε_i=180 MeV
25
30
35
40
E [MeV]
[nb MeV^{-2} sr^{-1} deg]

Fig. 25

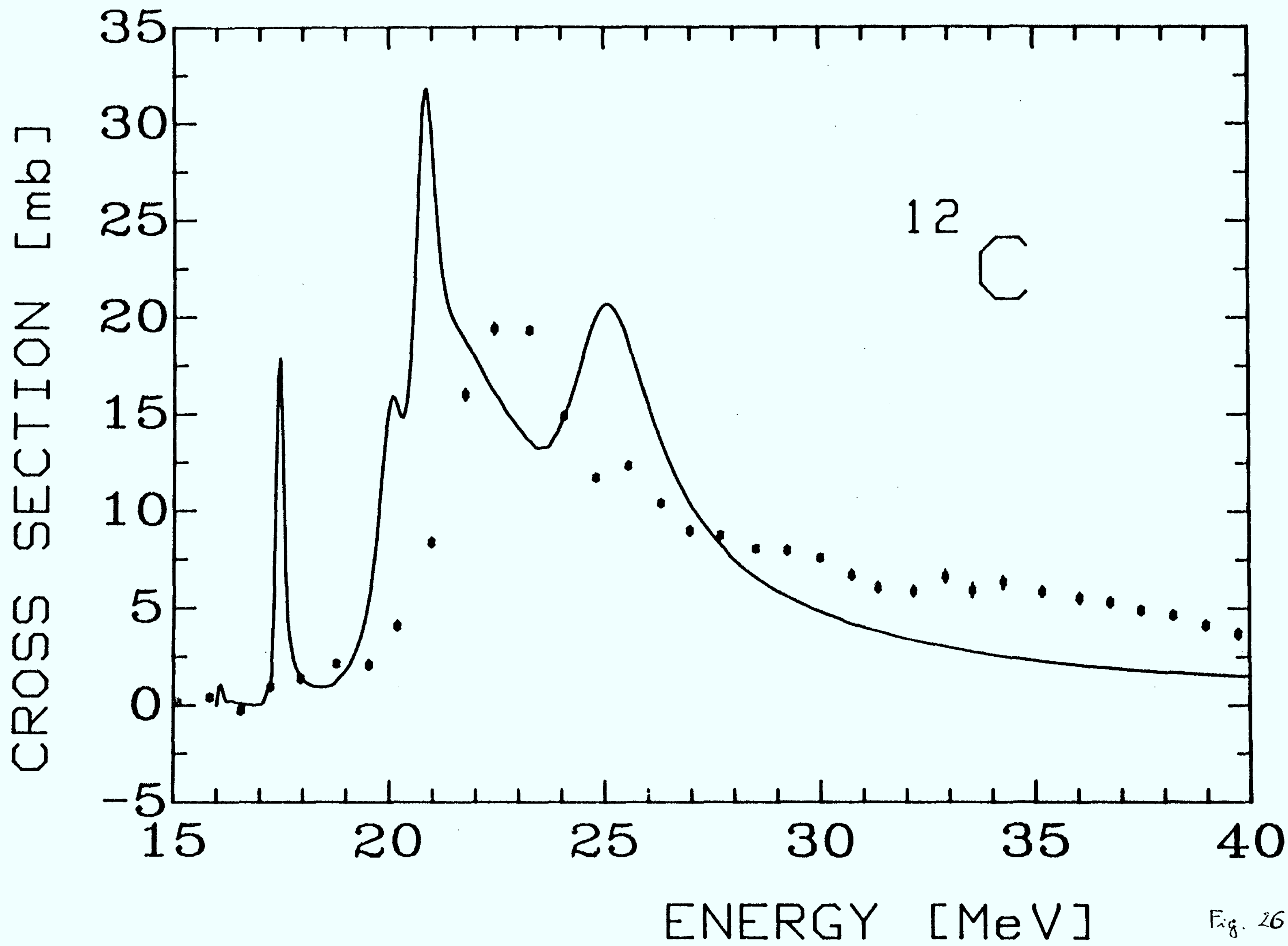

35
30
25
20
15
10
5
0
-5
CROSS SECTION [mb]
15
20
25
30
35
40
ENERGY [MeV]
^{12}C

Fig. 26

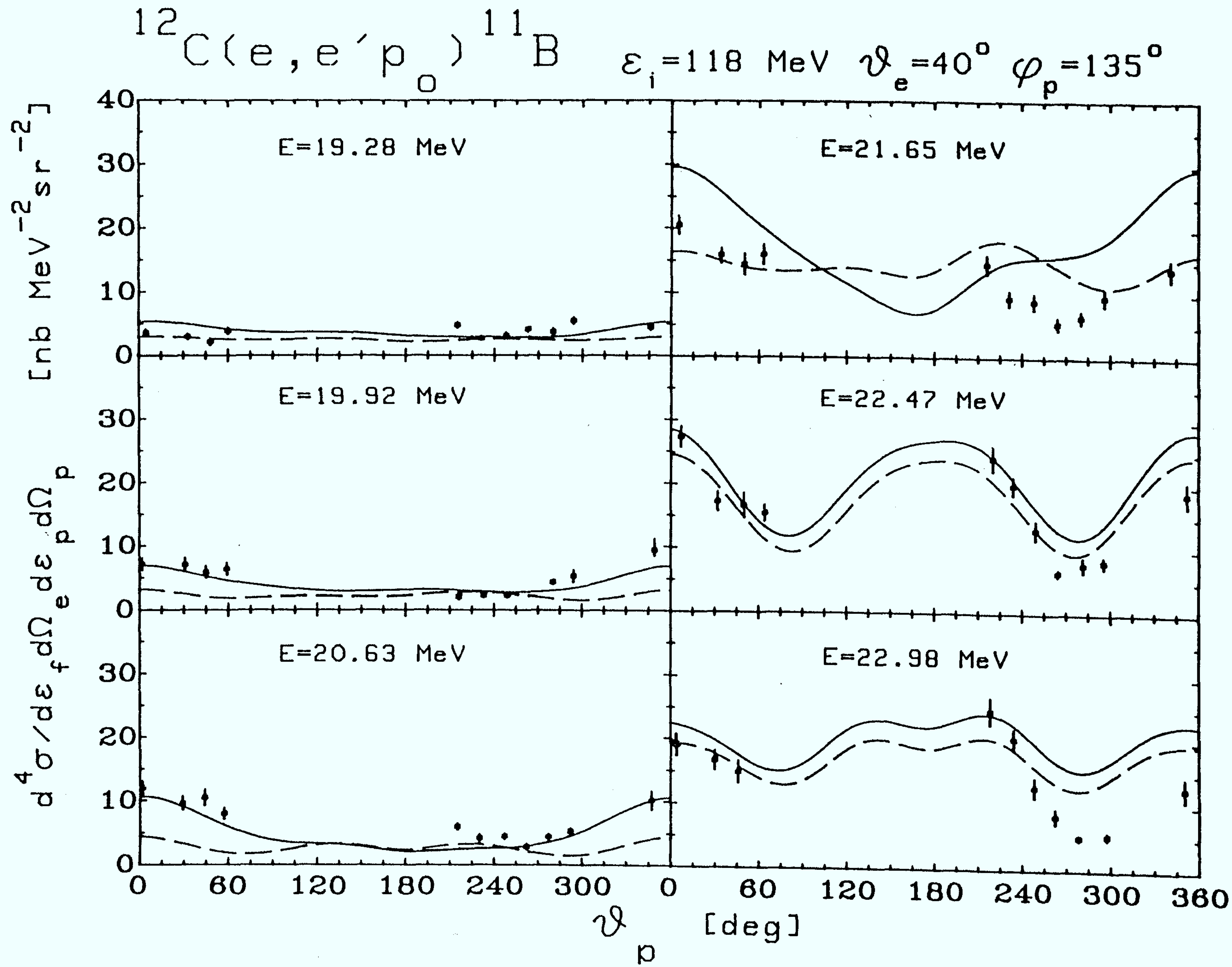

12C(e,e'p0)11B
εi=118 MeV ϑe=40° φp=135°
E=19.28 MeV
E=19.92 MeV
E=20.63 MeV
E=21.65 MeV
E=22.47 MeV
E=22.98 MeV
d4σ/dεf dΩe dεp dΩp [nb MeV-2 sr-2]
ϑp [deg]
0
10
20
30
40
60
120
180
240
300
360

Fig. 27

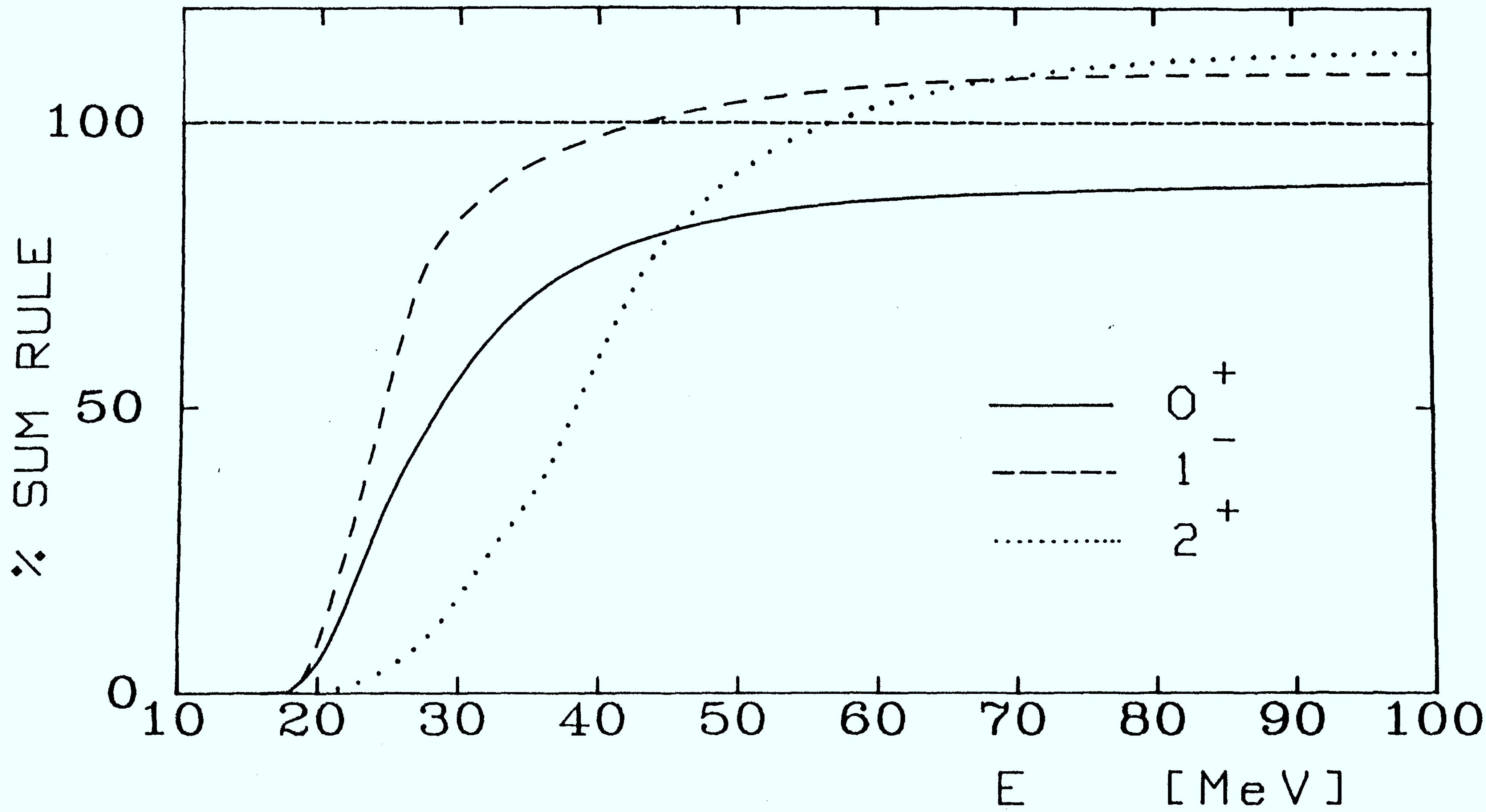

Fig. 28